Control of Molecular Spontaneous Emission in an Optical λ/2-Microresonator

Contents

1 Introduction

1.1 Aim of this thesis

The interaction between single quantum mechanical emitters (QME), i. e. atoms, ions or molecules, and the electromagnetic field is of fundamental interest in quantum- and nano-optics. Deep insight into the interaction mechanisms was gained in the field of cavity-QED by investigating single atoms strongly coupled to single cavity modes of optical resonators, see e. g. [1] and references herein. In the simplest case, such a resonator consists of two plane parallel mirrors offering high reflectivity, i. e. the well-known Fabry-Perot-resonator [2]. If the mirror spacing of a planar resonator is reduced to one half emission wavelength of embedded QME, it is called $\lambda/2$-microresonator.

It turned out that $\lambda/2$-microresonators are of particular interest for studying the radiative properties of embedded QME: The presence of resonator mirrors or, in other words, boundary conditions for the electromagnetic field drastically alter the photonic mode structure surrounding QME with respect to free space. As a result, even weak coupling of QME to the photonic mode structure or, in other words, to on- and off-axis cavity resonances of a $\lambda/2$-microresonator results in a significant temporal, spectral and angular redistribution of the radiation emitted by embedded QME, e. g. [3–5].

In the field of single molecule spectroscopy, single fluorescent dopant molecules immobilized in condensed or solid host matrices were investigated by means of laser spectroscopy and recognized as proper candidates for quantum optical experiments, e. g. [6–8]. Single molecule fluorescence microscopy and spectroscopy, see for example [9,10], are tightly connected with confocal microscopy [11]: This method incorporates focussing optics with high numerical apertures and delivers extremely small observation volumes which are needed to achieve a sufficient signal to noise ratio for single molecule detection. Hence, by eliminating the ensemble-averaging with the help of single molecule microscopy and spectroscopy, the coupling mechanism between single molecular dipole emitters and a single photonic mode of a microresonator could be studied experimentally for the first time under well-defined conditions.

The experimental basis of this work was the development of a microresonator that allows for studying the radiative properties of embedded and spatially immobilized fluorescent molecules for varying emitter concentrations by means of scanning confocal optical microscopy and spectroscopy. Ultimately, the microresonator should allow observation of spatially isolated

1

and immobilized single molecules for different mirror spacings within the same microresonator sample at both ambient and cryogenic temperatures.

The scientific goal was to study the modification of the Spontaneous Emission rate of molecules embedded in a planar optical $\lambda/2$-microresonator down to the single molecule level. The experimental results were aimed to be compared with calculations based on the various theoretical approaches already presented in the literature, e.g. [3, 12].

Finally, the findings were aimed to impact at least two technological fields of increasing interest:

1. Design of **advanced light emitting devices**. Utilizing planar microresonators turned out to be of greatest importance for the improvement of advanced light emitting structures like, e. g. all-polymer optoelectronic devices [13], random microcavity lasers [14] and single photon sources [15].

2. Design of **advanced light sensing devices**. $\lambda/2$-microresonators can improve the performance of advanced applications for ultra sensitive analytics like, for example, integrated lab-on-microchips.

1.2   Scope of this thesis

In this thesis, we investigate the influence of a planar optical $\lambda/2$-microresonator on the Spontaneous Emission rate of embedded molecules and the implications on the microresonator-controlled emission by means of scanning confocal optical microscopy and spectroscopy. The chapters of this work can be studied almost independently based on chapter 2 providing the fundamental knowledge for the research described in this work. The order of the chapters, however, refers all optical phenomena investigated here to the microresonator-controlled Spontaneous emission rate of single molecules discussed in chapter 3. Each chapter starts with an introduction of the main objective and refers to the specific instrumentation briefly presented in chapter 1.3. Theoretical discussion is provided and referenced as far as it is needed for understanding and modeling the experimental results.

In chapter 2, we introduce a new microresonator design and discuss the preparation and characterization of the resonator mirrors. The manufacturing of the microresonator doped with molecules as well as the experimental determination of the relevant system parameters are described. Using scanning confocal microscopy and spectroscopy, we demonstrate single molecule sensitivity and basic performance of the microresonator-molecule system.

In chapter 3, we discuss microresonator-controlled fluorescence decay of single dye molecules interacting with photonic modes of the microresonator in the $\lambda/2$-regime. From measured single molecule fluorescence decay curves, we derive the microresonator-controlled Spontaneous Emission rates and compare the results with predictions from rate calculations based on first order perturbation theory.

In chapter 4, we investigate the spectral shape of microresonator-controlled fluorescence emission of molecular ensembles as well as single molecules for varying mirror spacings. The spectral shape of the outcoupled emission is modeled by accounting the complex interplay between focussed pump field, free-space fluorescence properties of embedded molecules, optical properties of the microresonator and detection conditions. The results are compared with the measured and calculated on-axis transmission spectra of the microresonator for the corresponding mirror spacings.

In chapter 5, we investigate the fluorescence dynamics of dye molecules immobilized in the $\lambda/2$-microresonator for varying emitter concentrations. The influence of the microresonator-controlled Spontaneous Emission rate of embedded molecules on both output and Stimulated Emission efficiency is clarified.

In chapter 6, we investigate spatial modes formed by the $\lambda/2$-microresona-

tor using widefield imaging microscopy. The spatial mode diameter as derived from the experimental results is compared with theoretical predictions based on the optical properties of the microresonator.

In chapter 7, we study the coupling of molecular vibrations to photonic modes of the $\lambda/2$-microresonator in fluorescence and Raman scattering experiments. Experimental results are supported by rate calculations revealing selective enhancement and suppression of distinct radiative electronic-vibronic transitions. Moreover, we demonstrate that the microresonator acts as an ultra sensitive micro-spectrometer.

In chapter 8, we investigate the fluorescence emission of single molecules embedded in the $\lambda/2$-microresonator at cryogenic temperatures by means of Fourier spectroscopy. In particular, we study the influence of typical single molecule features like intensity blinking and spectral diffusion on the visibility of two-beam interference fringes.

1.3 Instrumentation

Optical measurements at room temperature were performed with an home-built inverted confocal microscope (based on an Axiovert 135 TV, Zeiss) which has already been described in detail [16]. As sketched in Fig. 1, a parallel laser beam provided by a single line argon-ion-laser (60X-200, American Laser Corporation) operating at $\lambda_{exc} = 488$ nm was divided by a beam splitter and focussed on the microresonator sample with an immersion objective offering a high numerical aperture (Planeoflex 100x / NA=1.3, Zeiss). Raster scanning the microresonator in x and y direction with respect to the diffraction-limited spot of the fixed microscope objective was done using a feedback-controlled sample stage (P-517.K008, Physik Instrumente). The collected fluorescence signal was separated from the reflected laser light by a holographic notch filter ($\lambda_{center} = 488$ nm, Kaiser). Successively, the light transmitted through the notch filter was spatially filtered using a pinhole and focused on the detector. For confocal imaging as well as for acquisition of fluorescence time traces, a single photon counting avalanche photo diode (SPCM-AQR-14, Perkin Elmer) was used. Fluorescence spectra were acquired with a grating spectrograph (SpectraPro 300i, Acton Research) in combination with a liquid nitrogen cooled CCD camera (LNCCD-1340/100-EB/1, Princeton Instruments).

For **time-resolved spectroscopy**, i. e. measurement of fluorescence decay curves as discussed in chapters 3 and 5, the experimental setup was equipped with a time correlated single photon counting board (timeharp 100, Picoquant) together with a start/stop diode (DET 210, Thorlabs) and a single photon counting avalanche photo diode (SPCM-AQR-14, Perkin Elmer). Pulsed excitation light was delivered by an ultrafast laser system (Verdi V10, REGA 9000, OPA, Coherent) operating at $\lambda_{exc} = 488$ nm providing a repetition rate of 250 kHz.

For **widefield imaging** of emission pattern as shown in chapter 6, we mounted a peltier cooled CCD camera (Newton DU971-UVB, Andor) with a pixel size of 16 μm by 16 μm to the upper tube side port of the Axiovert microscope body providing a 100 fold magnification of the object plane. In this case, no pinhole in the detection path was used and the diameter of the field of view was limited by the back aperture of the microscope objective.

For **confocal microscopy and spectroscopy on single-walled carbon nanotubes** embedded in the microresonator as reported in chapter 7, a He-Ne-laser (1137P, Uniphase) was used as excitation light source and the
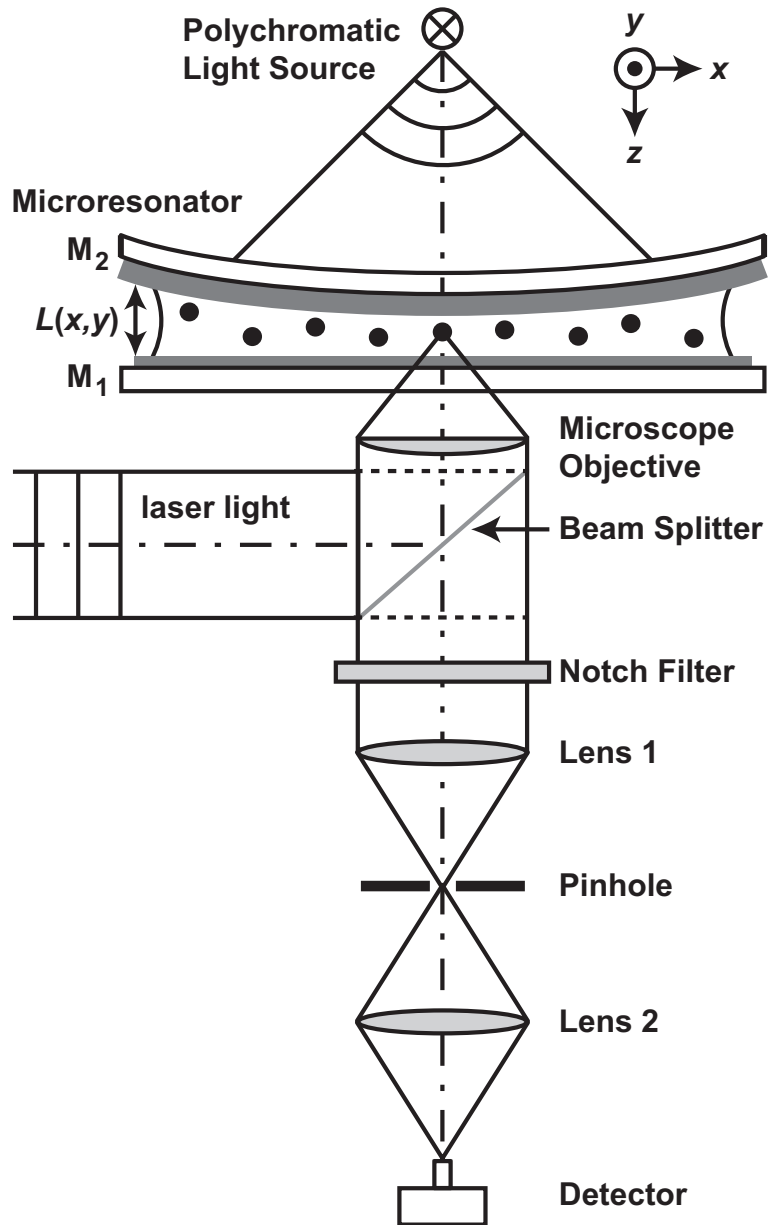
Figure 1: Schematic diagram of the experimental setup for optical experiments on the microresonator sample as discussed in the text. The microresonator is formed by two silver mirrors $M_{1,2}$ enclosing a thin polymer film doped with quantum mechanical emitters (dots).

laser light was separated from both Raman-scattered and photoluminescence light using a holographic notch filter (λ_{center} = 633 nm, Kaiser).

Determination of the local mirror spacing $L(x, y)$ of the microresonator was done illuminating the microresonator from the top using a polychromatic light source (KL 1500 LCD, Leica) and collecting the transmitted light by point wise detection as indicated in Fig. 1 and discussed in detail in chapter 2.

Optical measurements at low temperature were performed using a home-built confocal microscope head as shown in Fig. 2. During experiments, the microscope head was inserted in a liquid-helium bath cryostat (SVT-200 Model 10 CNDT, Janis) and optically connected to the external experimental setup by glass windows at the sides of the cryostat. The setup in combination with a parabolic mirror as a focussing element has already been described carefully [17].

In contrast to the cited work, we equipped the microscope head with a microscope objective which was mounted on a piezo-driven position unit as shown schematically in Fig. 2(a). This enabled coarse adjustment of the microscope objective in x and y direction with respect to the piezo scanning tube as indicated by grey arrows. The piezo scanning tube allowed for scanning the microresonator sample with respect to the microscope objective within a maximum scanning range of roughly 30 μm by 30 μm, depending on the temperature. It was mounted on a piezo-driven position unit for adjusting the microresonator in z direction with respect to the microscope objective, i. e. focussing. An optical multimode fiber was guided through the sample holder and provided polychromatic and laser light, respectively, allowing both sample alignment and transmission measurements as discussed in chapter 2.

For **confocal fluorescence microscopy**, a parallel laser beam was divided with a dichroic beam splitter (z572rdc, Chroma), directed through the cryostat windows and reflected by a plane mirror into the back aperture of the microscope objective (see Fig. 2). Here, a tunable single mode ring dye laser (CR-699, Coherent) with R6G-solution as active medium pumped by a cw-operating frequency-doubled Neodym-YAG laser (Verdi V10, Coherent) served as excitation laser. The molecular fluorescence emission was collected with the same microscope objective and separated from the excitation light using a holographic notch filter (λ_{center} = 568 nm, Kaiser). For confocal imaging, an avalanche photon counting module (SPCM-AQ 141, EG + G) was used as detector. Fluorescence spectra were acquired with a grating spec-
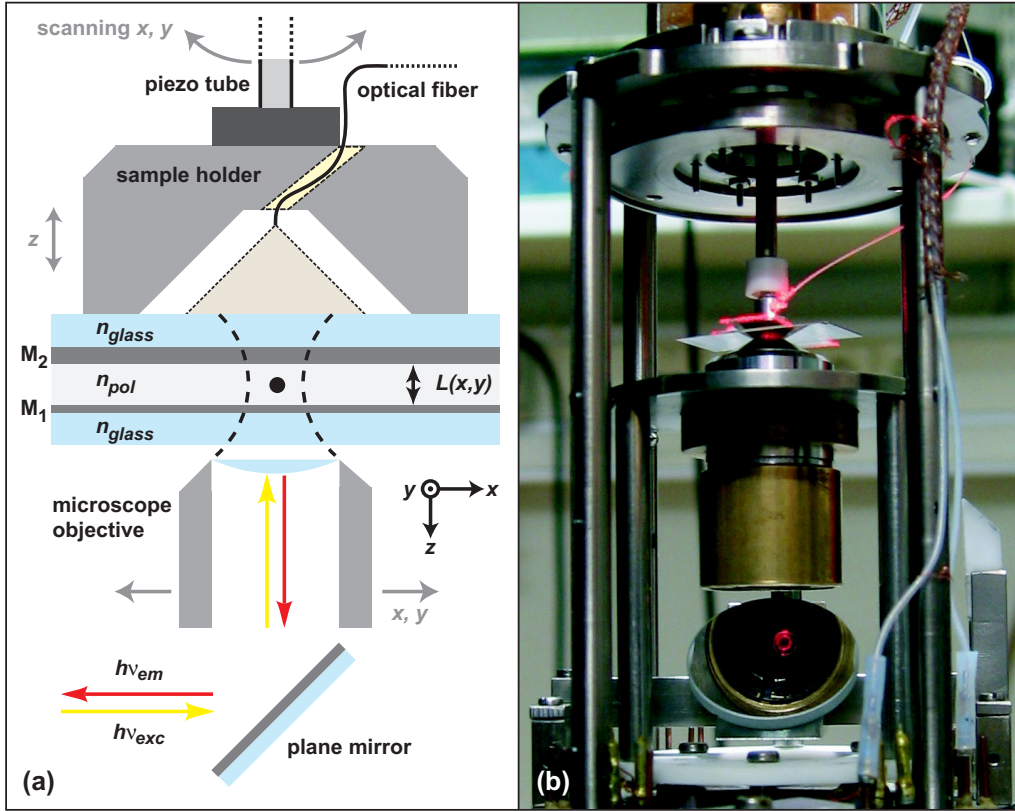
Figure 2: (a) Schematic diagram and (b) photograph of the microscope head with a microresonator sample mounted for low temperature experiments as described in the text. During measurement, the microscope head is located in a liquid helium bath cryostat. In (a), the focal regime of the microscope objective is indicated by dashed lines.

trograph (SpectraPro 300i, Acton Research) equipped with a liquid nitrogen cooled CCD camera (LNCCD-1340/100-EB/1, Princeton Instruments). The performance of the setup as described here was verified first during photoluminescence studies on individual single-walled carbon nanotubes [18–21].

Measurements of **intensity correlations** as discussed in chapter 7 were performed using a Hanbury-Brown and Twiss interferometer [22] as shown schematically in Fig. 3(a) consisting of a silver-coated non-polarizing beam splitter cube BS and two avalanche photodiodes (SPCM-AQR-14, Perkin Elmer) $D_{1,2}$ as detectors. The temporal correlation of measured photon counts was done using a time correlated single photon counting board (time-harp 100, Picoquant).
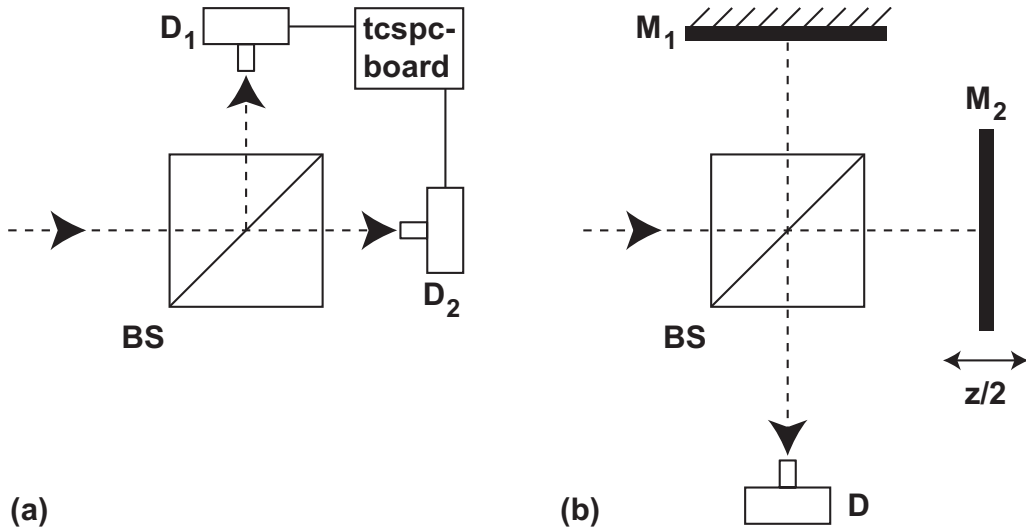
Figure 3: (a) Schematic diagram of a Hanbury-Brown and Twiss interferometer consisting of a beam splitter cube BS, two detectors $D_{1,2}$ and a time correlated single photon counting board (tcspc-board) for the measurement of intensity correlations. (b) Schematic diagram of a Michelson interferometer consisting of a beam splitter cube BS, two mirrors $M_{1,2}$ and a detector D for the measurement of field correlations, i. e. interferograms.

For acquisition of **interferograms** as presented in chapter 8, we guided the collimated fluorescence light to a Michelson interferometer [2] as sketched in Fig. 3(b) consisting of a silver-coated non-polarizing beam splitter cube and two plane silver mirrors $M_{1,2}$. One of the interferometer mirrors (M_2) was mounted on a feedback-controlled sample stage (P-517.3CL, Physik Instrumente) which allowed controlled displacement of the moving mirror within a range of 100 μm with a resolution of one nm. The light transmitted through the interferometer was focussed on a detector D, an avalanche photodiode (SPCM-200 CD1718, EG + G) in our case.

2 A New Microresonator Design for Single Molecule Detection

In this chapter, we present a new microresonator design which allows the efficient detection of single molecules by measuring the molecular fluorescence emission coupled into resonant photonic modes. In a first step, we discuss the preparation and characterization of the resonator mirrors. In a second step, the manufacturing of the microresonator and the experimental determination of its optical properties is described. In a third step, using scanning confocal microscopy and spectroscopy, the radiative coupling between single dye molecules and the longitudinal cavity mode of the resonator in the $\lambda/2$-regime is investigated. As a result, we observe a significant spectral narrowing of single molecule fluorescence emission determined by the spectral width of the on-axis transmission spectrum of the microresonator.

2.1 Introduction

Optical microresonators, i. e. resonators with confinement dimensions in the range of one emission wavelength of embedded quantum mechanical emitters (QME), can be used to control the spatial, spectral, and temporal properties of the emitted radiation [3]. This control is essential for improving existing single photon sources based on single molecules [23–29] and for applications in quantum computation [30] and quantum cryptography [31]. Moreover, utilization of microresonators can enhance the performance of devices for ultra sensitive analytics, e. g. [32, 33].

Ultimately, it would be desirable to couple the fluorescence emission of a single molecule to a single resonator mode which overlaps with the emission spectrum of the molecule. Hence, the enclosed molecule is forced to emit photons with a narrowed energy distribution that is determined by the photonic mode of the $\lambda/2$-microresonator. Up to now, evidence for the observation of single molecules embedded in optical microcavities has only been derived from the measured sub-poissonian photon statistics of the fluorescence emission from highly diluted dye solutions enclosed within planar microresonators [34, 35] and single molecule fluorescence bursts from streams of dye-doped microdroplets [36]. However, to study the interaction between single fluorescent emitters and a microresonator with well-defined coupling conditions, it is necessary to immobilize and spatially isolate them. In this case, the transition dipole is fixed with respect to the resonator mirrors and collective fluorescence dynamics mediated by the microresonator is prevented [37].

In this chapter, we show how to build and characterize such a microresonator and demonstrate that it is possible to spatially address single molecules in the microresonator using confocal microscopy. Moreover, we show that the spectral width of microresonator-controlled single molecule fluorescence spectra is determined by the spectral width of the measured on-axis transmission spectrum of the microresonator which offers $FWHM$-values around 35 nm and 15 nm, respectively, in our case.

2.2 Preparation and Characterization of the Resonator Mirrors

The silver mirrors of the microresonator were evaporated with a rate around 1 nm per second onto commercially available and cleaned microscope glass coverslips (thickness: 170 µm) by an electron beam source (EB3, Edwards) under high vacuum conditions ($p \simeq 10^{-6}$ mbar). The thickness of the silver mirrors was chosen to be $d_2 = 60$ (30) nm for the back mirror M_2 and $d_1 =$
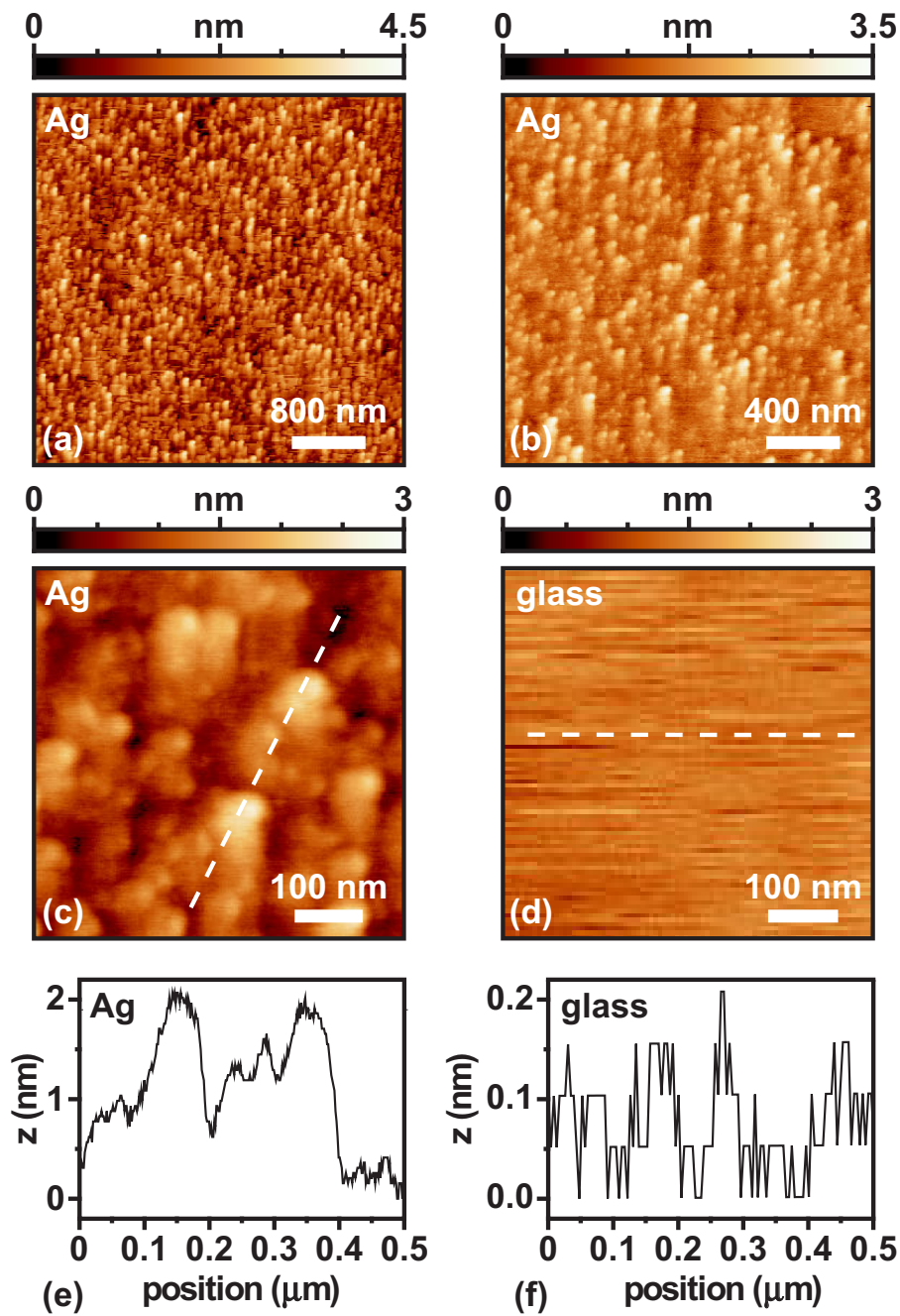
Figure 4: Atomic force microscopy images measured on the surface of (a)-(c) a silver mirror with thickness $d = 30$ nm and (d) a cleaned glass microscope cover slip which serves as mirror substrate. The dashed lines in (c) and (d) indicate the courses of the cross sections shown in (e) for the silver mirror and (f) for the bare glass substrate.
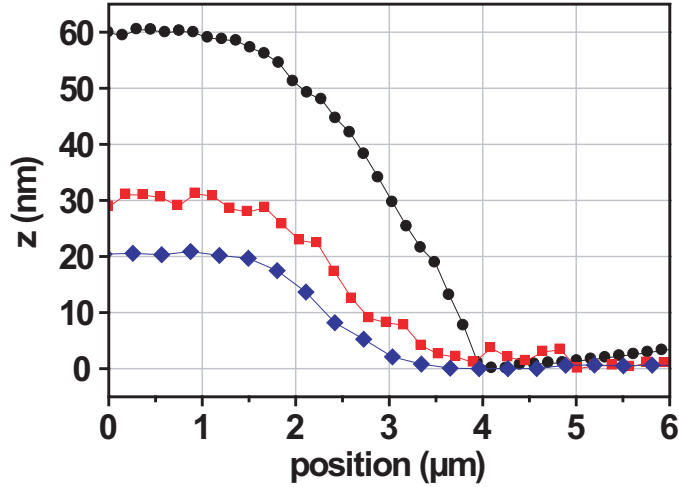
Figure 5: Cross sections taken from atomic force microscopy images measured on the edge between silver-coated and bare areas of the glass substrate. The thickness d of the silver films as monitored by an oscillating quartz unit during evaporation was 60 nm (dots), 30 nm (squares) and 20 nm (diamonds), respectively.

30 (20) nm for the input/output mirror M_1 to optimize the performance, i. e. excitation and fluorescence light for single molecule detection pass the same mirror M_1 (see Fig. 1). The thickness of the silver films was monitored during the evaporation process using an oscillating quartz unit (FTM7, Edwards). After evaporation, both surface quality and thickness of the mirrors was verified by atomic force microscope (AFM) measurements. In Fig. 4(a)-(c), the topography of a silver mirror with $d = 30$ nm is shown. The silver film has a surface roughness below 2 nm as can be seen from the cross section shown in Fig. 4(e) which was taken along the dashed line in Fig. 4(c). As a reference, the topography of the bare mirror substrate, i. e. the microscope coverslip, is shown in Fig. 4(d). The corresponding cross section along the dashed line is shown in Fig. 4(f) and demonstrates that the glass surface is flat within the z-resolution (± 0.2 nm) of the AFM-setup. As a result, we conclude that on a length scale of microns the surface quality of the silver mirrors is better than $\lambda/100$ for the entire optical regime.

To verify the thickness of the silver films as monitored by the oscillating quartz unit, we evaporated silver steps with heights of 20 nm, 30 nm and 60 nm, respectively, onto clean glass-coverslips. In a second step, we measured the step heights with an AFM and the resulting cross sections are shown in Fig. 5. A good agreement between the d-values determined by the oscillating

quartz unit and the results from the topography measurements was found. The maximum thickness mismatch observed in our experiments was $\Delta d \pm 5$ nm mainly caused by the imprecise manual shutter control of the evaporation setup.

2.3 Preparation and Characterization of the Microresonator

Microresonator Design

The microresonator consists of two silver mirrors separated by a thin polymer film doped with QME in ultra low concentration as sketched in Fig. 6(a). As a broadband-emitting QME, we used the perylen-derivative N-(2,6-diisopropylphenyl)-perylen-3,4-dicarboxymid abbreviated PI in the following. The structural formula of PI-molecules is shown in Fig. 7. The dye molecules were embedded into an UV-polymerizing optical adhesive (NOA61, Norland) with refractive index $n_{pol} = 1.56$ acting as a dielectric medium between the microresonator mirrors. For the preparation, both PI-molecules and the monomers of the adhesive were dissolved in dichloroethane. Evaporation of the solvent resulted in an active medium composed of randomly oriented and homogenously distributed dye molecules in well-controlled concentrations. Both ensemble absorbance and fluorescence spectra of PI-molecules embedded in the cured polymer are shown in Fig. 7. Single molecule experiments were carried out at concentrations around $c_{PI} = 10^{-10}$ mol/l.

To get access to various mirror spacings L, one of the resonator mirrors is slightly inclined with respect to the other by applying a punctual force $\vec{F}$ before the curing process is initialized (see Fig. 6(a)). This leads to a well-defined dependence of the mirror spacing L on the position within the $(x$-$y)$-plane of the microresonator. To achieve nanometer-accuracy for the L-alignment, the force is applied using a spring mechanism controlled by a micrometer screw as sketched in Fig. 6(a). A photograph of the microresonator press is shown in Fig. 6(b). The adjustment of the mirror spacing is controlled by illuminating mirror M_1 with a polychromatic light source and observing the white light interference pattern, i. e. Newton rings of equal optical thickness [2], in reflection (see left part of Fig. 6(c)). Note, that the visibility of the interference fringes in reflection decreases with increasing d_1, hence limiting the adjustment procedure described here. However, we could adjust microresonators having a d_1 of up to 40 nm. In a last step, UV-illumination of the sample leads to the polymerization of the optical adhesive
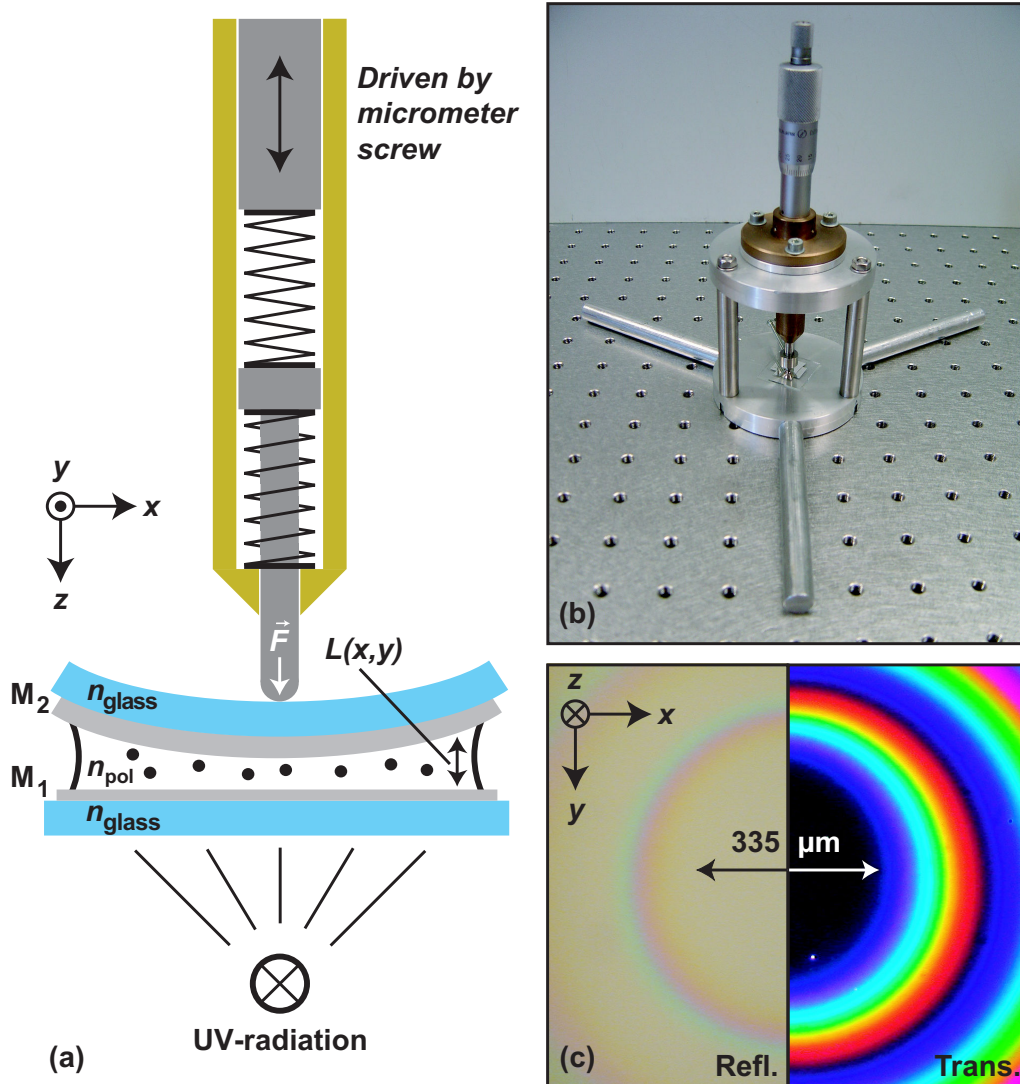
Figure 6: (a) Schematic diagram of the microresonator press and the manufacturing process as described in the text. (b) Photograph of the microresonator press. (c) Widefield microscopy images (200 fold magnification) of the central area of a microresonator having mirror thickness of $d_1 = 30$ nm and $d_2 = 60$ nm illuminated with white light showing the same area recorded in reflection (left) and transmission (right) on M_1, respectively.

15
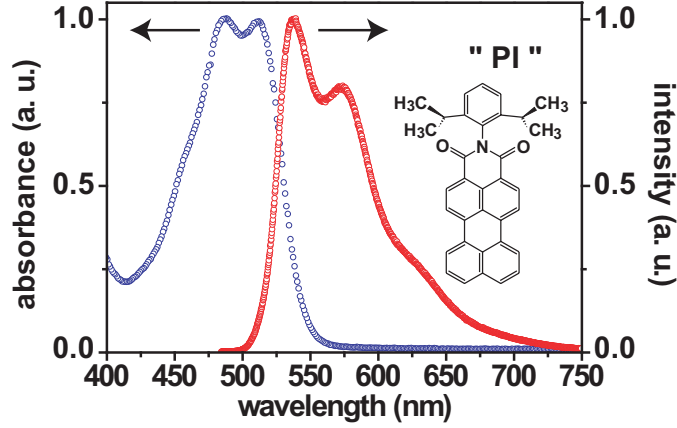
Figure 7: Absorbance (blue circles) and fluorescence (red circles) spectrum, respectively, of ensembles of PI-molecules homogeneously distributed and randomly oriented in a cured polymer film (NOA 61) enclosed between two glass coverslips. The structural formula of PI is also shown.

effectively gluing together the two silver mirrors. It should be remarked that the microresonator design presented in this chapter has some relation to a similar resonator layout reported earlier using an air gap between two dielectric substrates with different refractive indices [38].

Optical Characterization of the Microresonator

Both optical quality and uniformity of the microresonator were controlled by observing the white light interference pattern in transmission as shown in the right part of Fig. 6(c). Within the central area of the microresonator having a diameter $d_{center} \simeq 335$ µm, the mirror spacing $L(x,y)$ is so small that all optical fields impinging on the structure are reflected effectively. The transmission of the microresonator obeys the resonance condition

$$L(x,y) = \left(\mathrm{m} - (2\pi)^{-1} \sum_i \Delta\phi_i \left(d_i, \vartheta, \lambda \right) \right) \lambda \left(x, y \right) / 2 n_{pol} \cos \vartheta \qquad (1)$$

Here, m = 1, 2, 3, ... denotes the interference order, $\Delta\phi_i$ the phase change due to reflection at the respective mirror i = 1, 2 and ϑ the incidence angle of a parallel light beam having a wavelength $\lambda(x,y)$. Note, that the mirror spacing L deviates from the effective resonator length in the case of real metal mirrors. The phase changes $\Delta\phi_i$ introduce a nearly constant offset which reduces the mirror spacing L by around 50 nm as compared to the results for ideal metal mirrors ($\Delta\phi_i = \pi$). The $\Delta\phi_i$ were taken as a result from our

16
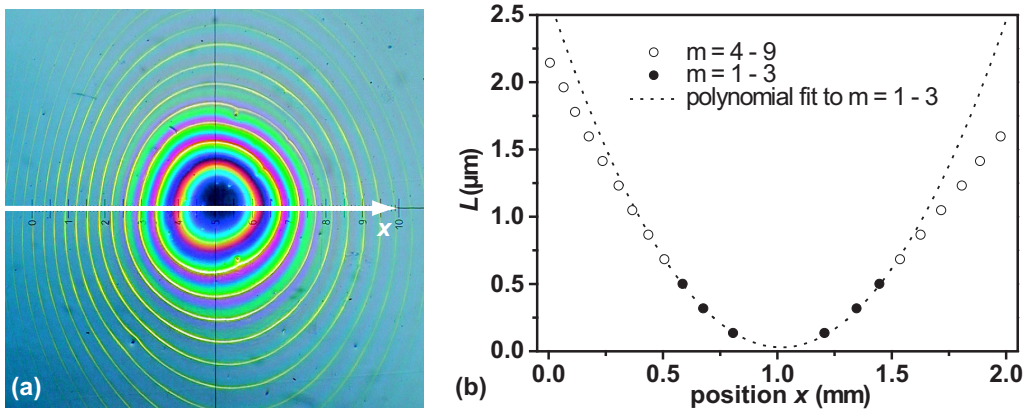
Figure 8: (a) Transmission widefield microscopy image (50 fold magnifica-tion) of the central part of a microresonator having mirror thickness of d_1 = 20 nm and d_2 = 30 nm. Concentric laser (λ = 570 nm) and white light interference fringes are visible surrounding the dark center. (b) Profile of the mirror spacing $L(x)$ calculated by Eqn. 1 using the positions of the sharp laser fringes in the optical image (a). For the interference orders m = 1 - 3 (dots), $L(x)$ is well-described by a second order polynomial (dotted line).

computer simulations which were verified by reproducing comparable results for silver mirrors and microresonators reported elsewhere [39].

For preparing microresonators, we used silver mirrors having thickness d_i of 20 nm, 30 nm and 60 nm, respectively. Assuming λ = 532 nm, $\vartheta = 0^o$ and a parallel polarization of the optical field with respect to the plane of the metal mirror M_i, we obtained the following mirror reflectivities R_i and phase changes $\Delta\phi_i$ from our calculations:

d_i (nm)	20	30	60
R_i	0.50	0.71	0.91
$\Delta\phi_i$	1.08	0.98	0.91

Choosing $y = 0$ for convenience, we could determine the exact relation between L and x by simultaneously illuminating the microresonator with parallel laser light and the positions x corresponding to distinct interference orders were measured using a division scale (see Fig. 8(a)). The local mirror spacing $L(x)$ and hence the mirror spacing profile depicted in Fig. 8(b) was obtained from the optical image in Fig. 8(a) with the following parameters: λ_{laser} = 570 nm, n_{pol} = 1.56; $\vartheta = 0^o$, $\sum \Delta\phi_i = 1.85$ and m increasing from 1 for the innermost ring up to m = 12. For small values of m, $L(x)$ is

17

well-described by a second order polynomial (doted line in Fig. 8(b)) as it is expected for Newton rings.

2.4   Single Molecule Detection in the $\lambda/2$-Regime

Local Mirror Spacing and Cavity-Q

For single molecule detection within the first resonator mode (i. e. the $\lambda/2$-regime), we addressed an area of 100 μm x 100 μm in the innermost interference fringe (m = 1) as shown in Fig. 9(a). The microresonator was illuminated with polychromatic plane waves as sketched in Fig. 1 to determine the two relevant system parameters: The local mirror spacing L and the local Q-factor of the microresonator. A typical local on-axis transmission spectrum of a microresonator having $d_1 = 30$ nm and $d_2 = 60$ nm is presented Fig. 8(c). $L(x)$ can be obtained from the wavelength at the transmission maximum $\lambda(x)$ using Eqn. 1 with the parameters $n_{pol} = 1.56$; $\vartheta = 0^o$, m = 1 and the corresponding $\Delta\phi_i$. This procedure was found to give reproducible results with an accuracy of $\delta L = \pm$ 3 nm.

A systematic non-linear increase of the mirror spacing with increasing distance from the microresonator center is observed as shown in Fig. 9(b) and can be understood as a magnified section of the L-profile as depicted in Fig. 8(b) around m = 1. From the data shown in Fig. 9(b), $\Delta L/\Delta x \simeq 10^{-3}$ is obtained which means that a displacement Δx of 500 nm results in a variation of the mirror spacing ΔL of about 0.5 nm. This is up to one order of magnitude smaller than the surface roughness of the silver mirrors as determined by AFM-measurements (see Fig. 4(e)). This demonstrates that the microresonator acts as planar resonator in a very good approximation within the 500 nm focal spot diameter of our microscope objective. The measured transmission spectrum shown in Fig. 9(c) can be modeled using a Lorentzian line shape function and reveals the bare resonator linewidth having the $FWHM$-value $\Delta\omega$ at the center frequency ω_0 from which the cavity-Q is determined according to $Q = \omega_0/\Delta\omega$. For mirror spacings between 120 nm and 160 nm, which are typical for our measurements, the cavity-Q was found to increase with increasing L and had typical values of around 50. As a result, we can assign the cavity parameters L and Q for every sample position (x,y).

Single Molecule Fluorescence Detection

Using scanning confocal fluorescence microscopy (see chapter 1.3 and Fig. 1), we were able to detect spatially isolated bright spots that originate from single molecules on resonance with the structure (see Fig. 10). The
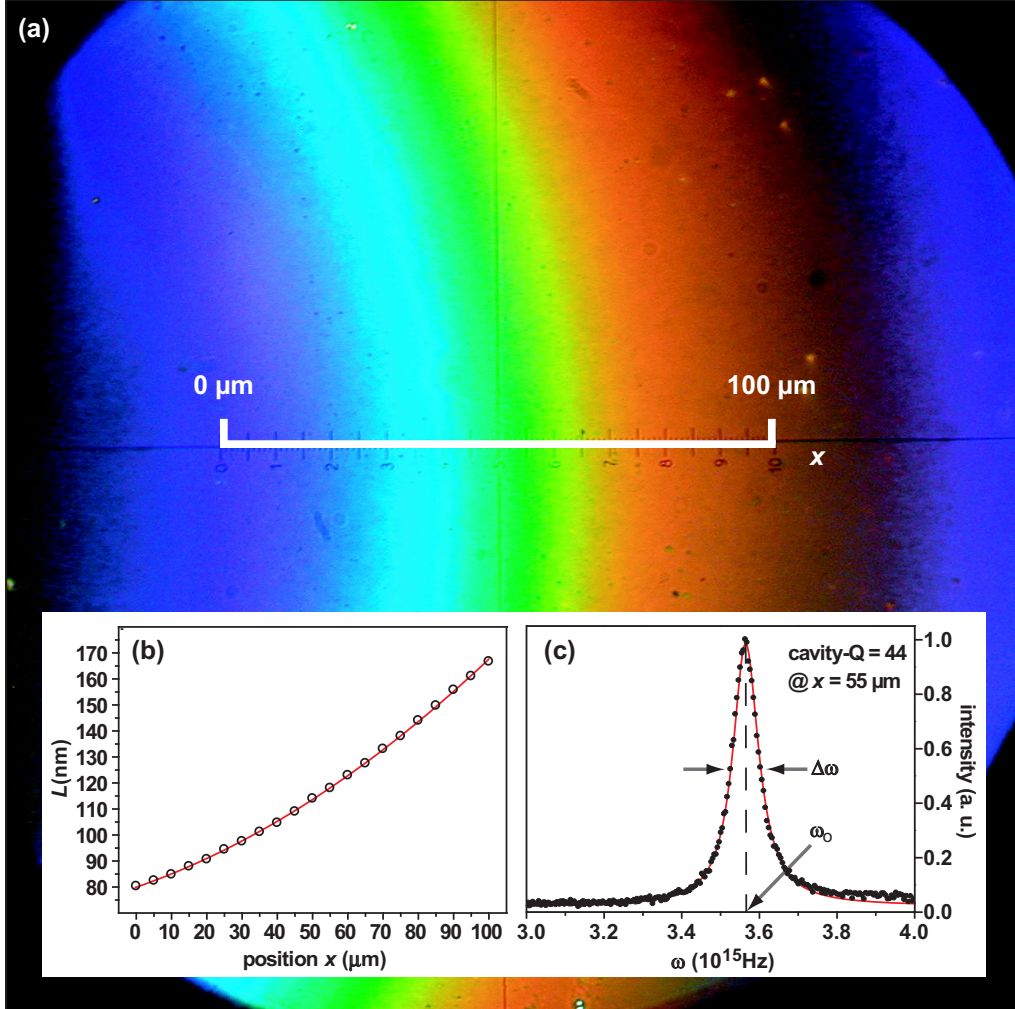
Figure 9: (a) Transmission widefield microscopy image (1000 fold magnification) showing the $\lambda/2$-regime of a microresonator having mirror thickness of $d_1 = 30$ nm and $d_2 = 60$ nm. (b) Variation of the local mirror spacing $L(x)$ determined from a series of local transmission spectra (see (c)) measured by moving the microresonator stepwise in x-direction along the white line shown in (a) with respect to a fixed microscope objective. The peak transmission wavelength $\lambda(x)$ is used to calculate $L(x)$ (circles) according to Eqn. 1. The solid line is a second order polynomial fit. (c) Measured local transmission spectrum of the microresonator (dots) fitted by a Lorentzian line shape function (line) giving a cavity quality-factor $Q = \omega_0/\Delta\omega = 44$.

19
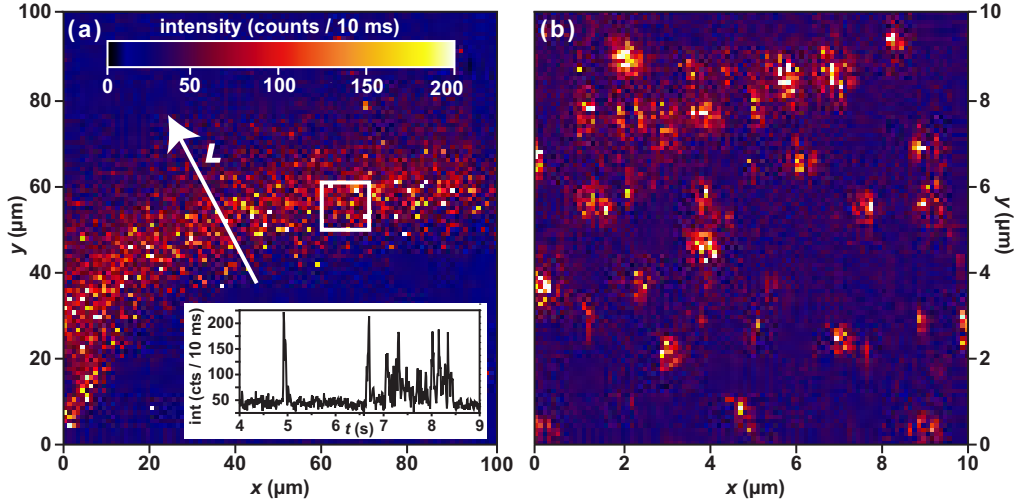
Figure 10: (a) Scanning confocal fluorescence microscopy image of the first order interference region (m = 1) of a Fabry-Perot type microresonator having mirror thickness of $d_1 = 30$ nm, $d_2 = 60$ nm and a dye concentration $c_{PI} = 10^{-10}$ mol/l. Bright spots (see also (b)) result from the fluorescence of individual molecules as can be seen from their characteristic blinking behaviour in the time-trace of the fluorescence intensity with time-intervals of 10 ms (inset). (b) Magnified section from the confocal image (a) as indicated there by the white frame. The intensity scale bar shown in (a) is also valid for (b).

section of the fluorescent ring shown in Fig. 10(a) corresponds to a section of the innermost interference fringe as shown in Fig. 9(a). Time-traces of the emitted fluorescence intensity (see inset Fig. 10(a)) acquired on isolated bright spots (see Fig. 10(b)) reveal blinking in the millisecond regime and sudden bleaching which is typical for single quantum systems. In addition, we observed photon-antibunching in the fluorescence emission of single terrylene molecules embedded in our microresonator at cryogenic temperatures (see inset in Fig. 27(b)) clearly demonstrating that our resonator system has single molecule sensitivity and is well-suited to produce single photons.

Note, that for mirror spacings L matching the resonance condition of the fluorescence wavelength according to Eqn. 1, single dye molecules were observed through silver mirrors with a thickness d_1 of up to 30 nm. Off resonance, i. e. for other L, the fluorescence signal was suppressed effectively and single molecule detection was not feasible, as expected. It should be remarked that single molecule fluorescence was also observed for higher interference orders up to m = 3. Since the observation volume increases with

20
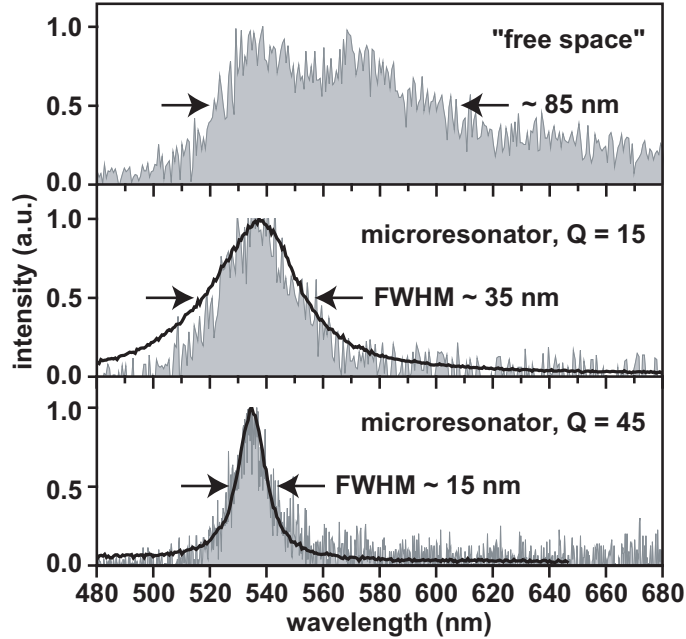
Figure 11: Single molecule fluorescence spectra (grey shaded areas) observed for dye molecules enclosed between the mirrors of a microresonator with Q-factors of 15 and 45, respectively, and in free space as reference. The full lines are the respective local on-axis transmission spectra for the corresponding positions on the microresonator measured using white light illumination.

the mirror spacing L, the ratio of single molecule to background fluorescence signal decreases for a given dye concentration and spatial addressing of single molecules becomes impossible.

2.5 Microresonator-Controlled Single Molecule Fluorescence Spectra

In Fig. 11 we present microresonator-controlled fluorescence spectra of single PI-molecules for mirror spacings L around 120 nm. Results obtained from two different microresonators offering cavity-Qs of 15 ($d_1 = 20$ nm, $d_2 = 30$ nm) and 45 ($d_1 = 30nm$, $d_2 = 60$ nm), respectively, were compared with the reference fluorescence spectrum of a single PI-molecule in free space. The free-space spectrum was acquired from a comparable sample as discussed above, just without silver mirrors. While the later spectrum exhibits a width of about 90 nm and an asymmetric band shape characteristic for the vibronic progression of organic dye molecules, the microresonator-controlled fluorescence spectrum for $Q = 15$ is cut off by the microresonator at the red side of

the spectrum while the blue side is determined by the fluorescence spectrum of the dye molecule itself. Finally, the single molecule fluorescence spectrum for $Q = 45$ features a narrow and symmetric band that is clearly determined by the local on-axis transmission spectrum of microresonator as shown in Fig. 11 as solid line. Obviously, the spectral width decreases with increasing cavity-Q, giving e. g. for $Q = 45$ a 6 fold decrease of the width of the emission profile compared to the molecule in free space, what effectively boosts the coherence length of the emitted radiation (see chapter 8) in view of the Wiener-Khinchin-theorem [40].

In chapter 4, we show that the spectral shape of microresonator-controlled fluorescence emission as shown in Fig. 11 can be modeled based on the microresonator-controlled Spontaneous Emission rate Γ_{SpE} for PI-molecules as a function of the mirror spacing L. The fundamental relation between Γ_{SpE} and L is the main objective of chapter 3.

2.6   Summary and Conclusion

In summary, we presented a new microresonator design which provides long term stability and single molecule sensitivity over months. In the following, it will be used for studying molecular fluorescence dynamics in microresonators under ambient conditions as well as at cryogenic temperatures. The microresonator-controlled single molecule fluorescence spectra measured at room temperature offer a narrowed and symmetric lineshape in comparison with the asymmetric band shape of the respective organic dye molecules in free space.

We consider the microresonator-controlled spectral narrowing of single molecule fluorescence emission or, from another point of view, the increased temporal coherence of the emitted single photon wave trains, as an important improvement for single photon sources based on dye molecules operating at room temperature.

Benefit could be gained from this work by integrating our microresonator design in a lab-on-microchip layout and combining it with microcapillaries or sheath flow cuvettes to improve the signal-to-noise ratio and spectral selectivity of ultra sensitive microfluidic analytical devices.

3 Microresonator-Controlled Spontaneous Emission Rates of Single Molecules

In this chapter, we discuss fluorescence decay curves delivered by single dye molecules embedded in a planar $\lambda/2$-microresonator. The Spontaneous Emission rate of individual molecules was found to be enhanced by the Purcell-effect up to 3 times compared to the Spontaneous Emission rate in free space as determined by the mirror spacing and in agreement with predictions from our calculations based on first order perturbation theory.

3.1 Introduction

According to Fermi's golden rule [41] the Spontaneous Emission (SpE) process of a photon by an atom or molecule depends on the transition dipole moment of the emitter and the electromagnetic vacuum field. Therefore, modifications of the electromagnetic field structure introduced by boundary conditions can lead to an enhancement [42, 43] or inhibition [44] of the emission rate Γ_{SpE} compared to the corresponding rate in free space. In the case of a planar microresonator, these variations are expected to be maximized if the mirror separation is reduced down to one half emission wavelength of enclosed emitters such that there is only one resonator mode which overlaps with the emission spectrum of the atom or molecule. Under this condition, as it was already shown in Fig. 11, the enclosed quantum object is forced to emit photons with a modified energy distribution that is determined by the photonic mode structure of the $\lambda/2$-microresonator.

Up to now, the enhancement or inhibition of Γ_{SpE} has been demonstrated with ensembles of fluorescent emitters between the flat mirrors of an optical microresonator [45–50], in laterally restricted microcavities [51, 52], microdroplets [53, 54] or dielectric micro- and nanospheres [55]. Experiments with only a few or a single emitter coupled to a cavity have been reported for atom beams passing a resonator [56–58] and, just recently, with a single Ca^+ ion trapped in the standing wave within an high finesse optical cavity [59]. An enhanced SpE rate for single semiconductor quantum dots embedded in high-Q disc- and post-type microcavities has been observed at cryogenic temperatures [60–62]. Although observation of single molecules in planar microresonators has been reported [34, 35], experimental investigations of how a $\lambda/2$-microresonator affects the decay dynamics of a single molecule are lacking.

In order to study the fluorescence decay rate Γ_{SpE} of single emitters in a microresonator experimentally, three requirements have to be fulfilled:

1. The emitters have to be separated over a distance larger than the transverse quantum correlation length [37, 63] or, in other words, the spatial mode radius [64, 65] of the system which is typically in the range of micrometers for a low-Q microresonator. Otherwise, the conventional (i. e. uncoupled) SpE-process for mirror spacings corresponding to the first order of interference (i. e. the $\lambda/2$-condition) is modified due to long-range coupling between the emitters. In consequence, the SpE

process merges into a Stimulated Emission process at exceedingly low excitation power [66].

2. Since the transition rate Γ_{SpE} depends on the orientation of the transition dipole with respect to the microresonator mirrors, it can only be determined from the fluorescence decay curves of a single transition dipole or from transition dipoles with identical orientations. Otherwise, multi-exponential decay profiles are expected for an ensemble of emitters with nonuniform orientations, precluding the quantification of Γ_{SpE}.

3. To achieve well-defined coupling conditions, the transition dipole needs to be fixed with respect to the resonator mirrors.

All three requirements can be matched by the study of single, spatially fixed and isolated molecules as quantum mechanical emitters embedded in the microresonator presented in chapter 2.

3.2   Experimental

The microresonator sample consisted of two resonator mirrors $M_{1,2}$ with a silver film thickness of 30 nm and 60 nm, respectively, resulting in a cavity-Q around 50 in the $\lambda/2$-regime (see chapter 2). A transparent polymer (n_{pol} = 1.56) doped with uniformly distributed and randomly oriented perylene-type molecules (abbreviated PI, see Fig. 7) in ultra low dopant concentration ($c_{PI} \simeq 10^{-10}$ mol/l) served as an active medium between the resonator mirrors.

The measurements were performed at room temperature with the setup introduced in chapter 1.3 and sketched in Fig. 1. Using confocal microscopy and spectroscopy, we spatially addressed single PI-molecules within the microresonator and determined the local mirror spacing L as discussed in chapter 2. For recording the time-resolved fluorescence decay curves of single molecules, the setup was equipped with an ultrafast pulsed laser system and a single photon counting board as described in chapter 1.3.

3.3 Microresonator-Controlled Spontaneous Emission Rate

Fluorescence Decay Curves and Spontaneous Emission Rate

In Fig. 12(a), typical fluorescence decays recorded for two different single dye molecules and different mirror spacings L are shown. Both transients were found to be mono-exponential and were fitted by single exponential decay functions $A \exp^{-t/\tau_{meas}} + B$ convoluted with the instrument response function ($FWHM_{irf} \simeq 500$ ps). For molecule 1, the excited state lifetime τ_{meas} was determined to be (2.0 ± 0.2) ns while for molecule 2 it was found to be significantly longer, at (3.8 ± 0.2) ns. The measured lifetime $\tau_{meas} = \Gamma_{meas}^{-1}$ results from the sum of radiative and non-radiative decay channels and the radiative rate for different mirror spacings L can be calculated according to

$$\Gamma_{SpE}(L) = \Gamma_{meas}(L) - \Gamma_{nr} = \Gamma_{meas}(L) - (1 - Y_0)\Gamma_{meas,0} \qquad (2)$$

where Y_0 is the fluorescence quantum yield of the molecule. The non-radiative rate Γ_{nr} is determined by intramolecular processes such as inter-system crossing and internal conversion. Therefore, Γ_{nr} is not affected by the presence of the photonic modes of the microresonator and thus independent of the mirror spacing L. As a reference, the fluorescence rate and quantum yield of PI-molecules in free space, i. e. in a microresonator of the same type as that one reported in chapter 2, just without silver mirrors, was determined independently to be $\Gamma_{meas,0} = 1 / (4.2 \pm 0.2)$ ns and Y_0 = 0.75 ± 0.05, respectively. The free space value $\Gamma_{SpE,0}$ was measured for dye concentrations varying over three orders of magnitude applying the same time-resolved spectroscopy technique. The bulk fluorescence quantum yield Y_0 of PI-molecules dissolved in dichloromethane as well as embedded in the cured polymer was measured applying standard methods using Rhodamin 6 G dye as a reference [67].

In Fig. 12(b), the measured rates Γ_{SpE} for 57 different molecules are presented together with theoretical predictions. Γ_{SpE} can be calculated directly from Fermi's golden rule [41]

$$\Gamma_{SpE} = 1/\tau_{SpE} = \frac{2\pi}{\hbar^2}|\langle|\hat{\mu} \cdot \hat{E}_{cav}^+|\rangle|^2 \rho_{cav}(\omega) \qquad (3)$$

taking into account the modification of either the density of states of the electromagnetic field ρ_{cav} or the electric field operator $\hat{E}_{cav}^+$ in the presence of the microresonator and both treatments lead to the same results. We followed the approach presented by Björk and Yamamoto [3] assigning
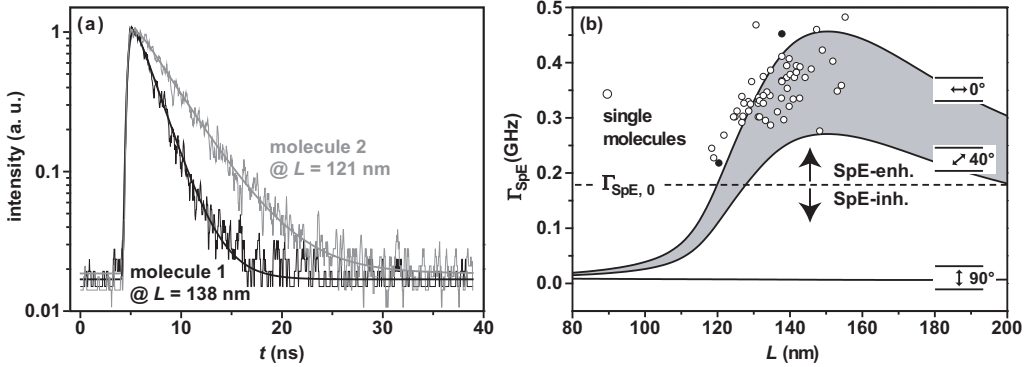
Figure 12: (a) Fluorescence decays of two individual molecules embedded in the $\lambda/2$-microresonator for different mirror spacings L. Both transients were modeled using single exponential decay functions (smooth lines). The resulting lifetimes τ_{meas} are 2.0 ns and 3.8 ns, respectively. (b) Measured microresonator-controlled fluorescence decay rates (circles) for 57 molecules at different mirror spacings L. The solid curves show the theoretical values calculated for parallel ($\theta = 0^o$), tilted ($\theta = 40^o$) and perpendicular ($\theta = 90^o$) orientation of the molecular transition dipole moment with respect to the resonator mirrors at the position $z = 0$ (see Fig. 13). The SpE-rates derived from the decays shown in (a) are indicated by dots.

the variations of Γ_{SpE} to the modification of the vacuum fluctuations associated with an electrical field entering the microresonator. For a given L, $\Gamma_{SpE}(L, \theta)$ is predicted to peak for a transition dipole orientation parallel to the microresonator plane ($\theta = 0^o$ in Fig. 13) and to decrease to nearly zero following

$$\Gamma_{SpE}(L, \theta) = \Gamma_{SpE}(L, \theta = 0^o)\cos^2(\theta) + \Gamma_{SpE}(L, \theta = 90^o)\sin^2(\theta) \quad (4)$$

The calculated Γ_{SpE} for three different dipole orientations parallel ($\theta = 0^o$), tilted ($\theta = 40^o$) and perpendicular ($\theta = 90^o$) to the resonator mirrors at the $z = 0$ position are shown in Fig. 12(b) as solid lines. In our calculations, the reflection and transmission coefficients of the resonator mirrors are calculated as functions of the silver film thickness $d_{1,2}$, the incidence angle ϑ, and the wavelength λ based on the dielectric function of silver [2, 39]. The ability of the molecules to emit photons at different wavelengths was taken into account by summing the Spontaneous Emission rates for the different wavelengths $\Gamma_{SpE}(L, \lambda)$ weighted by $f(\lambda)$, the measured and normalized free-space PI fluorescence spectrum as shown in Fig. 7, resulting in
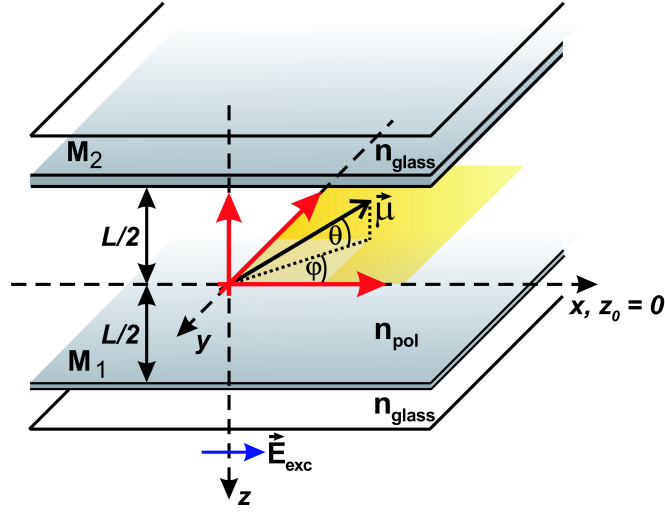
Figure 13: Schematic of the microresonator geometry containing the relevant coordinate system and notations as discussed in the text. The transition dipole $\vec{\mu}$ represents a single molecule.

$$\Gamma_{SpE}(L) = \sum \Gamma_{SpE}(L, \lambda) f(\lambda) \tag{5}$$

Note that this model calculation predicts the experimentally determined rates $\Gamma_{SpE}(L)$ without accounting for free parameters. Our single molecule data is found to nicely agree with the theoretical curves with values between those predicted for transition dipole orientations $0^o \leq \theta \leq 40^o$ placed at $z = 0$ in the microresonator (grey shaded area in Fig. 12(b)). The highest observed enhancement factor $\Gamma_{SpE}/\Gamma_{SpE,0}$ of about 2.7 is close to the maximum value predicted from theory.

Spreading of Spontaneous Emission Rates

Obviously, the spreading of measured Γ_{SpE} for the single molecule data increases with increasing L. In general, variations in Γ_{SpE} could be caused by different z-positions of the molecules within the resonator and different orientations with respect to the mirror planes (angle θ in Fig. 13). The polar angle ϕ, which is determined by the projection of the transition dipole moment vector $\vec{\mu}$ onto the electric field vector which is linearly polarized in the (x-y)-plane of the microresonator (see Fig. 13), only has an influence on the absorption efficiency and hence fluorescence intensity of the molecules. Since the intensity distribution of both the excitation and emission field

scales with $cos^2(2\pi n_{pol}z/\lambda)$ inside the microresonator, a successive decrease of excitation power allows the addressing of molecules predominantly near the ($z = 0$)-plane in the center of the microresonator.

Furthermore, dye molecules within a distance of up to ten nanometers from the resonator mirrors will loose their excitation energy predominantly via radiationless transfer to the silver films [68]. Indeed, experiments on Eu^{3+}-monolayers embedded in silver-clad microresonators showed that the measured fluorescence lifetimes does not vary significantly (< 10 percent) under z-displacement inside the microresonator until the onset of fluorescence quenching near the silver mirrors [50].

Therefore, we attribute the observed spreading of rates Γ_{SpE} mainly to variations of the angle θ included by the molecular transition dipole moment $\vec{\mu}$ and the (x-y)-plane of the microresonator (see Fig. 13). It should be mentioned that the observed spreading in Γ_{SpE} could also be modeled assuming parallel dipole orientation ($\theta = 0^o$) and emitter displacements of $\pm$ 30 nm from the ($z = 0$)-plane in the center of the microresonator. For our experiment this means that for mirror spacings around 120 nm, which is close to the SpE-inhibition regime (see Fig. 12(b)), the resonance condition Eqn. 1 can be matched only by molecules with transition dipoles nearly parallel to the resonator mirrors $M_{1,2}$.

In contrast, as L increases, the resonance condition can be fulfilled also for transition dipole orientations deviating from $\theta = 0^o$ maintaining sufficient radiation efficiency to allow for single molecule detection. The fluorescence decays obtained from single molecule emission thereby reflect different but sufficient advantageous transition dipole orientations which leads to an enhanced Γ_{SpE} with respect to the value $\Gamma_{SpE,0}$ in free space.

3.4   Fluorescence Lifetime Imaging

To visualize the orientational dependence of fluorescence lifetimes and intensities, a FLIM-type (Fluorescence Lifetime Imaging) representation of the measured data is presented in Fig. 14. As an example, the transition dipole orientations of three different molecules calculated by Eqn. 4 are indicated by an arrow. Molecule (a) meets the theoretical prediction for lying at $z = 0$ with a transition dipole moment nearly parallel to the resonator mirrors, that is $\theta_a = 0^o$. On the other hand, regarding the corresponding mirror spacings L, molecule (b) and (c) show fluorescence lifetimes τ_{meas} that indicate $\theta_b = 27^o$ and $\theta_c = 43^o$, respectively.
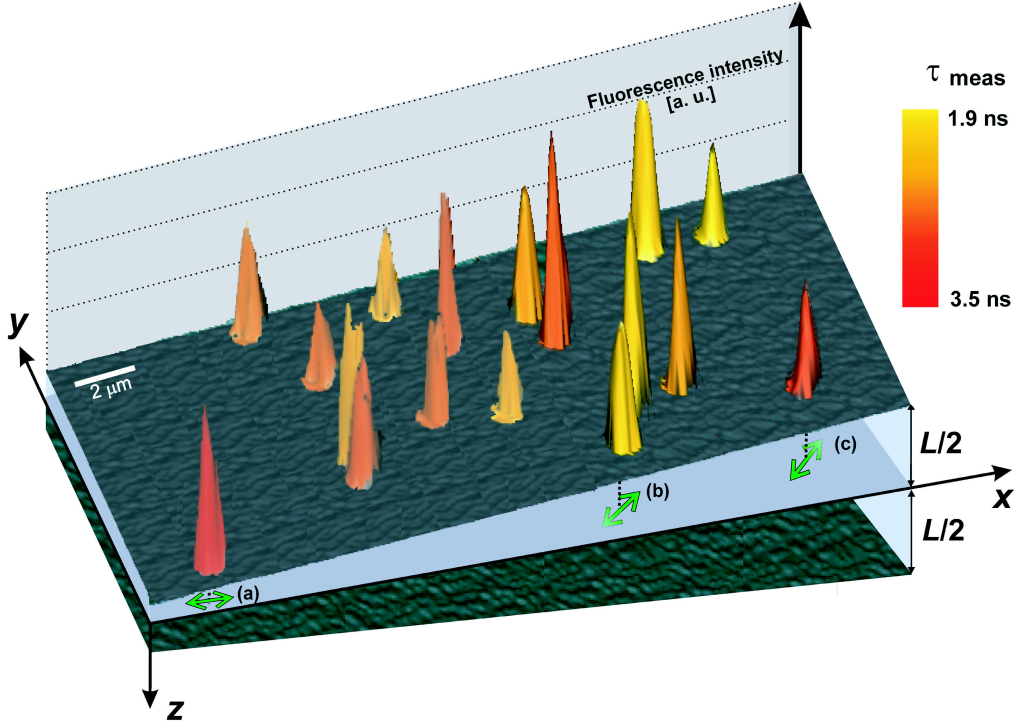
Figure 14: FLIM-type representation showing the measured fluorescence intensity and the variation of single molecule fluorescence lifetimes τ_{meas} with mirror spacing L at different resonator positions (x, y). The arrows in the $(z = 0)$-plane indicate positions and calculated orientations ($\theta_a = 0^o$, $\theta_b = 27^o$ and $\theta_c = 43^o$) of transition dipole moments for three different PI-molecules (a), (b) and (c).

3.5 Detection Efficiency for On- and Off-Axis Emission

The L-regime between roughly 120 nm and 160 nm for which single molecule decay curves could be detected corresponds to the width of the bright ring in Fig. 10(a). For larger L, single molecule detection was not possible despite the increased rate Γ_{SpE} because of the transmission properties of the microresonator given by Eqn. 1: For a fixed wavelength λ, an increasing L can only be compensated by an increasing ϑ which effectively introduces off-axis emission. However, since the reflectivities of the silver mirrors as well as the collection efficiency of the experimental setup vary strongly with ϑ, the detection efficiency for off-axis emission can be considerably reduced.

This means that also the spectral shape of microresonator-controlled emission is expected to depend strongly on the mirror spacing L as well as on the detection conditions. This is investigated in detail in chapter 4:

30

There, we show how the spectral distribution of collected fluorescence emission can be calculated as a function of the mirror spacing L by filtering the microresonator-controlled fluorescence emission determined by $\Gamma_{SpE}(L)$ using Fabry-Perot-theory [2].

3.6 Transverse Correlation Length and Intermolecular Distance

For the dye concentrations used in our single molecule experiments, the average intermolecular distance within the microresonator is estimated to be around 2 μm as supported by confocal microscopy images (see Fig. 10(b)). In the following, we compare the intermolecular distance with the transverse quantum correlation length l_m which is a measure for the microresonator-mediated intermolecular coupling length in our planar microresonator system [37, 63]:

$$l_\mathrm{m} = \frac{2\lambda(x,y)}{n_{pol}}\sqrt{\mathrm{m}f} \quad , \quad f = \frac{\pi(R_1 R_2)^{1/4}}{1 - \sqrt{R_1 R_2}} \tag{6}$$

Here, $\lambda(x,y)$ is the wavelength at the transmission maximum of the microresonator (see also chapter 2), n_{pol} is the refractive index of the polymer film between the resonator mirrors $\mathrm{M}_{1,2}$ having the reflectivities $R_{1,2}$ and m is the interference order. For a $\lambda/2$-microresonator with silver mirror thickness $d_1 = 30$ nm and $d_2 = 60$ nm, we use $R_1 = 0.71$, $R_2 = 0.91$ and m = 1 and calculate l_1 assuming $\lambda(x,y) = 532$ nm. f is the finesse of a planar resonator [2] which has a value around 14 in the present case. As a result, we obtain $l_1 \simeq 2.58$ μm which can be considered as the theoretical upper limit of the coupling length in our microresonator. This value is comparable to the intermolecular distance in our microresonator sample as discussed above. In view of our results, however, we conclude that microresonator-mediated molecular coupling is negligible here. This conclusion will be further confirmed in chapter 6: There, we will compare the transverse quantum correlation length l_1 as discussed here with the measured and calculated diameter of spatial modes of our $\lambda/2$-microresonator.

It should be mentioned that we also observed few fluorescence decay curves showing more than one fluorescence lifetime contribution. This can easily be understood assuming sudden changes in the interaction of the molecule with its local environment during data acquisition time.

3.7 Summary and Conclusion

In summary, we presented fluorescence decay curves of single molecular dipole emitters interacting at room temperature with photonic modes of a planar $\lambda/2$-microresonator having a cavity-Q around 50. Enhancement factors $\Gamma_{SpE}/\Gamma_{SpE,0}$ of up to 2.7 were determined from mono-exponential fluorescence decay curves delivered by single dye molecules, in agreement with theoretical predictions.

The microresonator-enhanced Spontaneous Emission rate as well as the microresonator-enhanced coherence length of single molecule fluorescence emission as reported in chapter 2 (see Fig. 11) can be considered as important improvements for single photon sources based on single dye molecules operating at room temperature. In chapter 5, we will investigate if both enhancements can be used simultaneously.

4 The Spectral Shape of Microresonator-Controlled Molecular Fluorescence

In this chapter, we investigate experimentally and theoretically the spectral shape of fluorescence emission of dye molecules coupled to the photonic mode structure of a planar $\lambda/2$-microresonator by varying the emitter concentration and the mirror spacing. The spectral shape of the outcoupled emission is modeled by summing radiative on- and off-axis contributions depending on the mirror spacing. Good agreement was found between experimental results and simulations taking into account the complex interplay between focussed pump field, broad free-space fluorescence spectrum of embedded molecules, microresonator properties and detection conditions.

4.1 Introduction

Over the last decade, planar microresonator structures turned out to be of great importance for the development of advanced organic light emitting devices (OLED) [13,69] and vertical cavity surface emitting lasers (VC-SEL) [70,71] as well as advanced single photon sources (SPS) [15]. It has been demonstrated experimentally, that weak coupling of quantum mechanical emitters (QME) to a $\lambda/2$-microresonator results in a temporal modulation, i. e. enhancement and inhibition of Spontaneous Emission (SpE)) [49,50], as well as an angular redistribution of the emitted light [39,50] what has to be taken into account for the design of advanced photonic devices.

Importantly, we found that emission of embedded QME is spectrally redistributed (see Fig. 11) to fulfill the transmission conditions of the resonator depending on the mirror spacing (see Eqn. 1). This effect is of major significance for broadband-QME such as organic dye molecules or semiconductor quantum dots for which the spectral width of free-space emission exceeds the width of the resonator transmission spectrum. Surprisingly, this effect is not treated sufficiently in the literature.

All three effects, namely temporal, angular and spectral redistribution, are based on the microresonator-controlled SpE-rate of embedded QME as discussed in chapter 3 and can be calculated using first order perturbation theory [3,72].

In the following, we clarify the correlation between mirror spacing, on- and off-axis resonances and the spectral shape of microresonator-controlled broadband emission for our microresonator system and discuss the influence of the detection conditions.

4.2 Experimental

The microresonator samples were formed by two resonator mirrors $M_{1,2}$ with a silver film thickness of 30 nm and 60 nm, respectively, resulting in a cavity-Q around 50 in the $\lambda/2$-regime (see chapter 2). As an active medium between $M_{1,2}$, a transparent polymer ($n_{pol} = 1.56$) doped with uniformly distributed and randomly oriented perylene-type molecules (abbreviated PI, see Fig. 7) in high ($c_{PI} \simeq 10^{-5}$ mol/l) and ultra low ($c_{PI} \simeq 10^{-10}$ mol/l) concentrations was used.

The measurements were performed at room temperature with the setup introduced in chapter 1.3 and sketched in Fig. 1. Using scanning confocal mi-
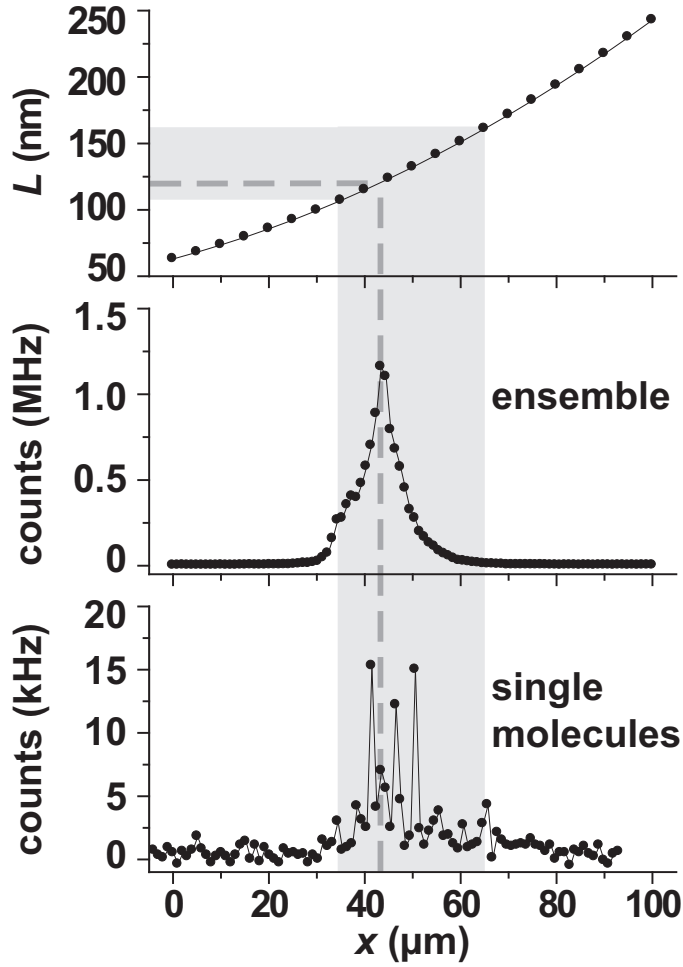
Figure 15: Profile of the mirror spacing $L(x)$ (upper curve) of the microresonator in the $\lambda/2$-regime. Corresponding measured fluorescence intensity $I(x)$ for high (middle curve) and ultra low (lower curve) dye concentration.

croscopy and spectroscopy, we spatially addressed PI-molecules immobilized within the microresonator and recorded the integrated fluorescence intensity under variation of the mirror spacing L as described in chapter 2. In a second step, we measured both the microresonator-controlled molecular fluorescence spectra and the corresponding local on-axis transmission spectra of the microresonator as a function of the mirror spacing L.

4.3 Output for Varying Mirror Spacing and Dopant Concentration

We discuss now the correlation between the local mirror spacing $L(x)$ and the integrated fluorescence intensity, i. e. the output, for two representative molecular concentrations. The mirror spacing $L(x)$ can be calculated from the maximum transmission wavelength $\lambda(x)$ of the measured local on-axis transmission spectrum (see Fig. 18(a), middle panel) for every position x of the microresonator according to Eqn. 1. This procedure results in a profile of the mirror spacing as shown in Fig. 15, upper curve, and was already discussed in detail in chapter 2.

The corresponding fluorescence intensity traces $I(x)$ also shown in Fig. 15 were acquired by scanning microresonators having different dopant concentrations along the x-axis with respect to a fixed immersion oil objective (100x, $NA = 1.3$) as indicated in Fig. 1. They can be understood as line sections of a respective scan image as shown in Fig. 10(a): In the case of high molecular concentrations, the measurement reveals a section of a closed fluorescent ring without spatial fine structure.

The fluorescence scan of a microresonator with high molecular concentration (see Fig. 15, middle curve) shows a sharp maximum, if $\lambda(x)$ overlaps with the free-space fluorescence spectrum of the dye as shown in Fig. 18, upper spectrum. This spectrum was measured with a comparable sample as discussed above, just without silver mirrors.

For single molecule doping, the scan (Fig. 15, lower curve) exhibits fluorescence bursts for several positions x where the fluorescence emission of spatially isolated single molecules is on resonance with the structure. The grey background indicates the L-regime where single molecule emission was above the detection limit of the experimental setup.

4.4 On-Axis Transmission versus Molecular Emission

In Fig. 16(a), measured and calculated on-axis transmission spectra of the microresonator (m =1 and $\vartheta = 0^o$ in Eqn. 1) as a function of the mirror spacing L are shown. Good agreement was found between experimental and calculated spectra. For comparison, two cross sections from the plots shown in Fig. 16(a) taken at $L = 120$ nm are shown in the middle panel of Fig. 18(a): As a result, the on-axis intensity transmission of the microresonator calculated as a function of the wavelength, i. e. the well-known Airy-function [2], nicely agrees with the corresponding measured local on-axis transmission spectrum. For the calculation of the on-axis transmission spectra discussed
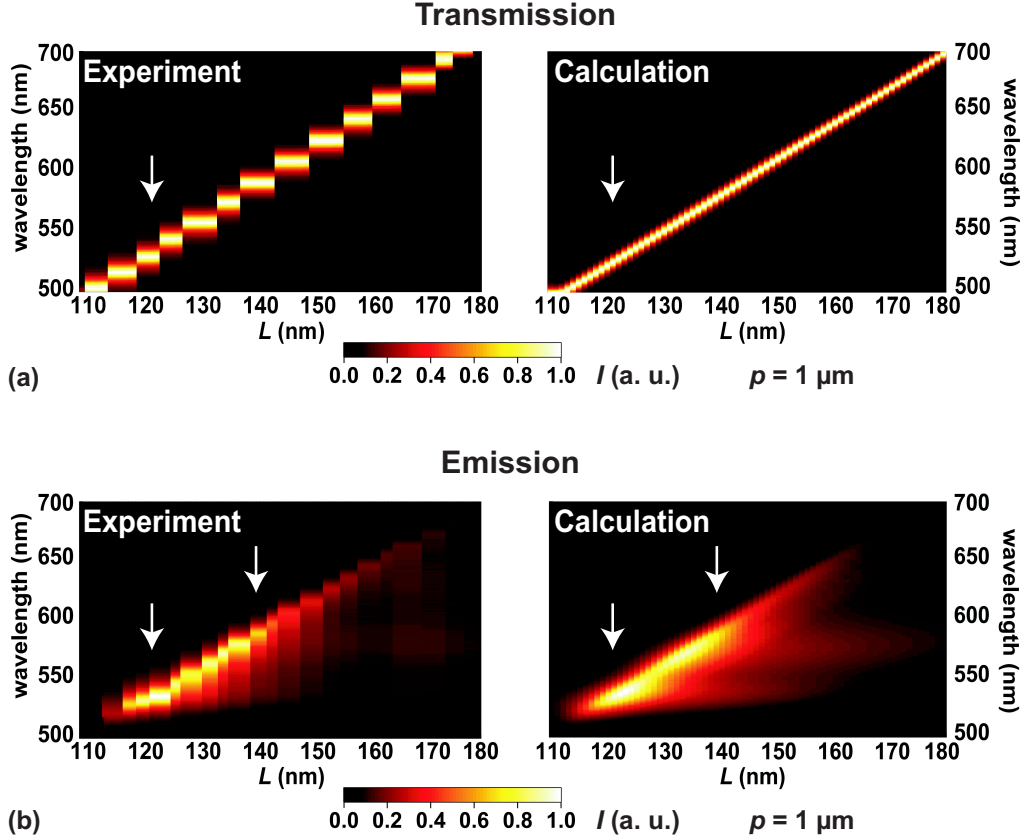
Figure 16: (a) Measured and calculated on-axis transmission spectra of the microresonator as function of the mirror spacing L. (b) Measured and calculated spectral distribution of the microresonator-controlled fluorescence emission as function of L. The white arrows in (a) and (b) indicate the cross sections that are shown in Fig. 18 and discussed in the text.

here, we assumed a parallel polarization of the incident optical field with respect to the plane of the metal mirrors $M_{1,2}$ (see Fig. 13).

In the left panel of Fig. 16(b), a spectrally resolved fluorescence scan is shown measured for high dye concentration. The bright diagonal stripe reflects the proportional relation between $L(x)$ and $\lambda(x)$ for on-axis resonances as can be seen by comparison with the corresponding series of on-axis transmission spectra of the microresonator shown in Fig. 16(a). Obviously, the spectral distribution broadens significantly with increasing L. In the following, we discuss how this variation in spectral shape can be quantified.

Modeling the spectral shape of the microresonator-controlled emission is

37

divided into four major steps. Note, that the first two steps have already been introduced in chapter 3 to calculate the curves $\Gamma_{SpE}(L)$ as shown in Fig. 12(b).

1. The reflection and transmission coefficients of the resonator mirrors are calculated as functions of d, ϑ, λ based on the dielectric function of silver [2, 39].

2. For each mirror spacing L, we calculate the radiative rates for single dipole emitters located in the center $z = 0$ of the microresonator and oriented in $i = x, y, z$ direction (see Fig. 13) as a function of ϑ and λ according to [3, 12]. The resulting rates $\Gamma_i(\lambda, L)$ are weighted by the normalized free-space fluorescence spectrum of the dye, $f(\lambda)$ (see Fig. 18(a), upper spectrum).

3. The detectable radiation contribution is obtained by filtering the sum of radiative rates for the three dipole orientations $\sum \Gamma_i(\lambda, L) f(\lambda)$ using Fabry-Perot-theory [2]. In this step, the limitation of the detection angle is included using a simplified optical model. ϑ_{max} is either given by the NA of the microscope objective or by the observation diameter p on the microresonator (see Fig. 17), depending on the emission direction of the radiation produced in the structure. The observation diameter p is determined by the pinhole size and the magnification of the microscope objective (see also Fig. 1). This can be understood as follows: For axial radiation, the number of roundtrips within the microresonator is only limited by the losses of the mirrors and the polymer film, respectively. Radiation emitted off-axis, on the other hand, can walk off the observation area that is determined by p within a small number of internal reflections. This is modeled by summing the emitted radiation in truncated geometrical series where the maximum number of roundtrips (i. e. the upper limit of the series) depends on L, ϑ and λ, respectively (see Eqn. 1).

4. The efficiency of molecular absorption strongly depends on the excitation field distribution inside the microresonator. Therefore, the calculated spectra are scaled by the strength of the linearly polarized and focussed pump field at $z = 0$, which was modeled as a function of L.

Results of our calculations are presented in Fig. 16(b) nicely reproducing the experimental spectra. Representative spectra at $L = 120$ nm and $L = 140$ nm, respectively, are shown in the lower panels of Fig. 18(a) and (b). For
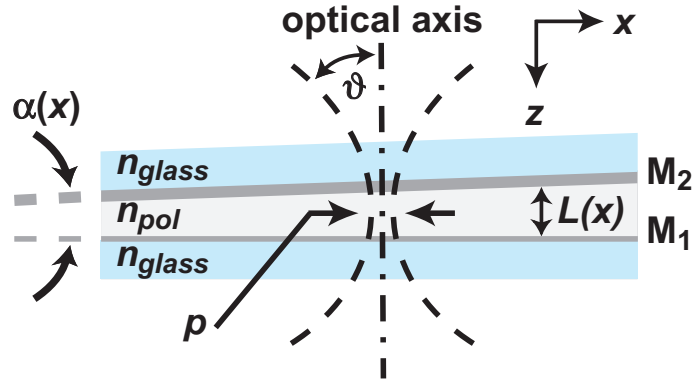
Figure 17: Schematic of the microresonator geometry in the focal region (curved dashed line) of the microscope objective. The size of the pinhole as shown in Fig. 1 determines the diameter p of the observation area. Within an observation diameter p around 1 micron, the microresonator acts as a planar microresonator in a good approximation since the tilt angle between the resonator mirrors $M_{1,2}$ is very small ($\alpha(x) \simeq 10^{-3} - 10^{-2}$).

$L = 120$ nm, the free-space fluorescence spectrum of the dye is redistributed and nearly samples the spectral shape of the local on-axis transmission profile of the microresonator. A maximized spectral narrowing is accompanied by a maximum detection efficiency in full agreement with the corresponding intensity trace $I(x)$ (Fig. 15, middle curve) and the numerical results (see Fig. 16(b)). Here, the spectral shape of the outcoupled emission was found to be insensitive to variations of the observation diameter p since radiation is predominantly emitted in forward direction. For this L, the on-axis emission field density within the resonator is maximized supporting non-linear effects like lasing. To clarify the correlation between $\Gamma_{SpE}(L)$ and the efficiencies for both output and Stimulated Emission will be the main objective of chapter 5.

The increased spectral width for $L = 140$ nm (see Fig. 18(b)) originates from off-axis resonances on the blue side of the spectrum as indicated by the dashed line. Apparently, the detection of the off-axis emission can be suppressed by reducing the observation diameter p, i. e. by spatial filtering the outcoupled radiation.

It should be mentioned that the modeling scheme presented here can be applied to microresonators made of dielectric thin films (i. e. distributed bragg reflectors). Accounting for resonator-mediated molecular coupling processes [37,66] could further improve modeling accuracy.
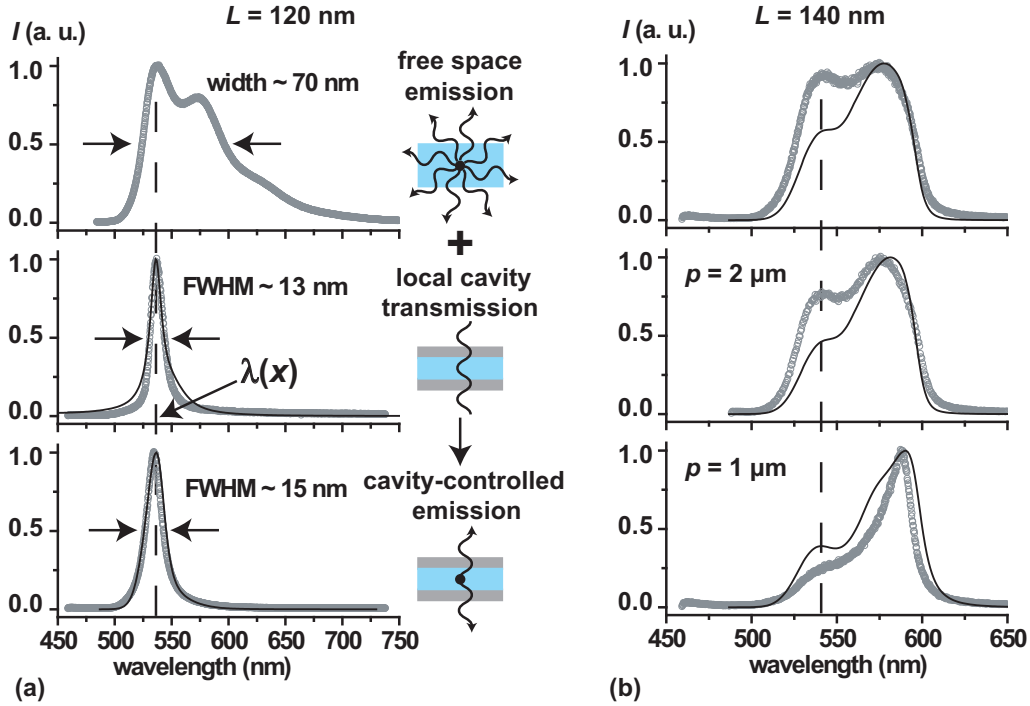
Figure 18: (a) For $L = 120$ nm, the free space fluorescence spectrum of the dye (upper curve) is modified and samples the spectral shape of the local on-axis transmission profile of the microresonator (middle curves, circles: measurement, line: calculation). The resulting microresonator-controlled emission spectrum is shown below (circles: measurement, line: calculation). (b) For $L = 140$ nm, the modification of the spectral shape of detected microresonator-controlled fluorescence emission under variation of the observation diameter p on the microresonator structure is shown (circles: measurement, line: calculation). For the upper spectra, no pinhole was used. The middle and lower spectra correspond to a pinhole diameter of 200 µm and 100 µm, respectively. The middle and lower spectra in (a) as well as the lower spectra in (b) are cross sections of the respective plots in Fig. 16 as indicated there by the white arrows.

4.5 Single Molecule Fluorescence Spectra for Varying Mirror Spacing

In Fig. 19, microresonator-controlled single molecule fluorescence spectra for three different mirror spacings measured without pinhole are shown. Their shape was modeled assuming in-plane dipole orientations (see Fig. 13) showing excellent agreement. The occurrence of the off-axis emission for increasing

40
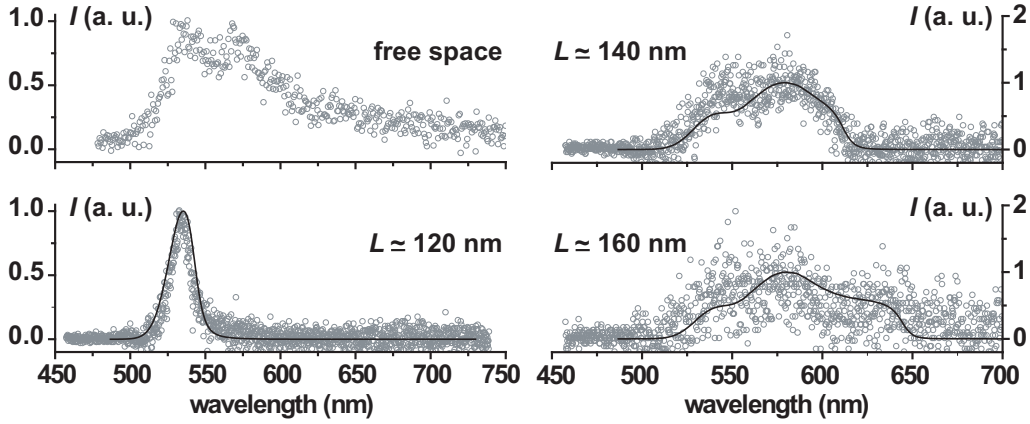
Figure 19: Measured (circles) and calculated (line) microresonator-controlled single molecule fluorescence spectra for three different mirror spacings L. A measured free-space single molecule fluorescence spectrum is also shown as reference.

L leads to a spectral broadening until the signal to noise ratio drops below the detection limit of the experimental setup, in agreement with the integrated fluorescence intensity trace shown in the lower panel of Fig. 15.

4.6 Summary and Conclusion

In summary, we compared measured and calculated on-axis transmission spectra of a planar $\lambda/2$-microresonator with the corresponding microresonator-controlled fluorescence emission spectra of embedded dye molecules as a function of the mirror spacing L. The spectral shape of the detected fluorescence emission was modeled accounting for the optical properties of the resonator mirrors, the radiative properties of the embedded emitters in free space (i. e. their radiative rate, their fluorescence spectrum and their fluorescence quantum yield) and the detection conditions without the need for free parameters.

Our results allow for tailoring emission/detection schemes based on microresonators and broadband-QME for applications in photonics and ultra sensitive analytics.

5 Spontaneous Emission Rate, Output and Stimulated Emission Efficiency in a $\lambda/2$-Microresonator

In this chapter, we investigate experimentally and theoretically the fluorescence dynamics of dye molecules immobilized in a planar $\lambda/2$-microresonator for varying emitter concentrations. Time-resolved spectroscopy reveals enhancement and inhibition of radiative rates determined by the mirror spacing in agreement with simulation results. The maximum output efficiency, however, occurs for mirror spacings where no rate modification is observed and coincides with the maximum of Stimulated Emission efficiency which was probed by means of output fluctuations.

5.1 Introduction

To summarize the previous chapters, we proofed that the weak coupling of quantum mechanical emitters (QME) having a broad emission spectrum to the photonic mode structure of a $\lambda/2$-microresonator results in a significant temporal, spectral and angular redistribution of the emitted radiation. We demonstrated in chapter 4, that all three processes are completely determined by the microresonator-controlled Spontaneous Emission (SpE) rate Γ_{SpE} and can be calculated, even for single single dye molecules, using first order perturbation theory.

In contrast, both output and Stimulated Emission (StE) efficiency, which are key parameters for advanced photonic applications such as single photon sources and microlasers, e. g. [14, 15], are not only determined by Γ_{SpE}, they also depend on the coupling ratio β which is defined as the SpE into a desired cavity mode normalized to the total SpE produced in the structure [50, 65, 66, 73–77].

Importantly, in the case of broadband-QME, both angular and spectral dependencies of the radiative rate and the outcoupled emission have to be considered as a function of the mirror spacing. Experimental investigations, however, of how both the output and the StE-efficiency are determined by Γ_{SpE} and β as functions of L are lacking in the case of broadband-QME.

5.2 Experimental

The microresonator samples consisted of two resonator mirrors $M_{1,2}$ with a silver film thickness of 30 nm and 60 nm, respectively, resulting in a cavity-Q around 50 in the $\lambda/2$-regime (see chapter 2). As an active medium between $M_{1,2}$, a transparent polymer ($n_{pol} = 1.56$) doped with uniformly distributed and randomly oriented perylene-type molecules (abbreviated PI, see Fig. 7) in high ($c_{PI} \simeq 10^{-5}$ mol/l) and ultra low ($c_{PI} \simeq 10^{-10}$ mol/l) concentrations was used.

The measurements were performed at room temperature with the setup introduced in chapter 1.3 and sketched in Fig. 1. Using confocal microscopy and spectroscopy, we spatially addressed PI-molecules and determined the local mirror spacing L as discussed in chapter 2. For recording time-resolved fluorescence decay curves of single molecules as well as molecular ensembles, the setup was equipped with an ultrafast pulsed laser system and a single photon counting board as described in chapter 1.3.
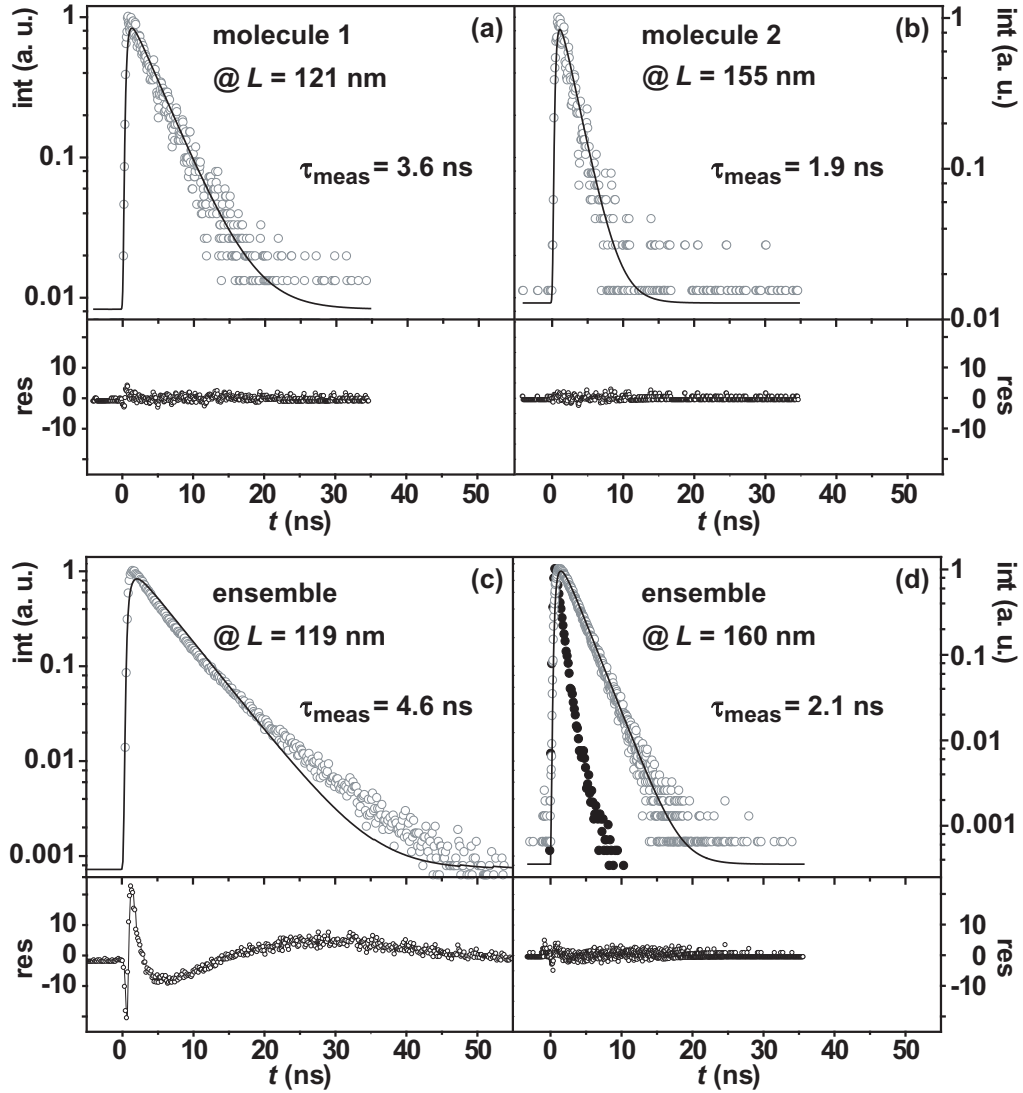
Figure 20: Measured (circles) and fitted (lines) microresonator-controlled fluorescence decays for single molecules (a), (b) and molecular ensembles (c), (d) for representative mirror spacings L. The residuals below show deviations between measured decays and single exponential model functions convoluted with the instrument response function (dots in (d)). In (c), the fit with a single exponential is used to derive an average decay time for comparison.

44

5.3 Fluorescence Dynamics

In Fig. 20, typical experimental fluorescence decays for single molecules as well as molecular ensembles at different mirror spacings L are shown. Single exponential model functions convoluted with the instrument response function (dots in Fig. 20(d), $FWHM_{irf} \simeq 500$ ps) were fitted to the experimental decay curves. The resulting SpE-rates are shown in Fig. 21(a) together with theoretical predictions. The lines show calculated rates for PI-molecules located in the center of the microresonator for three representative transition dipole orientations θ (see Fig. 13) as already discussed in chapter 3 and shown in Fig. 12(b).

Spatially isolated molecules show mono-exponential decay curves (see Fig. 20 (a), (b)) and Γ_{SpE}-values depending on the mirror spacing. As shown in Fig. 21(a), different molecules can have different SpE-rates for the same L reflecting a strong dependence on the angle θ between the transition dipole moment and the mirror planes of the resonator (see Fig. 13) as well as a displacement from the microresonator center. Comparison of Γ_{SpE} for molecule 1 and 2 as derived from the curves shown in Fig. 20 (a) and (b) with the theoretical curves reveal that both molecules are located in the center of the microresonator and oriented parallel to the mirror planes ($\theta = 0^o$ in Fig. 13).

For molecular ensembles, variation of the mirror spacing results in the well-known SpE-rate modulation [49], i. e. SpE-enhancement [42] and SpE-inhibition [44], respectively. Even though transition dipole moments with $\theta \neq 0^o$ are excited in our experiment as can be seen from our single molecule data, the fluorescence decays of molecular ensembles are obviously determined by molecules having $\theta = 0^o$ that offer the fastest decay rates. This fact combined with the observation of mono-exponential decay for ensembles of randomly oriented emitters (see Fig. 20(d)) indicates a very efficient coupling mechanism between excited molecules mediated by the microresonator [37].

We attribute the occurrence of mono-exponential fluorescence decay in our system to a highly efficient and non-dispersive resonance energy homo-transfer mediated by the microresonator. The effect of the local density of states of the electromagnetic field on radiative and non-radiative energy transfer is discussed controversial in the literature, e. g. [78–84], and also subject of our ongoing investigations.

For L approaching 120 nm, we observe increasing deviations from strictly mono-exponential decay (see Fig. 20(c)). However, mono-exponential fit functions still provide a good approximation of the average decay time here. In the L-regime around 120 nm, mono-exponential fluorescence decays occur only for spatially separated single molecules (see Fig. 20(a)).
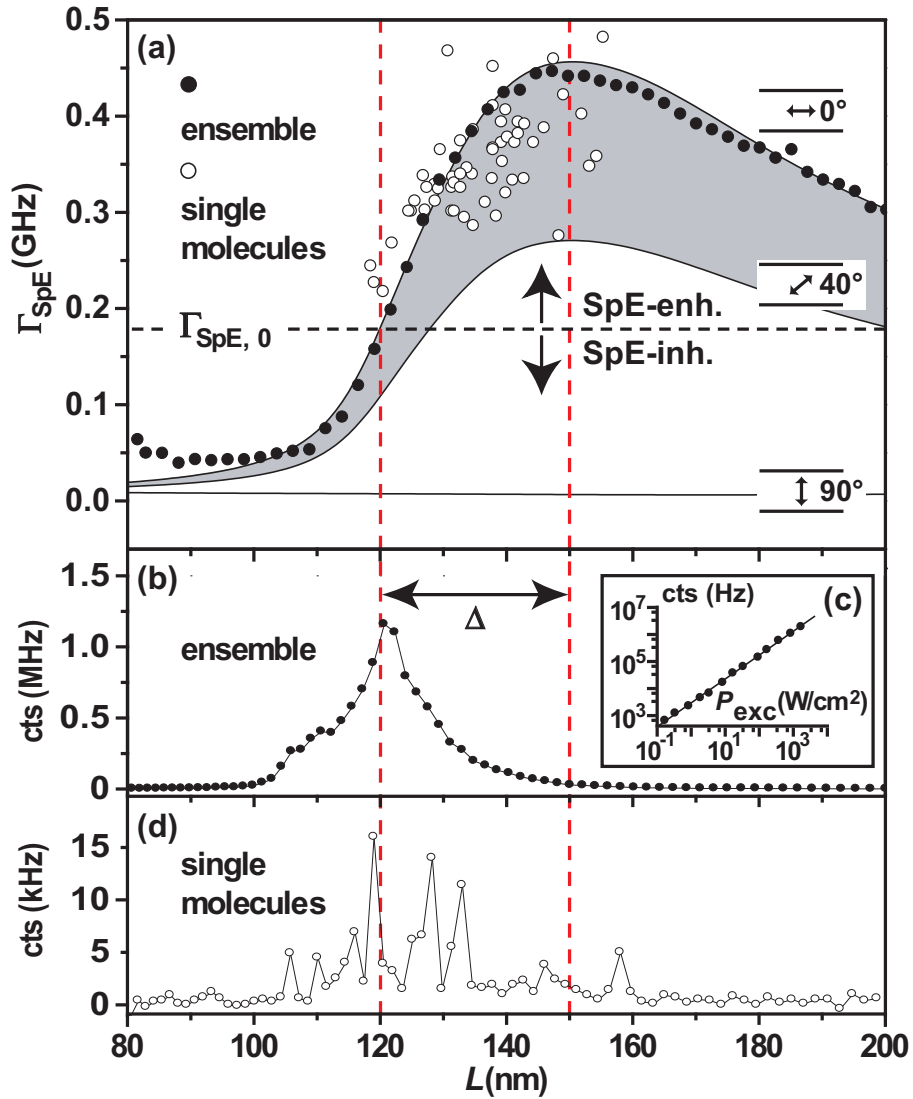
Figure 21: (a) Microresonator-controlled SpE-rates derived from fluorescence decays for PI-ensembles (dots) and for single PI-molecules (circles). Calculated SpE-rates (lines) for PI molecules centered in the microresonator and tilted with respect to the mirror planes by 0°, 40° and 90°, respectively. (b) Spectrally integrated fluorescence intensity for high dopant concentration. (c) Power dependence of detected fluorescence intensity at $L = 120$nm (dots) and a linear fit to the experimental data (line). (d) Spectrally integrated fluorescence intensity for ultra low dopant concentration shows isolated peaks originating from different molecules on resonance with the microresonator. The difference $\Delta = 30$ nm between the mirror spacings for maximum output efficiency and maximum enhancement of Γ_{SpE} is indicated by the double arrow.

The main result of our time-resolved measurements is that maximum Γ_{SpE} is observed at $L = 150$ nm for both molecular ensembles and single molecules.

5.4 Fluorescence Rate and Output Efficiency

In Fig. 21(b), the spectrally integrated fluorescence intensity along a line section through the microresonator is shown for high dopant concentration as a function of the mirror spacing. The signal shows a clear maximum at $L = 120$ nm. The intensity trace for ultra low dopant concentration (see Fig. 21(d)) exhibits fluorescence signals for sample positions and hence mirror spacings, where spatially isolated molecules are on resonance with the structure. The envelope of this fluorescence trace gives a fair estimate for the L-regime, where single molecule emission was above the detection threshold of the experimental setup.

The effect of the mirror spacing on the detected intensity and the spectral shape of microresonator-controlled emission was already discussed in chapter 4. In addition, the linear system response (see Fig. 21(c)) was verified for both cw and pulsed laser excitation up to the molecular saturation regime for all mirror spacings demonstrating that the microresonator operates well below lasing threshold. The key result here is the large difference Δ between mirror spacings for maximum output efficiency ($L = 120$ nm) and maximum enhancement of Γ_{SpE} ($L = 150$ nm) as indicated by dashed vertical lines in Fig. 21. A similar relationship between output efficiency and radiative rate was only discussed theoretically for a monochromatic emitter located inside a simple waveguide structure [77]. In the following section we demonstrate, that the maximum output efficiency coincides with the maximum of the radiation coupling ratio β.

5.5 The Coupling Ratio β

In Fig. 22(a), the calculated ratio β between SpE in the forward mode and the total SpE for a PI-molecule located in the center of the microresonator and oriented parallel to the mirrors is shown (see also Fig. 13). The forward mode is spectrally characterized by $\Delta\lambda = \lambda_{max} \pm 6.5$ nm, i. e. the $FWHM$ of the local on-axis transmission spectrum with maximum transmission wavelength λ_{max} (see Fig. 18(a), middle panel). The corresponding angular divergence $\Delta\vartheta$ is also determined by the reflectivities of the microresonator mirrors and was calculated as a function of the mirror spacing L based on the derivation presented in [65] which accounts for the resonance properties of a planar
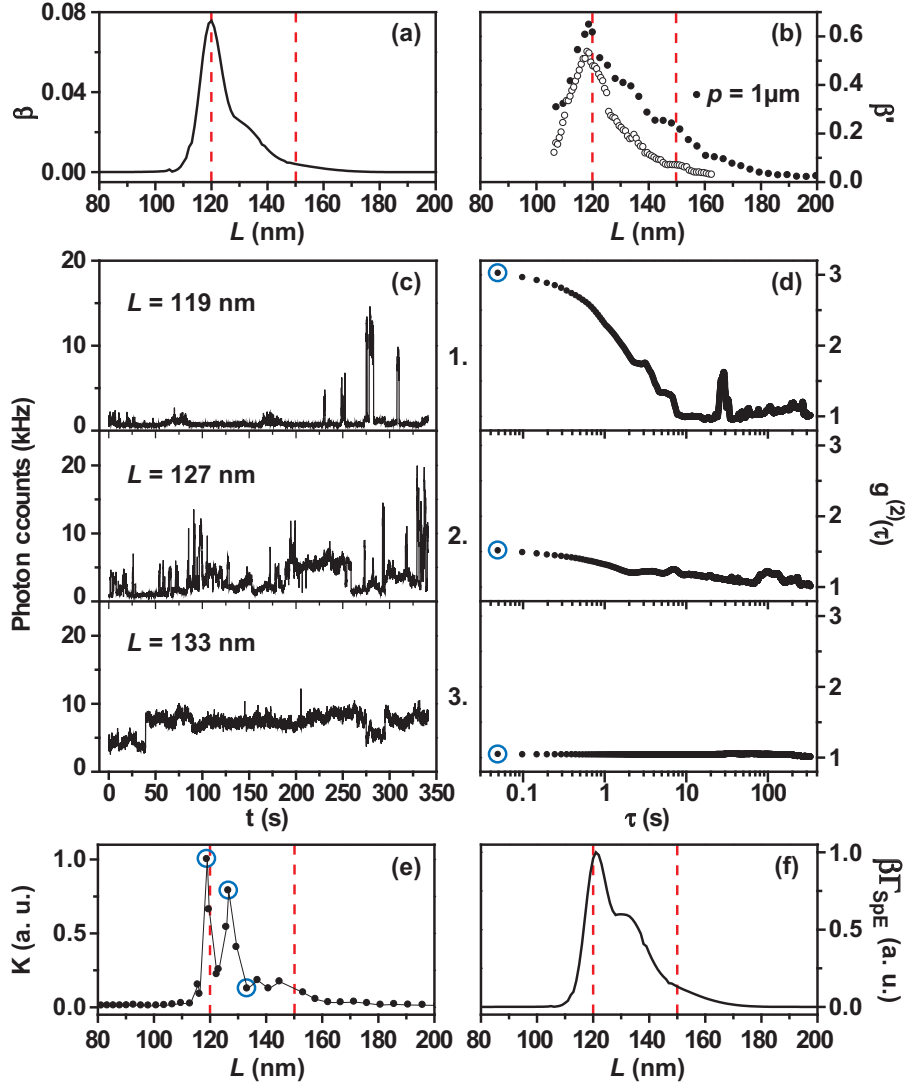
Figure 22: (a) Calculated coupling ratio β to the forward mode as a function of mirror spacing L. The shoulder around $L = 130$ nm reflects the vibronic progression of the free-space fluorescence spectrum of PI (see Fig. 7). (b) Experimental coupling ratio β' with (dots) and without (circles) restriction of the observation area as discussed in text. (c) Measured intensity traces and (d) corresponding intensity correlation $g^{(2)}(\tau)$ for three representative mirror spacings. (e) Fano-Mandel parameter K. Circles indicate data points derived from the corresponding values of $g^{(2)}(0)$ as shown in (d). (f) Product of theoretical curves β and Γ_{SpE} as described in text. The dashed lines in (a), (b), (e) and (f) indicate mirror spacings for maximum output efficiency ($L = 120$ nm) and maximum SpE-rate ($L = 150$ nm), respectively (see Fig. 21).

48

microresonator. Obviously, β peaks for $L = 120$ nm matching the mirror spacing for maximum output efficiency (see Fig. 21(b), (d)). For comparison, we estimated the experimental ratio β' (circles in Fig. 22(b)) from the overlap of the measured local on-axis transmission spectrum of the microresonator and the corresponding emission spectrum for each L as shown in Fig. 16. As expected, β' has larger values than β because not all radiation produced in the structure can be recorded in the respective emission spectra due to the limitation of the collection angle ϑ.

As discussed in chapter 4, we found that reducing the diameter of the observation area p on the microresonator reduces the detection efficiency for off-axis emission, equivalent to angular filtering by limiting ϑ: In Fig. 22(b), reduction of the observation diameter to $p = 1$ µm clearly increases β' (dots in Fig. 22(b)) due to blocked off-axis contributions in the corresponding emission spectra. The L-value for maximum β', however, is not affected and coincides with the mirror spacing for maximum β. Note, that the maximum of β' is equivalent to the maximum spectral narrowing as well as the minimum angular divergence of outcoupled radiation.

5.6 Output Fluctuations and Stimulated Emission Efficiency

Having determined the output maximum as well as the key parameters β and Γ_{SpE} as function of the mirror spacing L, we can now discuss their influence on the StE-efficiency. It is well known that microcavity lasers show strong output fluctuations depending on β and Γ_{SpE}, respectively, displaying the photon density in the lasing mode [85, 86]. Indeed, time traces measured on our microresonator exhibit strong intensity fluctuations as can be seen in Fig. 22(c). For this measurement, we used an intermediate dopant concentration ($c_{PI} \simeq 10^{-7}$ mol/l) and cw-pump power P_{pump} around 80 W/cm^2. The length of dark periods as well as the ratio between maximum and minimum intensities decreases from $L = 119$ nm to $L = 133$ nm. The time scale of the intensity fluctuations observed here is expected to be determined by the intersystem crossing rate and the lifetime of the dark molecular triplet state [87] which limits the efficiency of dye lasers. In Fig. 22(d), the corresponding intensity correlation functions calculated according to

$$g^{(2)}(\tau) = \langle I(t+\tau)I(t)\rangle/\langle I(t)\rangle^2 = \langle n(t+\tau)n(t)\rangle/\langle n(t)\rangle^2 \qquad (7)$$

are shown [88]. Here, n is the number of accumulated photon counts per time interval $\Delta t_{meas} = 50$ ms and the total acquisition time was $t_{meas} = 341$ s. Obviously, $g^{(2)}(0)$ (highlighted by circles in Fig. 22(d)) reflects the

magnitude of the output fluctuations. These fluctuations are associated with the second moment of the photon statistics and are typically quantified using the Fano-Mandel parameter $K = \langle n \rangle [g^{(2)}(0) - 1]$. In Fig. 22(e), K is shown as a function of the mirror spacing L. The curve sharply peaks around $L = 120$ nm marking the favorable L-regime for StE [85]. The L-dependency of K can be understood from the rate equation for the mean number of photons ρ in the forward mode: $\dot{\rho} = \beta \Gamma_{SpE} N (1 + \rho) - \gamma \rho$ [73]. While the number N of excited molecules as well as the damping rate γ for photons from the passive cavity is rather constant under variation of L, we found that the product $\beta \Gamma_{SpE}$ calculated for PI-molecules centered in the microresonator and oriented parallel to the mirrors strongly depends on the mirror spacing as shown in Fig. 22(f). Evidently, the product $\beta \Gamma_{SpE}$ shows a sharp maximum for mirror spacings around 120 nm and it reflects the measured L-dependency of K (see Fig. 22(e)). In other words, $\beta \Gamma_{SpE}$ as function of L determines the photon density in the forward mode and hence the StE-efficiency.

In chapter 6, we will identify unstable emitting spatial modes formed between the resonator mirrors as the origin of the output fluctuations discussed above.

5.7   Summary and Conclusion

To summarize the reported results, we found that the maximum output efficiency at $L = 120$ nm (see Fig. 21(b), (d)) coincides with the maximum of the following system parameters, i. e. (I) the calculated coupling ratio β (see Fig. 22(a)), (II) the experimental coupling ratio β' indicating the maximum spectral and angular narrowing of outcoupled emission (see Fig. 22(b)) and (III) the measured K and the calculated $\beta \Gamma_{SpE}$, respectively, reflecting favorable StE-conditions (see Fig. 22(e), (f)). In contrast, maximum enhancement of Γ_{SpE} is predicted and observed for $L = 150$ nm while for $L = 120$ nm no rate modification compared to the free-space value $\Gamma_{SpE,0}$ occurs (see Fig. 21(a)).

In conclusion, we emphasize that the difference Δ is a fundamental phenomenon which occurs when the resonator dimensions approach one half emission wavelength of enclosed emitters. Even for monochromatic emitters, Δ remains large (around 10 nm in our system) and can only be further decreased by increasing the mirror reflectivities. The mirror spacing for maximum output and StE-efficiency depends critically on the shape of the free-space emission spectrum of embedded QME and needs to be determined carefully. The presented results must be accounted for the design of photonic applications based on planar microresonator structures.

6 Spatial Modes of a $\lambda/2$-Microresonator

In this chapter, we investigate the radiation patterns formed on the surface of a planar $\lambda/2$-microresonator enclosing immobilized dye molecules. Using time-resolved widefield imaging microscopy, we observed isolated spatial modes which occurred randomly in the pumped microresonator area, exhibiting strong intensity fluctuations. The measured upper limit for the diameter of isolated spatial modes around 0.5 μm was found to agree with theoretical predictions for the effective mode radius of our system. Moreover, we demonstrate the formation and the decay of a spatial double mode.

6.1 Introduction

Planar microresonators form spatially confined circular modes with a finite lateral extent, i. e. a mode radius, which is determined by the optical properties of the microresonator [37,64,65,86]. The formation of laterally restricted spatial modes is a direct consequence of the finite loss of the microresonator: Since emitted photons escape from the resonator after a certain number of internal reflections that is determined by the optical properties of the microresonator, a transverse mode cannot extent infinitely along the mirror surfaces and, as a consequence, the mode divergence angle is finite. As a result, the radius of a spatial mode is also limited since both the angular divergence and the radius of a spatial mode are connected by the diffraction relation. If the pumped area of the microresonator is larger than the transverse diameter of a spatial mode, the active spatial modes are supposed to fill the pumped area or, in other words, to form a spatial multi mode.

Direct observation of spatial modes in a planar microresonator doped with dye solution has been reported for operation below and above laser threshold and the measured spatial mode diameter was found to be in agreement with theoretical predictions [89]. The measured radiation pattern consisted of spatially isolated circular spots occurring in the pumped area of the microresonator and were reported to have a stable position.

From this, it is intuitively clear that the strong intensity fluctuations observed in the output of planar microresonators (see [85, 86] and chapter 5) should originate from unstable spatial modes formed in the pumped area of the microresonator.

To our present knowledge, direct observation, i. e. imaging, of unstable spatial modes formed in a planar $\lambda/2$-microresonator has not been reported so far in the literature. Moreover, experimental proof for the formation of a double mode from two isolated spatial modes seems to be lacking.

In the following, we establish a relation between the output properties of the $\lambda/2$-microresonator as discussed in chapter 5 and the microresonator-controlled emission pattern formed in the plane of the resonator mirrors. As a key result, we can assign the measured output fluctuations as shown in Fig. 22(c) to unstable emitting spatial modes occurring randomly in the pumped area of the microresonator.

6.2 Experimental

The microresonator samples consisted of two resonator mirrors $M_{1,2}$ with a silver film thickness of 30 nm and 60 nm, respectively, resulting in a cavity-Q around 50 in the $\lambda/2$-regime (see chapter 2). As an active medium between $M_{1,2}$, a transparent polymer ($n_{pol} = 1.56$) doped with uniformly distributed and randomly oriented perylene-type molecules (abbreviated PI, see Fig. 7) in high concentrations ($c_{PI} \simeq 10^{-5}$ mol/l) was used.

Widefield imaging was performed at room temperature with the experimental setup sketched in Fig. 1 and described in chapter 1.3. Series of images were acquired at 7.6 Hz (see Fig. 25(a)-(f), exposure time $\Delta t_{int} = 40$ milliseconds per frame as well as Fig. 23(a) and Fig. 24(a)-(c), both with $\Delta t_{int} = 10$ milliseconds per frame) and at 9.9 Hz (see Fig. 23(b), $\Delta t_{int} = 1$ millisecond per frame), respectively. The cw-pump power was in the order of $P_{pump} \sim 1$ kW/cm^2.

6.3 Radiation Patterns for Representative Mirror Spacings

Measurements of the spatial intensity distribution were carried out in the $\lambda/2$-regime of the microresonator (see chapter 2). In Fig. 23(a) and (b), high resolution widefield images of the microresonator surface are shown for two different mirror spacings L. The images were taken by laser-pumping a microresonator area having a diameter of around 3 µm and measuring the radiation patterns displaying the spatial intensity distribution of outcoupled microresonator-controlled emission on mirror M_1. The intensity distribution measured for $L \simeq 120$ nm is shown in Fig. 23(a) and consists of spatially isolated bright spots occurring in the pumped area as can be seen in the corresponding cross section shown in Fig. 23(c). The width of a gaussian envelope of the bright features ($FWHM \simeq 2.8$ µm) displays the width of the pumped area of the microresonator and was found to increase with increasing pump power.

In contrast, the radiation pattern measured for $L \simeq 150$ nm as shown in Fig. 23 (b) does not exhibit spatial fine structure. The smooth envelope of the measured intensity distribution, however, reveals a similar width compared to that for $L \simeq 120$ nm as can be seen from the cross section shown in Fig. 23 (d) yielding a $FWHM$-value around 2.5 µm.
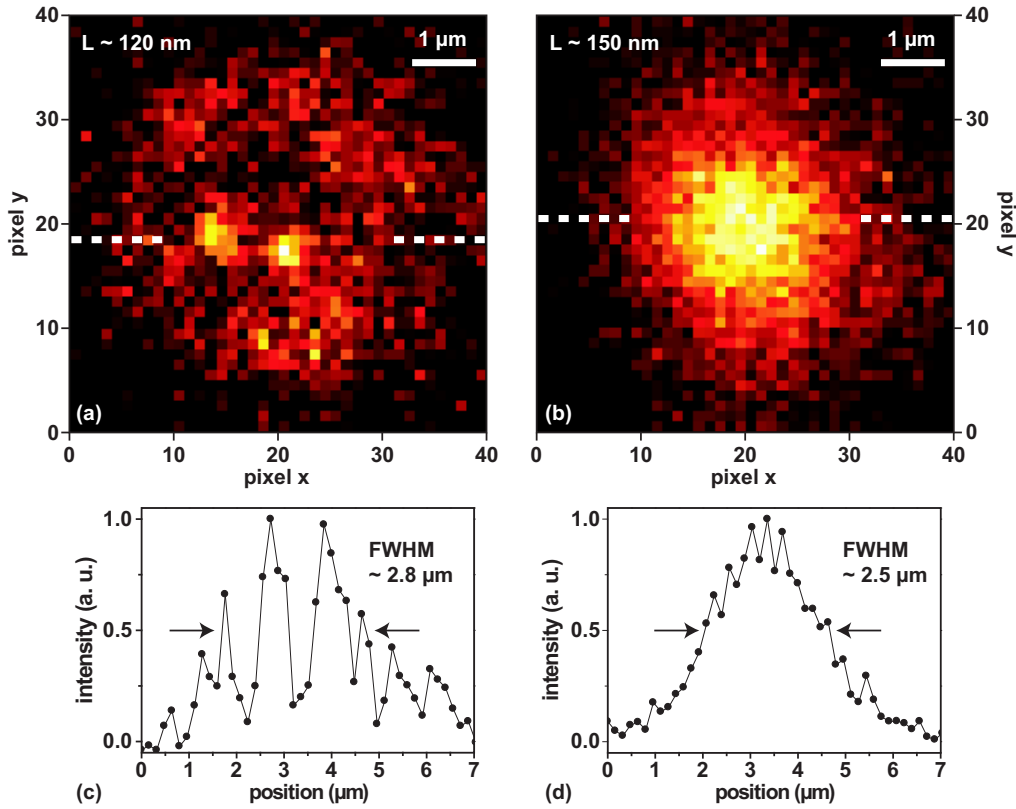
Figure 23: Microresonator-controlled emission patterns in the mirror plane for two representative mirror spacings (a) $L \simeq 120$ nm and (b) $L \simeq 150$ nm, respectively. (c) For $L \simeq 120$ nm, the cross section along the dashed line in (a) exhibits a fine structure consisting of isolated circular spots (see also Fig. 24) as discussed in the text. (d) For $L = 150$ nm, the cross section along the dashed line in (b) exhibits no fine structure. The $FWHM$-values in (c) and (d) refer to a Gaussian envelope function and reflect the diameter of the pumped microresonator area which was found to depend on the excitation power.

6.4 Shape and Intensity Fluctuations of Isolated Spatial Modes

In the following, we will investigate the radiation pattern formed by the microresonator for L around 120 nm in more detail.

We found that the bright spots shown in Fig. 23(a) are not stable in time. The bright spots occur randomly in the pumped area and exhibit strong intensity fluctuations, i. e. "on"- and "off"-states, on timescales of milliseconds up to seconds.

We observed an isolated bright spot over a time span of $\Delta t_{meas} = 2.5$ s. Three representative images are shown in Fig. 24(a)-(c). The intensity scale for the three images is kept constant and refers to the intensity maximum occurring in Fig. 24(b).

At t_1, the spatial intensity distribution as shown in Fig. 24(a) does not exhibit any significant feature. The weakly structured background (see also Fig. 25(a)-(f)) reflects the intensity distribution of the laser excitation field in the pumped microresonator area: The fluorescence background intensity in the very center of the radiation patterns, which corresponds to the position of the focal spot and hence the intensity maximum of the focussed laser pump beam, was found to decrease with time and pump power due to irreversible photobleaching of dye molecules. As a result, we found that the center of the pumped area is surrounded by a fluorescent corona showing stable fluorescence background intensity as can be seen by comparing e. g. Fig. 24(a) and (c).

At t_2, we observe a bright fluorescent spot in the center of the pumped microresonator area (see Fig. 24(b)). Finally, at t_3, the bright spot disappeared again as can be seen in Fig. 24(c).

The maximum intensity occurring at the position of the bright spot in Fig. 24(b) is shown as a function of time in Fig. 24(d). During the time interval $\Delta t_{"on"} = 1.44$ s framed by t_1 and t_3, the intensity of the bright spot was found to increase until it dropped suddenly.

The bright spot shown in Fig. 24(b) was found to have a circular shape and a $FWHM$-diameter of around 0.5 µm as derived from the cross sections along the dashed lines. The cross sections in x-direction (dots) and y-direction (circles), respectively, are depicted in Fig. 24(e) and can be considered as the point spread function of our imaging setup. The cross section along the dashed line in Fig. 24(c) is also shown as squares in Fig. 24(e) to demonstrate the high contrast that results in a clear visibility of "on"- and "off"-states. Additionally, the cross section of the radiation pattern measured at $L \simeq 150$ nm and presented in Fig. 23(d) is shown as grey background for comparison.

According to [89], we identify the bright spots observed for mirror spacings L around 120 nm as fundamental spatial modes formed by the microresonator and compare the measured upper limit of the spatial mode diameter with theoretical predictions.

Two theoretical concepts for a resonator-mediated coupling length or, in other words, a transverse mode confinement in planar microresonators have been reported in the literature: The transverse quantum correlation length
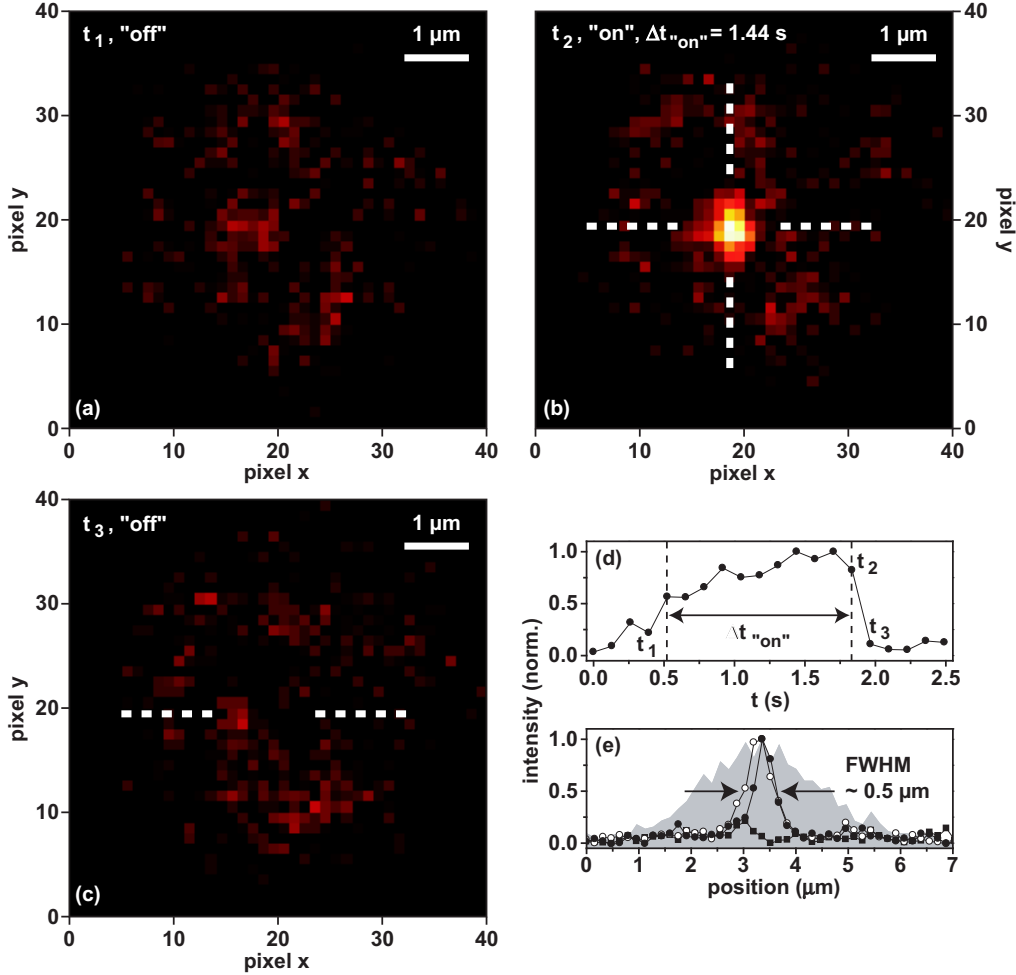
Figure 24: (a)-(c) Isolated bright spot formed in the pumped area of the microresonator at $L \simeq 120$ nm showing "on"-states (b) and "off"-states (a, c). (d) Time trace of the intensity at the position of the bright spot shown in (b) normalized to the intensity maximum occurring at $t = 1.44$ s. (e) The cross sections along the dashed lines in (b) reveal a circular spot shape having a $FWHM$-diameter of 0.5 μm in both x-direction (dots) and y-direction (circles) which can be considered as the resolution limit of our setup. The corresponding cross section taken during an "off"-state along the dashed line in (c) is also shown (squares). The grey background in (e) shows the cross section at $L \simeq 150$ nm (taken from Fig. 23(d)) for comparison.

l_m [37, 63] and the effective spatial mode radius r_{eff} [64, 65, 86]. The transverse quantum correlation length l_m is derived by accounting for Heisenberg's uncertainty principle for position and momentum of an emitted photon in the presence of a planar microresonator and can be understood as the transverse length scale of photon delocalization. In consequence, if more than one emitting molecule is located within l_m, the Spontaneous Emission process merges into a Stimulated Emission process at exceedingly low excitation power [66]. In chapter 3, l_m has already been introduced (see Eqn. 6) and estimated for the $\lambda/2$-regime of our microresonator.

The effective spatial mode radius r_{eff} is derived by accounting for the modified photonic mode density in the presence of a planar microresonator [64, 65]. r_{eff} can be interpreted as the mean free path of photons measured along the mirror surfaces when the photons emitted in the microresonator undergo multiple internal reflections with an angle to the normal axis of the mirrors that is determined by the optical properties of the resonator. Neglecting background absorption of the polymer film at the pump laser wavelength, the spatial mode radius can be written as

$$r_{eff} = \sqrt{\frac{\pi\lambda(x,y)L(x,y)(R_1 R_2)^{1/4}}{8 n_{pol}(1 - \sqrt{R_1 R_2})}} \tag{8}$$

Here, $\lambda(x,y)$ is the wavelength at the on-axis transmission maximum of the microresonator (see also chapter 2), n_{pol} is the refractive index of the polymer film with thickness $L(x,y)$ between the resonator mirrors $M_{1,2}$ having the reflectivities $R_{1,2}$. For the present microresonator with silver mirror thickness $d_1 = 30$ nm and $d_2 = 60$ nm, we use $R_1 = 0.71$ and $R_2 = 0.91$ and calculate r_{eff} assuming $\lambda(x,y) = 532$ nm and $L(x,y) = 120$ nm. As a result, we get $r_{eff} \simeq 0.27$ μm.

In contrast, the calculated transverse quantum correlation length $l_1 \simeq 2.58$ μm as estimated in chapter 3.6 for the same microresonator configuration is at least a factor of five larger than the measured upper limit of the diameter of spatial modes as determined from our experimental data (around 0.5 μm, see Fig. 24(b), (e)).

As a result, the calculated r_{eff}-value resulting in an effective spatial mode diameter of roughly 0.5 μm is in good agreement with our experimental observations.

We now discuss the influence of the mirror spacing L on the observability of spatial modes and the origin of the intensity fluctuations.

The L-dependency of the visibility of spatial modes as shown in Fig. 23

can be understood from the L-dependency of the radiation coupling ratio to the local forward mode, β, as discussed in chapter 5: As shown in Fig. 22(a), $\beta(L)$ reaches its maximum value β_{max} for L around 120 nm. For $L \simeq 150$nm, $\beta(L)$ is only $0.05 \cdot \beta_{max}$ because most of the molecular fluorescence emission is coupled to off-axis resonances. As a result, the emission pattern of adjacent spatial modes mutually overlap and smear out due off-axis emission undergoing multiple internal reflections between the resonator mirrors.

The output properties of spatial modes, i. e. the distribution of "on"- and "off"-states as well as the ratio between maximum and minimum output intensities, are determined by the product $\beta\Gamma_{SpE}$ as a function of L as shown in Fig. 22(f) and discussed in chapter 5. Since $\beta\Gamma_{SpE}$ as a function of L is the measure for the Stimulated Emission efficiency of the system, we identify the strong output fluctuations of spatial modes as unstable laser oscillations. The process can be explained as follows: If a sufficient number of molecules immobilized within the geometrical boundaries of a spatial mode is prepared in an excited electronic state, the laser oscillation starts. Under continuous wave illumination, a fraction of these molecules undergoes an intersystem crossing to a long-lived dark molecular triplet state. If the number of molecules in the dark triplet state reaches a critical value, the oscillation brakes down (see Fig. 24(d)). This interpretation is supported by the fact that observation of isolated spatial modes and strong output fluctuations was only possible for L around 120 nm where $\beta\Gamma_{SpE}$ and hence the Stimulated Emission efficiency reaches its maximum value (see Fig. 22(f)).

From the molecular dopant concentration of our polymer film, $c_{PI} \simeq 10^{-5}$ mol/l, we can derive an upper limit for the number of molecules N_{ism} contributing to the radiation pattern formed by an isolated spatial mode. Assuming a cylinder having a diameter of $2 \cdot r_{eff} \simeq 0.5$ µm and a height of $L = 120$ nm which is the actual polymer film thickness, we derive that on average $N_{ism} \simeq 140$ molecules are located within the geometrical boundaries of a spatial mode. Hence, we conclude that the spatial mode pattern as discussed here as well as the output fluctuations as described in chapter 5 were produced by at most a few tens of molecules coupled simultaneously by the microresonator.

6.5   Formation and Decay of a Spatial Double Mode

We now discuss the formation and the decay of a spatial double mode or, in other words, the transition between single mode and double mode operation, in the pumped area of the microresonator.

In Fig. 25, a series of widefield images and three representative cross sec-
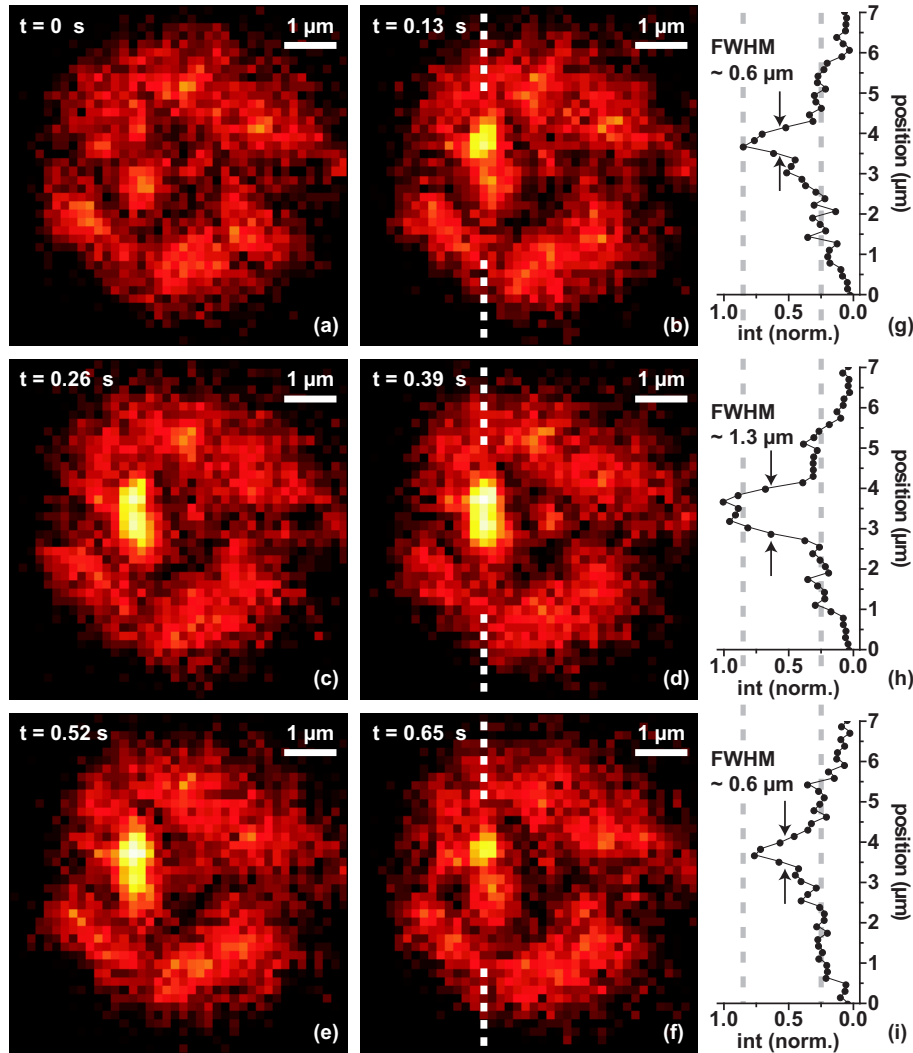
Figure 25: (a)-(f) Stepwise formation and decay of a spatial double mode consisting of two adjacent spatial modes observed at $L \simeq 120$ nm. (h) The cross section along the dashed line in (d) reveals that the spatial double mode has a $FWHM$-diameter of twice the value found for an isolated spatial mode as can be seen from the cross sections shown in (g) and (i) taken along the dashed lines in (b) and (f), respectively. The intensity scale of both the images (a)-(f) and the cross sections (g)-(i) is kept constant and refers to the intensity maximum occurring in (d) which was set to 1 in (g)-(i). The dashed lines in the cross sections (g)-(i) refer to the maximum intensity in cross section (g) and the fluorescence background indicating the size of the pumped microresonator area, respectively.

59

tions of the intensity distribution of the microresonator-controlled radiation pattern for $L \simeq 120$ nm are shown. The intensity scale for both images and cross sections is kept constant and refers to the intensity maximum observed in Fig. 25(d). For $t = 0$ s, no significant bright feature can be observed (see Fig. 25(a)). For $t = 0.13$ s (see Fig. 25(b)), we observe a spatial mode having a $FWHM$-diameter of around 0.6 μm as derived from the cross section taken along the dashed line and shown in Fig. 25(g). From $t = 0.26$ s to $t = 0.39$ s (see Fig. 25(c), (d)), the diameter of the bright spot expands in y-direction due to the appearance of a second spatial mode while it is rather constant in x-direction. The cross section taken along the dashed line in Fig. 25(d) reveals a $FWHM$-diameter of around 1.3 μm which is twice the value found for the isolated spatial mode shown in Fig. 25(b). From $t = 0.52$ s to $t = 0.65$ s (see Fig. 25(e), (f)), the double mode decays until only a single isolated spatial mode remains as can be seen from the cross section along the dashed line in Fig. 25(f) which is shown in Fig. 25(i).

We now discuss the temporal evolution of the emitted intensity. The measured intensity stepwise increases upon formation of the double mode as can be seen in Fig. 25(a)-(d) and the corresponding cross sections (see Fig. 25(g), (h)). Finally, as shown in Fig. 25(f), (i), the intensity of the remaining isolated spatial mode drops below the value observed for the same spatial mode before the double mode was formed (see Fig. 25(b), (g)) as clarified by the dashed line in Fig. 25(g)-(i). The second dashed line highlights the rather constant fluorescence background indicating the size of the pumped microresonator area. Additionally, it served as a reference for the estimation of the $FWHM$-values of the spatial mode diameter as indicated in Fig. 25(g)-(i).

It should be mentioned that spatial modes formed by a planar microresonator well below lasing threshold are expected to radiate incoherently [65]. Indeed, we did not observe any intensity correlation for clearly isolated spatial modes. The observation, however, of an intensity maximum at the time when two spatial modes unify (see Fig. 25(d), (h)) could indicate that a spatial double mode radiates more efficiently than two isolated spatial modes.

6.6   Summary and Conclusion

In summary, we observed radiation patterns on the surface of a planar $\lambda/2$-microresonator enclosing immobilized broadband-emitting dye molecules. For mirror spacings offering a high radiation coupling efficiency to the forward mode, we could observe isolated spatial modes. The measured $FWHM$-diameter of 0.5 μm for an isolated spatial mode agrees with theoretical predictions for the effective mode radius [89] of the present microresonator and displays the point spread function of our experimental setup. In contrast, it

is significantly smaller than the transverse quantum correlation length [37] calculated for our system.

Unstable emitting spatial modes were identified to be the origin of the output fluctuations discussed in chapter 5.

We demonstrated the formation and the decay of a spatial double mode in the pumped area of the microresonator as a proof for the validity of the spatial mode concept in planar microresonators.

The presented results complement the fundamental understanding of optical processes in planar microresonators and are encouraging for the experimental realization of single molecule dipole imaging in $\lambda/2$-microresonators under ambient conditions.

7 Vibronic Coupling of Single Molecules to Photonic Modes of a $\lambda/2$-Microresonator

In this chapter, we study spatially isolated molecules and nanostructures, respectively, immobilized in an optical $\lambda/2$-microresonator by means of fluorescence and Raman microscopy. In a first step, we show that single terrylene molecules relax into microresonator-allowed vibronic levels of the electronic ground state by emission of single fluorescence photons. Low temperature fluorescence spectra demonstrate that the microresonator spectrally isolates the purely electronic transition of single terrylene molecules accompanied by suppression of radiative relaxation in excited vibronic levels of the electronic ground state. In a second step, we demonstrate microresonator-controlled Raman scattering on embedded single-walled carbon nanotubes and discuss if utilization of a $\lambda/2$-microresonator enables cooling them.

7.1 Introduction

Molecules have, in comparison with atoms, additional degrees of freedom. While rotational motion of molecules can be suppressed by embedding them in condensed or solid host environments, the control of molecular vibrational motion remains one of the major goals in nano-science. Microresonators are promising tools to control the vibrational motion of single molecules by coupling them to the photonic mode structure of the resonator [5]. By using a planar $\lambda/2$-microresonator the radiative transition rates in both fluorescence and Raman scattering processes can be modified due to enhancement and inhibition of the Spontaneous Emission (SpE) rate Γ_{SpE} [42, 44] or, in analogy, the Raman scattering cross section σ [90, 91]. While the significance of a strong coupling between emitter and resonator has been emphasized in the context of quantum information processing [1], somewhat less attention has been paid to low-Q microresonators that operate in the weak coupling regime but still can modulate radiative rates of embedded molecules by at least one order of magnitude (see chapter 5). Experimental evidence, however, for coupling vibronic modes of single molecules and spatially isolated nanostructures, respectively, to photonic modes of a $\lambda/2$-microresonator seems to be lacking.

7.2 Experimental

For **fluorescence measurements at low temperature**, a transparent polymer ($n_{pol} = 1.56$) doped with uniformly distributed and randomly oriented terrylene molecules (for structural formula see Fig. 26(a)) in low concentrations ($c_{terrylene} \simeq 10^{-7}$ mol/l to 10^{-8} mol/l) was used as an active medium between the mirrors of the microresonator samples (see chapter 2). The resonator mirrors $M_{1,2}$ with a silver film thickness of 30 nm and 60 nm, respectively, were found to result in a cavity-Q around 50 in the $\lambda/2$-regime.

Fluorescence measurements on single terrylene molecules embedded in the microresonator were performed at cryogenic temperatures with the low temperature setup described in chapter 1.3 and sketched in Fig. 2. For recording intensity correlation curves, the setup was equipped with an Hanbury-Brown and Twiss interferometer as discussed in chapter 1.3 and shown in Fig. 3(a).

For **Raman scattering experiments at room temperature**, we prepared microresonator samples with resonator mirrors $M_{1,2}$ having a silver film thickness of 30 nm and 60 nm, respectively, and enclosing a PMMA solution doped with different species of single-walled carbon nanotubes (SWNT). An
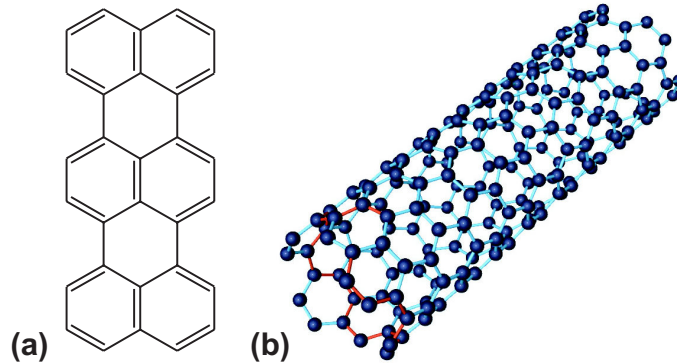
Figure 26: (a) Structural formula of a terrylene molecule. (b) Part of a three-dimensional model structure of a chiral single-walled carbon nanotube (SWNT) taken from http://www.surf.nuqe.nagoya-u.ac.jp.

example of a chiral SWNT-structure is shown in Fig. 26(b). After evaporation of the solvent (dichloroethane), the PMMA has a refractive index of n_{pol} = 1.49.

Raman scattering experiments on SWNT embedded in the microresonator were performed with the room temperature setup (see Fig. 1) as discussed in chapter 1.3.

7.3 Vibronic Coupling and Single Molecule Fluorescence

We cooled a microresonator doped with terrylene molecules in a liquid helium bath to 1.8 K. Under this condition, the electron-phonon-coupling between molecules and polymer matrix is considerably suppressed [9]. Hence, we expect that the fluorescence spectra exhibit their vibronic fine structure, i. e. narrow fluorescence lines at vibronic frequencies characteristic for terrylene molecules [92]. In Fig. 27, diffraction-limited confocal microscopy images show the integrated fluorescence emission of single terrylene molecules spatially isolated and immobilized in the $\lambda/2$-microresonator. As shown in Fig. 27(a), we observed single molecules exhibiting intensity blinking on timescales of milliseconds up to seconds. We also found molecules (see Fig. 27(b)) delivering stable fluorescence emission on these timescales. The corresponding intensity correlation function $g^{(2)}(\tau)$ detected for a single terrylene molecule imaged in Fig. 27(b) is shown in the inset. We found clear evidence for photon-antibunching ($g^{(2)}(0) < 1$) proving the presence of
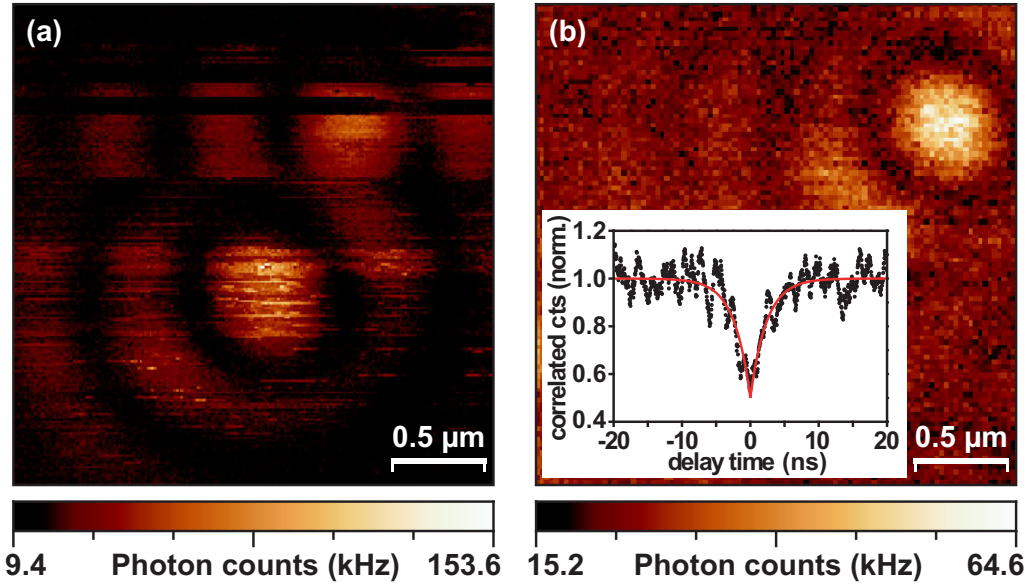
Figure 27: Diffraction-limited confocal fluorescence microscopy images of single terrylene molecules on resonance with a $\lambda/2$-microresonator at $T = 1.8\ K$. (a) Two spatially isolated molecules exhibit strong intensity blinking. (b) Single molecule delivering stable fluorescence emission. (Inset) The corresponding intensity correlation measurement (dots) exhibits photon-antibunching. Fitting the model function $1 - a \cdot \exp\left(-\left|\tau\right|/\tau_{meas}\right)$ to the data (line) reveals an excited state lifetime $\tau_{meas} = 2.3$ ns.

a single emitter and emission of single fluorescence photons [88].

The corresponding molecular excitation-emission cycle for this measurement is depicted in Fig. 28(a): We used the vibronic excitation scheme [93] to prepare single molecules into excited vibronic levels of the first excited electronic state, i. e. $S_{1,1}$. The $S_{1,0}$ level is reached by fast non-radiative internal conversion (IC) of vibrational energy on a time scale of picoseconds accompanied by a loss of coherence between the excitation field and the molecular transition dipole. Importantly, the efficiency of a radiative transition to a vibronic level of the molecular electronic ground state S_0 is determined by the local mirror spacing $L(x, y)$ according to Eqn. 1 as indicated by the on-axis transmission spectrum of the microresonator in Fig. 28(a). In the present case, it is tuned on-resonance with the purely electronic transition $S_{1,0} \rightarrow S_{0,0}$ that becomes manifest in the strongest and narrowest fluorescence line limiting the measured single molecule spectra on the blue side, i. e. the zero-phonon line (ZPL) [9].

65
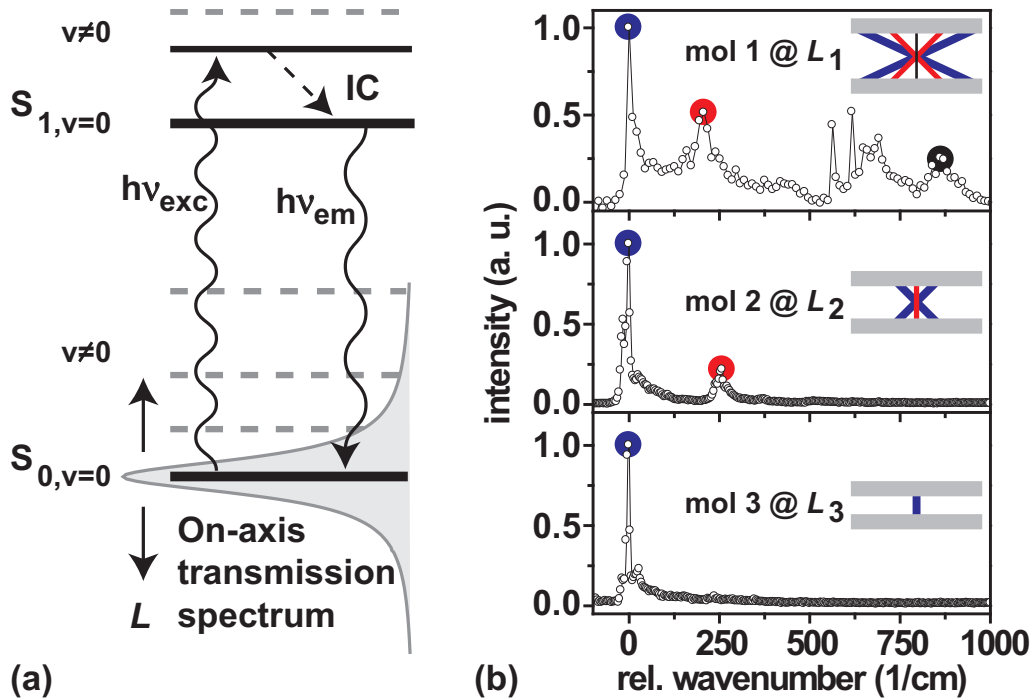
Figure 28: (a) Energy level diagram of the excitation-emission cycle of a fluorescent molecule embedded in the microresonator as discussed in the text. An intersystem crossing to a dark molecular triplet state is neglected. (b) Microresonator-controlled fluorescence spectra (circles) of single terrylene molecules for three mirror spacings $L_1 > L_2 > L_3$. The coupling of electronic-vibronic transitions to on- and off-axis cavity resonances is determined by the transmission condition of the microresonator (Eqn. 1) and clarified by the corresponding schematics for three representative transitions (blue: $\tilde{\nu} = 0$ cm^{-1} [ZPL], red: $\tilde{\nu} = 240$ cm^{-1} and black: $\tilde{\nu} = 850$ cm^{-1}) as discussed in the text.

Microresonator-Controlled Excitation of Molecular Vibrations

The influence of the mirror spacing on single molecule fluorescence spectra of terrylene is shown in Fig. 28(b) for three different molecules. Three representative transitions are marked by colored dots:

(I) The ZPL (blue dots) was set as the origin of the wavenumber scale. The relaxation into the molecular electronic ground state accompanied by excitation of a molecular vibration $S_{1,0} \rightarrow S_{0,1}$ is marked by (II) red dots for

the long-axis stretch vibration of the whole molecule around $\tilde{\nu} = 240$ cm^{-1} and (III) a black dot for the ring breathing vibration at $\tilde{\nu} = 850$ cm^{-1}.

The oscillatory strengths of the respective radiative transitions in free space are given by the overlap between the vibronic wave functions of electronic excited and ground state and are indicated in the schematic diagrams in Fig. 28(b) by thickness of colored lines. For molecule 1 (upper spectrum), the weak vibronic transition at $\tilde{\nu} = 850$ cm^{-1} (black dot) is coupled to the forward mode of the microresonator, i. e. the on-axis resonance (black line in the sketch) determined by the local mirror spacing L_1. Additionally, the emitter couples to blue-shifted off-axis resonances: Since L_1 is fixed, the blue-shifted transitions compensate a decreased λ by an increased ϑ (see Eqn. 1). By reducing L, we observed that vibronic lines in the measured spectra of detected molecules were cut successively from the red side of the spectrum: For molecule 2 at L_2 (middle spectrum), only the long-axis stretch vibration around $\tilde{\nu} = 240$ cm^{-1} is visible in the spectrum. The purely electronic transition is still coupled to an off-axis resonance of the microresonator as indicated in the corresponding schematic. Further reducing the mirror spacing to L_3 allows addressing molecule 3 (lower spectrum). Here, the strong ZPL is on resonance with the forward mode of the microresonator and remains as the only significant feature in the measured spectrum. The spectral width of the ZPL was found to display the instrument response function of our spectrometer having a width of $FWHM_{irf} \simeq 0.4$ nm for a grating with 600 grooves per mm. Note, that the spectral width of the ZPL and can reach lifetime-limited values, depending on the host matrix [9]. In chapter 8, we will investigate the temporal coherence properties of the microresonator-controlled single molecule fluorescence emission as shown in the lower spectrum of Fig. 28(b) by means of interferometric spectroscopy.

We show now that the spectral isolation of the purely electronic transition is accompanied by the suppression of radiative relaxation into excited vibronic levels of the electronic ground state. In the upper panel of Fig. 29, the relative rates $\Gamma_{SpE}/\Gamma_{SpE,0}$ calculated for the transition frequencies marked in Fig. 28(b) are shown assuming the molecular transition dipole to be located in the center of the microresonator and oriented parallel to the mirrors. The theoretical approach is discussed in more detail in chapter 3. Since the ZPL positions of terrylene molecules were found to be spectrally dispersed due to strong inhomogeneous broadening [9], we assume the ZPL to be spectrally located at $\lambda_{max} = 600$ nm, a typical value observed in our experiments. For L around 153 nm corresponding to L_1 as shown in Fig. 28(b), the rate Γ_{SpE} is enhanced for all three transitions with respect to the free-space val-
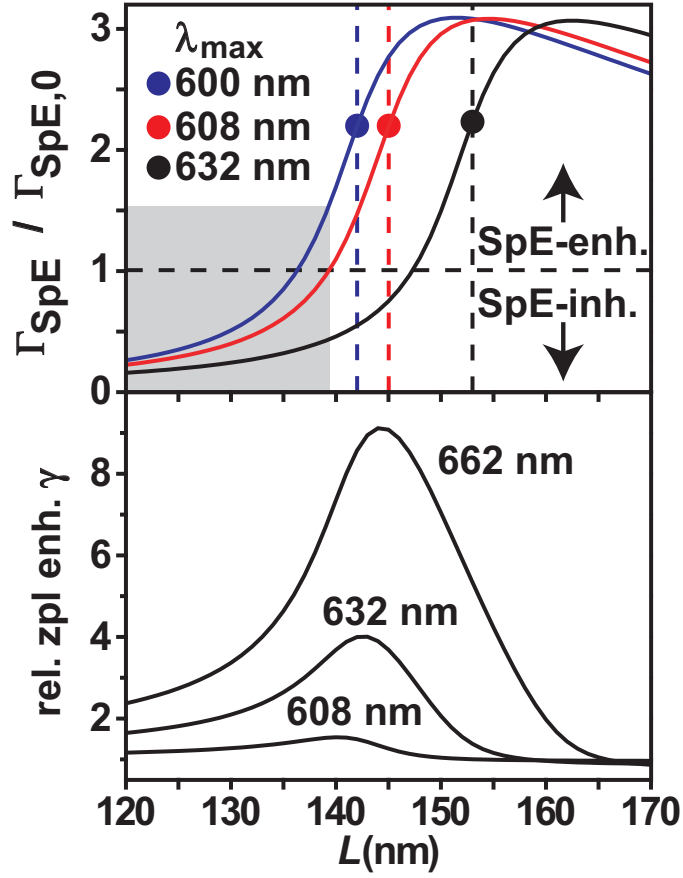
Figure 29: (Upper panel) Calculated relative SpE-rates for the transitions marked in Fig. 28(b) by colored dots assuming the ZPL spectrally located at $\lambda_{max} = 600$ nm (blue curve). The red curve for $\lambda_{max} = 608$ nm corresponds to the molecular transition occurring at $\tilde{\nu} = 240$ cm^{-1} and the black curve for $\lambda_{max} = 632$ nm corresponds to the molecular transition occurring at $\tilde{\nu} = 850$ cm^{-1}. (Lower panel) Relative enhancement γ of the ZPL with respect to three representative transitions occurring at $\tilde{\nu} = 240$ cm^{-1} (corresponding to the curve for $\lambda_{max} = 608$ nm), $\tilde{\nu} = 850$ cm^{-1} ($\lambda_{max} = 632$ nm) and $\tilde{\nu} = 1560$ cm^{-1} ($\lambda_{max} = 662$ nm) as discussed in the text.

ues $\Gamma_{SpE,0}$, i. e. the corresponding SpE-rates in a comparable sample without silver mirrors. By varying L, the radiative rates can be tuned: For L around 145 nm, which corresponds to L_2 in Fig. 28(b), the excitation of the ring breathing vibration (black curve) is already suppressed while excitation of the long-axis stretch vibration (red curve) is still enhanced with respect to free space. Finally, for L below 140 nm (reflected by grey shaded area in the

upper panel of Fig. 29) which corresponds to L_3 in Fig. 28(b), all radiative transitions with exception of the purely electronic transition are suppressed with respect to free space (see also Fig. 28(a)).

In the lower panel of Fig. 29, the enhancement factors γ of the ZPL with respect to the vibronic transitions at $\tilde{\nu} = 240 \ cm^{-1}$ (corresponding to the curve for $\lambda_{max} = 608$ nm in the upper panel of Fig. 29), $\tilde{\nu} = 850 \ cm^{-1}$ ($\lambda_{max} = 632$ nm) and $\tilde{\nu} = 1560 \ cm^{-1}$ ($\lambda_{max} = 662$ nm) are shown. The curves were calculated by dividing the relative rate $\Gamma_{SpE}/\Gamma_{SpE,0}$ of the purely electronic transition by the relative rates of the respective electronic-vibronic transitions as function of L. While the maximum ZPL-enhancement with respect to the low-frequency transition at $\tilde{\nu} = 240 \ cm^{-1}$ is rather small ($\gamma = 1.5$ at $L = 140$ nm), it reaches almost one order of magnitude for the high-frequency transition at $\tilde{\nu} = 1560 \ cm^{-1}$ ($\gamma = 9.1$ at $L = 144$ nm). As a result, a large spectral separation between distinct vibronic transitions supports their selective enhancement and inhibition by means of the microresonator. The difference of around 10 nm between the mirror spacings for maximum output efficiency and the maximum rate Γ_{SpE}, respectively, for a specific transition is a fundamental property of $\lambda/2$-microresonators and is described in detail in chapter 5.

We now put our findings in the context of recent results reported in the literature:

1. As an improvement of the single-molecule based single photon source operating at low temperatures [93, 94], utilization of a $\lambda/2$-microresonator as reported here allows for controlling Γ_{SpE} and the strong and spectrally narrow zero-phonon line emission can be brought on resonance with the forward mode of the microresonator. As a result, the emitted fluorescence photons are strongly directed and can be collected and coupled to optical fibres with increased efficiency. For larger L, angular separation of distinct transitions enables experimental studies of coherence properties of microresonator-controlled on- and off-axis emission [95] and the resulting radiation pattern could be imaged for individual dipole emitters in a $\lambda/2$-microresonator for the first time.

2. The coupling of nearly monochromatic fluorescence emission from a single molecule to a single cavity mode of a microresonator can be considered as an important step towards the realization of a single molecule dye laser [96].

3. The modification of single molecule fluorescence pattern and lifetimes,

respectively, near metal mirrors [97,98] rely predominantly on the non-radiative excited state energy transfer to the metal mirrors. In this case, no significant wavelength-selective enhancement or inhibition of molecular radiative rates can be achieved.

7.4 Vibronic Coupling and Raman Scattering

In the following, we discuss the coupling between vibrational degrees of freedom of molecular nanostructures and photonic modes of the $\lambda/2$-microresonator. As a model system, we have used single-walled carbon nanotubes (SWNT) and have investigated the microresonator-controlled Raman scattering at room temperature. The vibronic modes of SWNT are commonly called phonon modes in the literature and we will follow this convention here.

Microresonator-Controlled Raman Scattering Intensities

In Fig. 30(a), a confocal microscopy image of SWNT homogeneously distributed in a thin film of PMMA is shown. The Raman-spectrum (inset in Fig. 30(a)) measured on bright spots exhibit the well-known phonon modes of SWNT, i. e. the radial breathing mode (RBM), the disorder-induced phonon mode (D) as well as its overtone (G') and the CC stretch vibration (G) [99].

Using the same PMMA-nanotube solution as a medium between the silver mirrors of the $\lambda/2$-microresonator, we found that the scattering intensities for specific phonon modes of SWNT are determined by the mirror spacing. For each pixel of the image shown in Fig. 30(b), a spectrum was taken and the measured scattering intensities for the RBM-mode were subtracted from the measured scattering intensities for the G-mode to obtain the image contrast. As a result, two sectors of spatially separated concentric circles appeared: SWNT become visible, where a characteristic phonon mode (see inset in Fig. 30(a)) is on resonance with the microresonator. The bright inner fringe originates from SWNTs showing strong RBM scattering intensities, the dark outer fringe stems from SWNTs showing strong G band intensities.

This demonstrates that our $\lambda/2$-microresonator can be used as an microspectrometer with single molecule sensitivity (see also chapter 2) having an upper limit for the spectral resolution determined by the spectral width of the local forward mode of the microresonator.

It should be mentioned, however, that the different shapes and sizes of the bright spots in the Raman images (see Fig. 30(a) and (b)) as well as the fact that we did not isolate SWNTs in the sample solution before preparing the microresonator indicates rather observation of nanotube bundles with varying size than observation of spatially isolated individual SWNT.
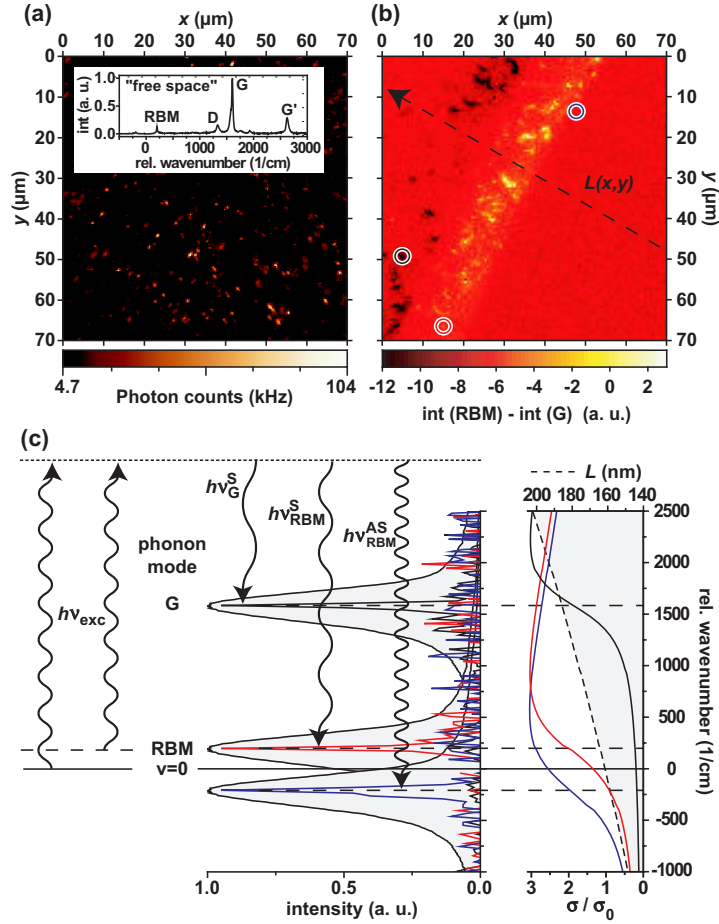
Figure 30: (a) Raman microscopy image of single-walled carbon nanotubes (SWNT) dispersed in a thin film of PMMA. (Inset) Raman spectrum of SWNT taken from one of the bright spots in (a). (b) Raman microscopy image of the same sample as shown in (a) but enclosed between the mirrors of a $\lambda/2$-microresonator. Strong scattering intensities show up where the frequencies of the G-mode (dark outer ring) and the RBM-mode (bright inner ring) are on resonance with the structure. The direction of increasing mirror spacing $L(x,y)$ is indicated by the black arrow. The colored circles mark the positions where the spectra shown in (c) were acquired. (c) Energy level diagram of Raman transitions selected by the microresonator. A typical measured on-axis transmission spectrum of the microresonator (grey curve) is overlapped with the respective Raman bands to improve clarity. Each of the spectra measured for SWNTs located at different mirror spacings L (blue line: RBM anti-Stokes, red line: RBM, black line: G) consists of an isolated Raman band. Note, that the spectra shown in (c) were acquired with a low-resolution grating having 300 grooves per mm.

71

In Fig. 30(c), the corresponding energy level diagram is shown. It consists of three representative spectra taken from the positions marked by circles in Fig. 30(b). As determined by the local mirror spacing $L(x, y)$, each Raman spectrum of SWNT consists of a single Raman band (blue: RBM anti-Stokes, red: RBM , black: G) which is on resonance with the forward mode of the microresonator as indicated by the on-axis transmission spectrum (grey curve) shown in Fig. 30(c). The maximum of the on-axis transmission spectrum was overlapped with the maxima of the respective Raman bands to improve clarity.

Microresonator-Controlled Raman Scattering Rates

We now discuss the L-dependence of the relative Raman scattering cross section σ/σ_0 for the three phonon modes as shown in Fig. 30(c). For large L around 185 nm, the scattering rates for all three phonon modes (blue line: RBM anti-Stokes, red line: RBM and black line: G) are enhanced as compared to the respective cross sections in free space σ_0, i. e. the scattering cross section in a comparable sample without silver mirrors. Here, the excellent spectral isolation of the G-band (black spectrum) results from the high scattering cross section for the G mode in free space (see inset Fig. 30(a)) and a suppressed detection efficiency for the RBM bands which are coupled to off-axis resonances of the microresonator in analogy to the situation shown in the upper panel of Fig. 28(b).

For L around 165 nm, scattering rates for both RBM Stokes and anti-Stokes modes are still enhanced while the relative scattering cross section for the G-mode is already suppressed with respect to free space. The spectral selectivity for the RBM-mode (red spectrum) results from both suppressed G-band scattering and reduced off-axis detection efficiency for the RBM anti-Stokes signal which was also observable for some SWNT.

For L below 160 nm, we found SWNT having enhanced scattering rates for the RBM anti-Stokes mode while the corresponding Stokes signal is already slightly suppressed with respect to free space.

It should be mentioned that we also found indications for weak Raman scattering at D and G' frequency, respectively. However, due to the poor Raman scattering intensity of the D-band in free space (see inset in Fig. 30(a)) and the off-resonant pump in the case of the G'-cavity-resonance, the scattering signal is weak compared to RBM and G, as expected.

Cooling of SWNT in a Planar $\lambda/2$-Microresonator

We now discuss the potential of the $\lambda/2$-microresonator for optical cooling of SWNT, i. e. removing vibrational energy from a SWNT that is initially in thermal equilibrium with its local environment.

Due to the large number of atoms, SWNT offer various degrees of freedom and hence, unlike atoms, efficient internal relaxation pathes that compete with the radiative relaxation. These internal relaxation channels cannot be controlled by the microresonator. In particular, the extremely low photoluminescence quantum yield of SWNT further deteriorates the energy balance: Almost every photon absorbed by SWNT will be converted into heat.

On the other hand, cooling of a specific phonon population, for example the RBM, could be favored by the presence of the $\lambda/2$-microresonator: In this scheme, the laser energy would be tuned on resonance with the anti-Stokes transitions, i. e. $E_{ii} - \hbar\omega_{RBM}$, of a specific SWNT [100] that is also on resonance with the local forward mode of the microresonator. Depending on the excitation field density, we expect a dynamical equilibrium between the phonon bath and the RBM population that is reduced by the anti-Stokes Raman transition. Experimentally, this mode-selective cooling phenomena could be demonstrated by measuring a sub-linear power dependence of the RBM anti-Stokes scattering intensity.

Microresonator-Controlled Photoluminescence of SWNT

For larger mirror spacings around $L = 280$ nm, we observed microresonator-controlled bandgap-photoluminescence (PL) from SWNT in absence of any Raman scattered light in the measured spectra. Since use of SWNT as photonic elements is still limited by the poor PL quantum yield, utilizing $\lambda/2$-microresonators can help to improve their PL-efficiency by enhancing the radiative exciton decay rate [18].

7.5 Summary and Conclusion

In summary, we demonstrated that an optical $\lambda/2$-microresonator gives access to vibrational motion of single embedded molecules and nanostructures. The coupling of molecular vibrations to the photonic mode structure of the microresonator is determined by the vibronic spectrum of the molecule and the mirror spacing L.

The coupling of the purely electronic radiative transition of a single molecule to the forward mode of the microresonator can be considered as

an advance for single photon sources based on single molecules and as an important step towards realization of a single molecule dye laser.

Our findings can be transferred directly to design advanced photonic devices as well as ultra sensitive integrated micro-spectrometers. The presented results should have impact on the fields of single molecule spectroscopy, quantum optics, laser physics and nanophotonics.

8 Single Molecule Fourier Spectroscopy

In this chapter, we analyze the correlation between the spectral shape and the temporal coherence of fluorescence emission of single dye molecules embedded in a planar $\lambda/2$-microresonator. Low temperature studies reveal the influence of typical single molecule fluorescence features like intensity blinking and spectral diffusion on the visibility of two-beam interference pattern measured with a Michelson interferometer. By comparison with spectroscopic data that was acquired with a grating spectrometer, we demonstrate the applicability of Fourier transform spectroscopy for unstable emitting molecules. Moreover, we show how the phonon sideband accompanying the narrow molecular zero-phonon emission line affects the visibility of interference fringes.

This chapter is based on:

M. Steiner, R. Korlacki, A. Hartschuh, and A. J. Meixner, "Single Molecule Fourier Spectroscopy," (in preparation).

8.1 Introduction

Single photon sources (SPS) emitting optical wave trains containing only a single photon have recently attracted considerable scientific interest and they have numerous applications in spectroscopy and quantum optics, see e. g. [101] and references herein. It was shown that Fourier spectroscopy is a proper tool for investigating the temporal coherence properties of single photon fluorescence emission from single quantum mechanical emitters (QME) in solids [102].

Single dye molecules, in particular, embedded in solid or condensed host matrices were found to fulfill the necessary condition for true SPS: The intensity correlation function $g^{(2)}(\tau)$ (see Eqn. 7) measured from single molecule fluorescence emission exhibits photon-antibunching on the time scale of the fluorescence lifetime (see e. g. [6,23–25,27] and inset in Fig. 27(b)), i. e. there is a diminishing probability for emission of two fluorescence photons at the same time. Just recently, it was reported that the spectrally isolated zero-phonon line emission of single dye molecules embedded in a crystalline matrix and cooled to cryogenic temperatures is a proper source of indistinguishable photons having coherence times in the nanosecond regime [93,94].

On the other hand, it turned out that at least three radiative properties of single dye molecules complicate their investigation by means of interferometric spectroscopy and limit their application in quantum optical experiments [23,93,94,101]:

1. The fluorescence spectra of single molecules at cryogenic temperatures consist of several emission lines reflecting the vibronic structure of the molecule. Hence, in any interferometric experiment, single molecule fluorescence emission has to be spectrally filtered additionally to prevent a rapid decay of temporal coherence of the emitted radiation.

2. The dipole emission of molecules in free space is almost isotropically and only a fraction of the fluorescence photons can be collected.

3. The onset of typical single molecule radiative fluctuations like reversible and irreversible photobleaching as well as spectral shifting disturbs or terminates any subsequent single photon experiment.

Embedding single molecules in a $\lambda/2$-microresonator could help to overcome the first two problems: The microresonator-controlled fluorescence emission is spectrally redistributed, i. e. filtered, and strongly redirected with respect to the collection optics (see chapter 7).

The radiative fluctuations of single molecules, however, cannot be reduced by the microresonator since they result from the interaction of the molecule with its local dielectric environment, i. e. the host matrix, which serves as a medium between the resonator mirrors (see chapter 2). In contrast to classical light sources and spectrally stable QME, e. g. atoms in the gas phase and color centers in solids [102–104], we therefore expect strong distortions of interference pattern.

Up to now, however, experimental investigations of how the radiative originalities of single molecule fluorescence emission affect the application of Fourier spectroscopy or, in other words, the quality of two-beam interference fringes, are lacking in the literature.

8.2   Experimental

The microresonator samples consisted of two resonator mirrors $M_{1,2}$ with a silver film thickness of 30 nm and 60 nm, respectively, resulting in a cavity-Q around 50 in the $\lambda/2$-regime (see chapter 2). A transparent polymer (n_{pol} = 1.56) doped with uniformly distributed and randomly oriented terrylene molecules (for structural formula see Fig. 26(a)) in low dopant concentrations ($c_{terrylene} \simeq 10^{-8}$ mol/l) served as an active medium between the resonator mirrors.

Measurements were performed with the low temperature setup described in chapter 1.3 and sketched in Fig. 2. For recording interferograms, the setup was equipped with a Michelson interferometer as introduced in chapter 1.3 and shown in Fig. 3(b).

8.3   Spectral Width and Temporal Coherence

To discuss the correlation between the spectral shape and the temporal coherence properties of microresonator-controlled single photon fluorescence emission, we need to briefly review the underlying physical principals.

The coherence length l_c of a single photon which is emitted by a single QME is given by the coherence time $\tau_c = l_c/c$ of the excited state that obeys Heisenberg's uncertainty principle $\Delta E \cdot \tau_c \geq h/2\pi$. Here, τ_c can be considered as both the dephasing time of the emitting excited state and the duration of the emitted wave train associated with the photon [102]. The phase and the number operators of photons do not commute [88] and the elongation of the wave train τ_c and its energy uncertainty ΔE cannot be measured for a single photon. For repeated excitation emission cycles of a single QME, however,

it was demonstrated that τ_c and ΔE become experimentally accessible. In particular, τ_c could be derived from the envelope of a two-beam interferogram which is related to the first order correlation function [88]

$$g^{(1)}(\tau) = \langle E(t+\tau)E^*(t)\rangle / \langle E^2(t)\rangle \qquad (9)$$

where E is the electric field associated with the emitted photons. The interferogram was measured on the output port of a Michelson interferometer by time-averaged detection of consecutive single fluorescence photons emitted by the same QME [102, 105].

This implies, on the other hand, that the coherence properties of single photons emitted by single QME can be derived from their time-averaged measured energy distribution, i. e. the power spectrum $\langle I(\omega)\rangle$, since the real part of $g^{(1)}(\tau)$ and $I(\omega)$ are associated via Fourier transform by the Wiener-Khinchin-Theorem [40].

If the QME is located inside a microresonator which restricts the spectral shape of the outcoupled emission, the coherence properties of the emitted photons are no longer only determined by the dephasing time of the excited state of the QME: They strongly depend on the characteristic decay time of the microresonator or, in other words, its photon storage time. As a result, the microresonator filters the statistical fluctuations of embedded QME [95].

As it was discussed in chapters 2 and 4, the free-space fluorescence spectra of single molecules at room temperature show strong homogeneous spectral broadening and exceed the spectral width of the transmission profile of the microresonator (see Fig. 11 and Fig. 19). In this case, the microresonator determines the spectral shape of the microresonator-controlled single molecule fluorescence emission and we were able to resolve its spectral width experimentally. Hence, the coherence length l_c of the fluorescence emission can be derived from the measured spectra by Fourier transform and we estimated a 1/e-value of $l_c \simeq 13.5$ μm which corresponds to $\tau_c = 45$ fs for the case shown in the lower panel of Fig. 11.

In contrast, at $T = 1.8$ K, the single molecule fluorescence emission consist of several vibronic lines which are considerably narrower than the transmission spectrum of the microresonator (see Fig. 28(b)). In the following, we investigate the simplest case as sketched in Fig. 28(a) and shown in the lower panel of Fig. 28(b) where the zero-phonon line (ZPL), i. e. the narrowest fluorescence line corresponding to the purely electronic transition (see also chapter 7), is on resonance with the forward mode of the microresonator

and remains as the only significant spectral feature in the microresonator-controlled emission spectrum. In our measured fluorescence spectra, the spectral width of the ZPL always displays the instrument response function of our spectrometer having a width of $FWHM_{irf} \simeq 0.15$ nm for a grating with 1200 grooves per mm. Since the transmission spectrum of the microresonator is broad compared to the fluorescence emission of embedded molecules, the coherence properties of microresonator-controlled single molecule fluorescence are expected to be predominated by the coherence properties of the emitter [95]. The upper limit of the coherence time τ_c of the emitter, i. e. a single terrylene molecule, is given by the microresonator-controlled fluorescence lifetime (see also chapter 3) which was measured to be $\tau_{meas} \simeq 2$ ns in the present case (see also inset Fig. 27(b) in chapter 7).

As already mentioned before, single molecules were found to exhibit strong intensity fluctuations on timescales between milliseconds and seconds even at cryogenic temperatures (see Fig. 27(a)) as well as spectral jumps of the ZPL within a range of up to a few nanometers which occur on the timescale of seconds. Hence, we expect that the time-averaged two-beam interferograms acquired on single dye molecules depend strongly on the data acquisition time and that the quantification of l_c and τ_c, respectively, as well as the derivation of Fourier transform spectra from experimental interferograms might be complicated.

8.4 Single Photon Two-Beam Interference

Assuming a monochromatic, parallel light beam entering a Michelson interferometer, the intensity distribution on the detector is given by

$$I(z) = 2r^2t^2 \langle I(t) \rangle \{1 + V(z)cos[2\pi\tilde{\nu}(z - z_o)]\} \tag{10}$$

where r and t are the reflection and transmission coefficients, respectively, of the beam splitter and $\langle I(t) \rangle$ is the time-averaged intensity of the monochromatic plane wave with wave number $\tilde{\nu} = 1/\lambda$ guided through the interferometer. The visibility of interference fringes $V(z)$ is defined as

$$V(z) = \frac{I_{max} - I_{min}}{I_{max} + I_{min}} \tag{11}$$

where I_{max} and I_{min} are adjacent intensity maxima and minima, respectively, of the interferogram acquired as function of the displacement $z/2$ of the moving interferometer mirror (see Fig. 3(b)). Note, that $V(z)$ is the envelope of the overall interferogram and a direct measure for the modulus of
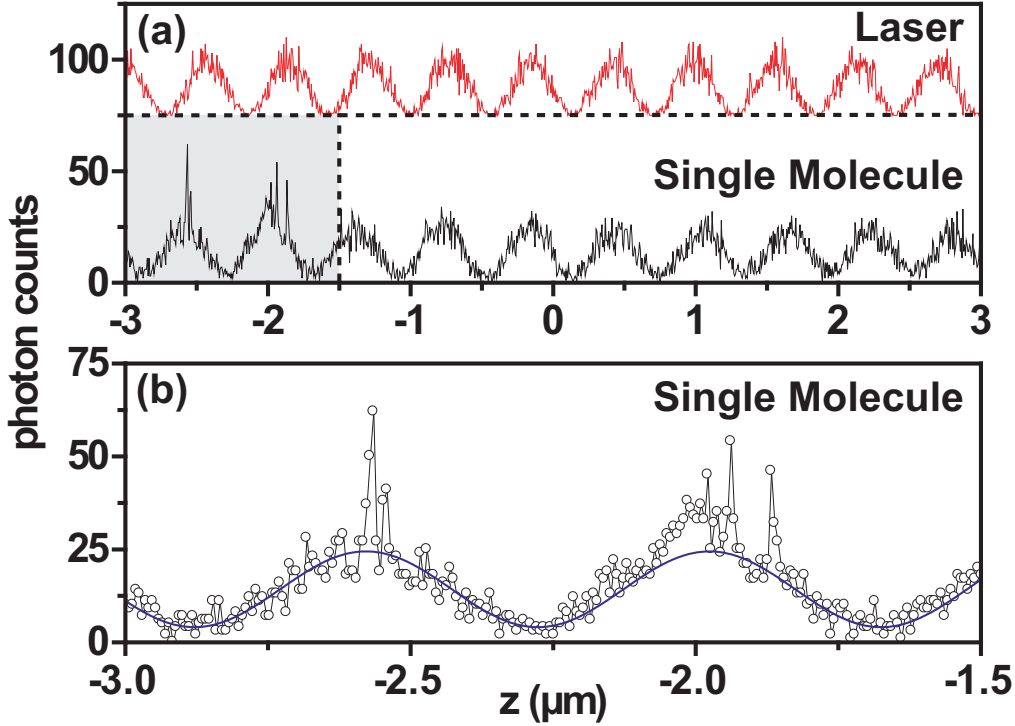
Figure 31: (a) Two-beam interferograms (lines) measured for the excitation laser ($\lambda_{laser} \simeq 570$ nm) and the single molecule fluorescence emission at $T = 1.8$ K ($\lambda_{molecule} \simeq 600$ nm), respectively, around zero path difference of the interferometer (ZPD, $z = 0$) as discussed in the text. The integration times per data point were 20 ms and 50 ms, respectively, for the laser interferogram and the single molecule interferogram. The laser interferogram is offset by 75 photon counts with respect to the single molecule interferogram to improve clarity. (b) Magnified section of the single molecule interferogram (circles) as indicated by the grey shaded area in (a). The interference fringes are distorted due to strong intensity fluctuations in the fluorescence emission of the observed molecule. A fit to the data (line) according to Eqn. 10 is also shown.

the first order coherence function $g^{(1)}$ (see Eqn. 9) and hence l_c and τ_c, respectively [40]. The offset z_o accounts for an asymmetry between both paths of the interferometer introduced by the beam splitter cube: We found that white light reference interferograms measured with our interferometer show a slight asymmetry with an intensity minimum, i. e. a dark fringe, in the center [106]. For the spectrally narrow radiation investigated in the following, we neglect this asymmetry. Nevertheless, we refer to zero delay $z = 0$

between the two pathes in the interferometer as zero path difference (ZPD) which was chosen to be the position of the intensity minimum in the center of the single molecule interferogram shown in Fig. 32. For acquiring double sided interferograms, the ZPD was tuned to the center of the total scanning range. Hence, the maximum difference between the two light pathes inside the interferometer was $z_{max} = 100$ μm which corresponds to a delay time $\tau_{max} = 0.33$ ps assuming vacuum velocity of light.

In Fig. 31(a), two interferograms measured for the excitation laser (upper curve, $\lambda_{laser} \simeq 570$ nm) and the single molecule emission (lower curve, $\lambda_{mol} \simeq 600$ nm), respectively, are shown for small path differences z. A constant offset of 75 photon counts was added to the laser interferogram in the figure to allow for comparison. Due to the small step width $\Delta z \simeq 6$ nm between adjacent data points, we could clearly resolve the interference fringes: Both curves show cosine modulation as expected for monochromatic two-beam interferograms (see Eqn. 10). The maximum visibility derived from measured laser interferograms was $V_{max}(z) = 0.95 \pm 0.02$. For low detector count rates, I_{min} and hence V was found to be limited by the dark count rate of the detector, i. e. $\Gamma_D \simeq 50$ Hz. The different integration times for the interferograms shown in Fig. 31 were accounted by adding the corresponding detector dark counts to the laser interferogram before fitting the data with a model function according to Eqn. 10. The fits show excellent agreement with the measured curves and we obtained $V_{laser}(z) = (0.84 \pm 0.01)$ and $V_{molecule}(z) = (0.71 \pm 0.02)$, respectively (see also Eqn. 11). The large difference between the emission wavelengths of the laser and the molecule (around 30 nm) result in a decreasing overlap between both interferograms becoming obvious around $z_{max} = \pm 3$ μm.

In the z-regime between -3 μm and -1.5 μm (grey shaded area in Fig. 31(a)), the interferogram measured on the molecule exhibits strong intensity fluctuations. This part of the interferogram is shown in Fig. 31(b) together with a fit according to Eqn. 10. Here, the cosine fringes are distorted and deviate clearly from both the fit function and the laser interferogram.

As a result, we found that the interferograms measured for laser light and microresonator-controlled single molecule fluorescence emission around $z = 0$ could not be clearly distinguished by their visibility $V(z)$. This means that at least for small z (or τ) the correlations of the respective optical fields expressed by $g^{(1)}(\tau)$ (see Eqn. 9) are nearly the same for both the laser light and the single molecule fluorescence emission while their intensity correlations given by $g^{(2)}(\tau)$ (see Eqn. 7) differ significantly (see inset in Fig. 27(b)).

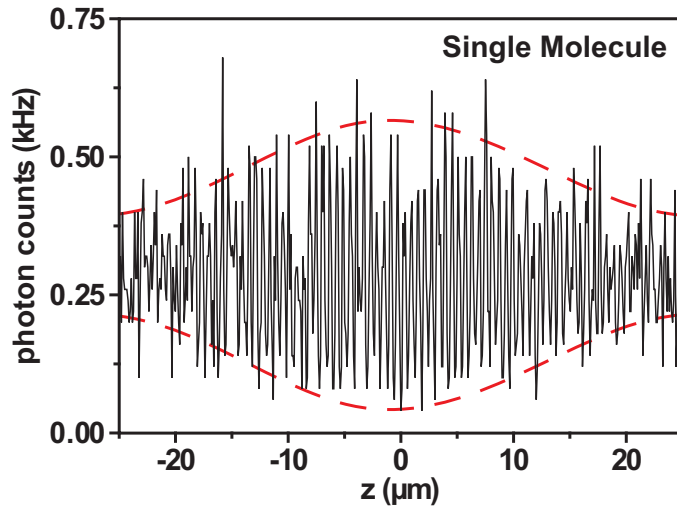In particular, the two-beam interferograms were found to be insensitive

Figure 32: Section of a double sided interferogram (line) measured on a single terrylene molecule embedded in the microresonator at $T = 1.8$ K as discussed in the text. The dashed lines indicate the decay of visibility $V(z)$ of the interferogram with increasing delay z.

to small spectral jumps as observed in the molecular fluorescence emission with our grating spectrometer: An intermediate shift of the emission wavelength around one nanometer could not be recognized from the measured interferograms because of the small path difference z in the interferometer, as expected.

In Fig. 32, a section from a double sided interferogram offering larger delays z is shown. It was acquired from the same molecule which was investigated above (see Fig. 31). The cosine modulations are partially distorted due to intensity fluctuations of the single molecule. Surprisingly, the envelope of the overall interferogram shows a decay of the visibility $V(z)$ (see Eqn. 11) on this z-scale as indicated by the dashed lines which serves as a guide to the eye. From the spectral width of the ZPL as measured with our grating spectrometer, we would not expect a noticeable decay of V(z) within the total scanning range z_{max} of our interferometer.

In the following, we demonstrate that this fast decay of $V(z)$ is inferred by an additional spectral component in the microresonator-controlled single molecule fluorescence spectrum, i. e. the phonon side band accompanying the ZPL on the red side of the spectrum.

8.5 Zero-Phonon Line, Phonon Wing and the Debye-Waller factor

In Fig. 33(a), a fluorescence spectrum (circles) of a single terrylene molecule embedded in the microresonator is shown, offering excellent signal to noise ratio. The mirror spacing is tuned on resonance with the purely electronic transition $S_{1,0} \to S_{0,0}$ of the terrylene molecule and the measured spectral width of the ZPL displays the instrument response function of our spectrometer.

Obviously, the measured spectrum consists not only of the ZPL: An additional feature, i. e. the so-called phonon wing, directly follows the ZPL on the red side of the spectrum and extends over a spectral range of around 5 nm having a width of approximately 2.5 nm as indicated in Fig. 33(a). The phonon wing originates from residual electron-phonon coupling between the molecule and the host matrix [9]. Due to the large spectral width of the on-axis transmission spectrum of the microresonator (dots, $FWHM = 14$ nm), it was not possible to spectrally isolate the ZPL of single terrylene molecules from the red-shifted phonon wing by means of the microresonator: If the ZPL is on resonance with the forward mode of the microresonator, the phonon wing also inevitably fits into the resonance window that is determined by the spectral width of the local on-axis transmission profile.

From a set of spectra comparable to that one shown in Fig. 33(a), we derived a Debye-Waller factor $F_{DW} = I_{ZPL}/(I_{ZPL} + I_{PW}) = 0.5 \pm 0.1$, where I_{ZPL} is the measured integrated intensity of the ZPL-emission and I_{PW} is the measured integrated intensity spectrally dispersed over the red-shifted phonon wing. Neglecting residual contributions of incompletely suppressed vibronic lines at higher emission wavelengths, the derived F_{DW}-value implies that on average only every second detected photon belongs to the spectrally narrow ZPL emission. Hence, if the ZPL emission is not spectrally isolated from the entire microresonator-controlled emission including the phonon wing, the coherence properties of the radiation are strongly influenced by the large spectral width of the phonon wing and, as a result, V decays rapidly with increasing z. It should be remarked that a comparable decay of the visibility of two-beam interference fringes induced by the phonon sideband was already observed in the low temperature fluorescence emission of a single nitrogen-vacancy defect in diamond [102].
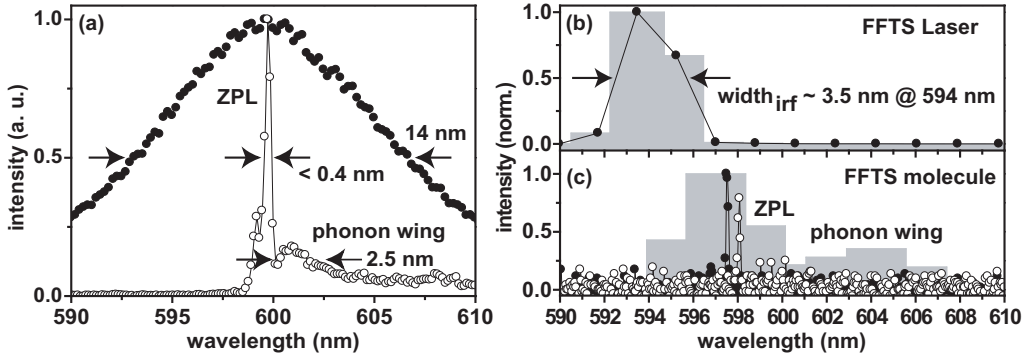
Figure 33: (a) Grating spectrum (grating: 600 grooves per mm) of microresonator-controlled fluorescence emission of a single terrylene molecule (circles) offering high signal to noise ratio. The purely electronic transition appears in the spectrum as the zero-phonon line (ZPL) which is on-resonance with the forward mode of the microresonator as indicated by a measured on-axis transmission profile (dots). The phonon wing accompanying the ZPL also fits in the resonance window of the microresonator. (b) Fast Fourier Transform spectrum (FFTS) (grey histogram bars) obtained from a laser interferogram as discussed in the text. To improve clarity, the sampling points of the FFT spectrum are additionally marked by dots and connected with lines. (c) FFT spectrum (grey histogram bars) obtained from an interferogram acquired on the microresonator-controlled fluorescence emission of a single terrylene molecule at $T = 1.8$ K clearly exhibiting the significant spectral features, i. e. the ZPL and the phonon wing (see also (a) for comparison). Two representative high-resolution grating spectra (grating: 1200 grooves per mm) acquired from the same molecule (dots, circles) are also shown indicating the intensity fluctuations and the spectral jumps, respectively, of the ZPL emission.

8.6 Single Molecule Fourier Transform Fluorescence Spectra

We now discuss the applicability of Fourier transform spectroscopy for unstable fluorescing molecules by comparing the spectrum obtained from a measured single molecule fluorescence interferogram with the corresponding spectroscopic data acquired with a grating spectrometer.

In Fig. 33, Fast Fourier Transform (FFT) spectra are shown calculated for both a double sided laser interferogram (Fig. 33(b), $\lambda_{laser} \simeq 594$ nm) and a double sided single molecule fluorescence interferogram (Fig. 33(c), $\lambda_{mol} \simeq 600$ nm). The delay z extended from -100 μm to +100 μm and 2048

data points were acquired for each interferogram which resulted in a step width $\Delta z \simeq 100$ nm. After applying FFT to the interferograms, we obtained the corresponding power spectra $I(\tilde{\nu})$ with a step width of $\Delta \tilde{\nu} = 50$ cm^{-1}. The FFT spectra were normalized to their respective intensity maximum. In the following, we refer the FFT spectra to a wavelength scale to compare them with spectroscopic data acquired with a grating spectrometer. For the acquisition parameters mentioned above, the FFT spectrum obtained from the laser interferogram (see Fig. 33(b)) can be considered as the measured instrument response function of our Fourier spectrometer. The intensity in the spectrum was found to spread over two FFT channels, i. e. two data points in the FFT spectrum, which are represented by grey histogram bars. To improve clarity, the positions of FFT channels are additionally marked by dots and connected with lines. For the spectral range around 590 nm, we found that the spectral width of the measured instrument response function is around 3.5 nm as indicated by arrows in Fig. 33(b).

In contrast, the FFT spectrum obtained from the interferogram measured on the single terrylene molecule exhibits two contributions: The ZPL and the red-shifted phonon wing are spectrally resolved and clearly visible in the spectrum as can be seen in Fig. 33(c). The ZPL has a spectral width of around 3.5 nm in good agreement with width of the measured instrument response function, i. e. the laser line in the FFT spectrum (see Fig. 33(b)). The phonon wing spectrally extends over 6 nm in good agreement with the value obtained from the grating reference spectrum shown in Fig. 33(a).

Although we observed strong intensity fluctuations distorting the single molecule interferogram (see Fig. 32), the FFT spectrum resembles well the relative spectral distribution of the ZPL and the phonon wing as can be seen by comparison with the reference grating spectrum shown in Fig. 33(a). The Debye-Waller factor $F_{DW} = 0.6\pm0.1$ estimated from the single molecule FFT spectrum (see Fig. 33(c)) nicely agrees with the values derived from grating spectra as discussed above.

To confirm the spectral position of the ZPL as it was observed in the FFT spectrum, we measured series of high resolution fluorescence spectra on the same molecule using the grating spectrometer. Two respresentative grating spectra (dots, circles) are shown for comparison in Fig. 33(c). Both spectra were normalized to the intensity maximum occurring in the dotted spectrum to highlight the intensity fluctuations in the ZPL emission. We found that the spectral position of the ZPL as measured with the grating spectrometer exactly fits to the position of the intensity maximum of the FFT spectrum as can be seen in Fig. 33(c). Due to the high spectral resolution of the grating spectrometer, we could clearly resolve small spectral jumps of the ZPL position up to $\pm$ 1 nm occurring on the time scale of seconds.

Obviously, these spectral jumps are not observable in the FFT spectrum since the spectral resolution is too small.

In the case of the grating spectra shown in Fig. 33(c), the high spectral resolution (grating: 1200 grooves per mm) is gained at the cost of the signal to noise ratio: Compared to the spectrum shown in Fig. 33(a) which was measured with lower spectral resolution (grating: 600 grooves per mm), the signal to noise ratio is not sufficient to reveal the red-shifted phonon wing.

As a result, we found that single molecule Fourier spectroscopy delivers reliable power spectra, even if the measured interferograms suffer from the strong intensity fluctuations of the observed molecule. If the frequency jumps occurring in single molecule fluorescence emission are below the spectral resolution of the Fourier spectrometer, they do not affect the quality of the power spectra obtained by FFT.

8.7 Beating induced by the Phonon Wing

We now compare the visibility $V(z)$ of the laser interferogram and the single molecule fluorescence interferogram for z ranging from 0 μm to 100 μm corresponding to delay times τ between 0 ps and 0.33 ps.

In Fig. 34, $V(z)$ is shown for the laser interferogram (diamonds) and, separately, for both sides of the single molecule interferogram (dots, circles). Additionally, the visibility of a background fluorescence interferogram (squares) acquired at $T = 160$ K with a fast exponential decay (dotted line) is shown for comparison. $V(z)$ was calculated for each measured interferogram according to Eqn. 11 as a function of the delay z.

The visibility of the laser interferogram was found to be rather constant (around 0.85) over the entire scan range of the Michelson interferometer and in good agreement with a linear fit to the data (line).

In contrast, as it was already discussed above (see also Fig. 32), the single molecule fluorescence interferogram shows a fast decay of the visibility from $V(z = 0 \text{ μm}) \simeq 0.7$ to $V(z = 20 \text{ μm}) \simeq 0.3$. For increasing z, $V(z)$ increases and exhibits a local maximum $V(z = 55 \text{ μm}) \simeq 0.5$ until it decays again to $V(z = 100 \text{ μm}) \simeq 0.4$.

We assign the local maximum or, in other words, the beating occurring in $V(z)$, to the spectral width of the phonon wing. We proof this by Fourier transforming a grating spectrum measured on the same molecule for long integration times, i. e. calculating an interferogram for the respective spectral distribution. From the calculated interferogram, we derive $V(z)$ and the result is shown in Fig. 34 as a dashed line: The curve samples the decay of $V(z)$ as derived from the measured single molecule fluorescence interferogram
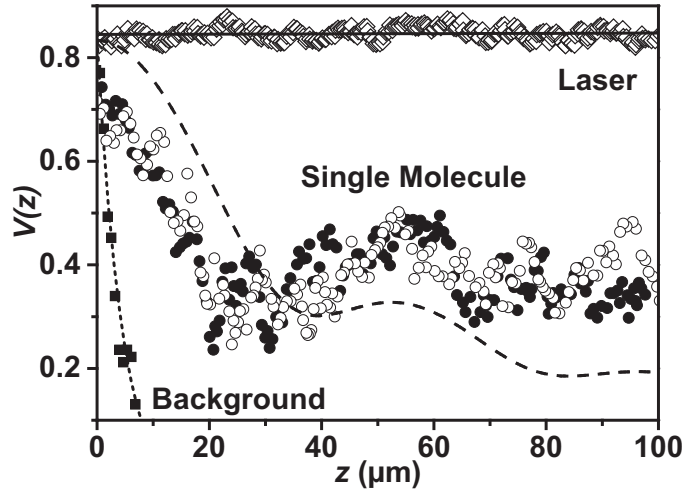
Figure 34: Visibility V derived from three representative measured interferograms as a function of the delay z between both light paths in a Michelson interferometer. The visibility of a reference laser interferogram (diamonds) is rather constant as can be seen from a linear fit to the data (line). The visibility derived from a single molecule interferogram acquired at $T = 1.8$ K (dots, circles) is shown together with the visibility curve of a calculated interferogram (dashed line) based on a grating spectrum acquired on the same molecule. The visibility of a fluorescence background interferogram acquired at $T = 160$ K (squares) was found to be in agreement with an exponential decay law (dotted line).

(dots, circles) and the z-positions for the beating maxima overlap well at z around 55 µm.

We confirmed the influence of the phonon wing on $V(z)$ by Fourier transforming a set of grating spectra comparable to that one shown in Fig. 32 and derived an estimate for $V(z)$ for the spectrally isolated ZPL emission: The resulting curve did not show a significant deviation from $V(z)$ as measured for the laser (see Fig. 34).

Obviously, there is a systematic deviation between the $V(z)$-curves as derived from the measured and the calculated interferogram: For small z ranging between 0 µm and 30 µm, the visibility of the calculated interferogram is higher than that of the measured one. In contrast, for $z > 30$ µm, the visibility of the calculate interferogram drops significantly below the visibility of the measured interferogram.

We attribute these deviations to the influence of the different acquisition procedures and data acquisition time scales: Since the width of the spectral distribution artificially increases with observation time due to the spectral

diffusion of the single molecule fluorescence emission, the grating spectra acquired on the time scale of several seconds show a spectral distribution which is broad compared to the instantaneous spectral distribution during acquisition of an interferogram sampling point which was performed in 50 ms.

This has an important implication on the time-averaged measurement of the coherence length l_c of single photons emitted by single molecules using Fourier spectroscopy: The data acquisition time for interferogram sampling points has to be shorter than the time scale of the single molecule spectral jumps. Otherwise, the time-averaging additionally reduces the visibility of the interferogram. As a result, the measured l_c-value is systematically smaller than the value which could be obtained from the same molecule by observing the spectrally stable emission between consecutive spectral jumps.

Finally, we discuss the temporal coherence properties of the single photon emission as derived from the interferogram measured on the single molecule: As can be seen in Fig. 34, $V(z)$ does not clearly drop below 0.25 (i. e. the 1/e-value of $V_{max} = V(z = 0) = 0.7$) in the entire z-range and hence we can not derive l_c from our experimental data maintaining high visibility of interference fringes in the entire scan range.

On the other hand, we observed extremely high visibility of interference fringes only within a z-range of a few micron around ZPD (see also Fig. 31(a)). $V(z)$ was found to decay rapidly for z approaching 20 μm (see also Fig. 32) and exhibits beatings due to contributions of photons associated with the broad red-shifted phonon wing.

8.8   Summary and Conclusion

In summary, we have investigated the single photon fluorescence emission of single spatially isolated terrylene molecules embedded in a $\lambda/2$-microresonator at $T = 1.8$ K with a Michelson interferometer. We examined the visibility of two-beam interferograms which were acquired photon by photon from the molecular zero-phonon line emission for path differences up to 100 μm, i. e. a delay time of 0.33 ps. By comparison with grating spectroscopy, we proofed the applicability of Fourier transform spectroscopy for fluorescent dye molecules showing strong intensity fluctuations and spectral jumps. Within the accessible scan range of our interferometer, the excellent visibility of the single molecule fluorescence interferograms did not drop below the 1/e-value of the visibility maximum of 0.7 which occurred around zero path difference, but was found to be strongly modulated due to contributions of photons associated with the phonon wing accompanying the zero-phonon emission line.

The experimental realization of single molecule Fourier spectroscopy as presented here can be considered as an important step for single molecule spectroscopy and for the investigation of the temporal coherence properties of single photon sources based on single molecules.

References

[1] H. Mabuchi and A. C. Doherty, "Cavity Quantum Electrodynamics: Coherence in Context," Science **298**, 1372–1377 (2002).

[2] M. Born and E. Wolf, *Principles of optics* (Pergamon Press, Oxford, 1980), 6 edn.

[3] H. Yokoyama and K. Ujihara, *Spontaneous Emission and Laser Oscillation in Microcavities* (CRC Press, Boca Raton, 1995).

[4] R. K. Chang and A. J. Campillo, *Optical Processes In Microcavities* (World Scientific, Singapore, 1996).

[5] K. J. Vahala, "Optical microcavities," Nature **424**, 839–846 (2003).

[6] T. Basché, W. E. Moerner, M. Orrit, and H. Talon, "Photon Antibunching in the Fluorescence of a Single Dye Molecule Trapped in a Solid," Phys. Rev. Lett. **69**, 1516–1519 (1992).

[7] P. Tamarat, B. Lounis, J. Bernard, M. Orrit, S. Kummer, R. Kettner, S. Mais, and T. Basché, "Pump-Probe Experiments with a Single Molecule: ac-Stark Effect and Nonlinear Optical Response," Phys. Rev. Lett. **75**, 1514–1517 (1995).

[8] C. Brunel, B. Lounis, P. Tamarat, and M. Orrit, "Rabi Resonances of a Single Molecule Driven by rf and Laser Fields," Phys. Rev. Lett. **81**, 2679–2682 (1998).

[9] T. Basché, W. E. Moerner, M. Orrit, and U. P. Wild, *Single-Molecule Optical Detection, Imaging and Spectroscopy* (Weinheim, New York, 1996).

[10] F. Kulzer and M. Orrit, "Single-Molecule Optics," Ann. Rev. Phys. Chem. **55**, 585–611 (2004).

[11] R. H. Webb, "Confocal optical microscopy," Rep. Prog. Phys **59**, 427–471 (1996).

[12] F. De Martini, M. Marrocco, P. Mataloni, L. Crescentini, and R. Loudon, "Spontaneous emission in the optical microscopic cavity," Phys. Rev. A **43**, 2480–2497 (1991).

[13] P. K. H. Ho, D. S. Thomas, R. H. Friend, and N. Tessler, "All-Polymer Optoelectronic Devices," Science **285**, 233–236 (1999).

[14] Q. Song, L. Liu, X. Shumin, X. Zhou, W. Wang, and L. Xu, "Unidirectional High Intensity Narrow-Linewidth Lasing from a Planar Random Microcavity Laser," Phys. Rev. Lett. **96**, 033 902 (2006).

[15] A. J. Bennett, D. C. Unitt, P. See, A. J. Shields, P. Atkinson, K. Cooper, and D. A. Ritchie, "Microcavity single-photon-emitting diode," Appl. Phys. Lett. **86**, 181 102 (2005).

[16] M. A. Weber, *Hochauflösende Lasermikroskopie and einzelnen Molekülen*, Ph.D. thesis, University of Siegen (1999).

[17] M. A. Lieb, *Mikroskopie mit Parabolspiegeloptik*, Ph.D. thesis, University of Siegen (2001).

[18] A. Hagen, M. Steiner, M. B. Raschke, C. Lienau, T. Hertel, H. Qian, A. J. Meixner, and A. Hartschuh, "Exponential Decay Lifetimes of Excitons in Individual Single-Walled Carbon Nanotubes," Phys. Rev. Lett. **95**, 197 401 (2005).

[19] A. Hartschuh, H. N. Pedrosa, J. Peterson, L. Huang, P. Anger, H. Qian, A. J. Meixner, M. Steiner, L. Novotny, and T. D. Krauss, "Single Carbon Nanotube Optical Spectroscopy," ChemPhysChem **6**, 577–582 (2005).

[20] L. Huang, A. Hartschuh, H. N. Pedrosa, J. Peterson, M. Steiner, L. Novotny, and T. D. Krauss, "Single carbon nanotube photonics," Proc. SPIE **5732**, 1–13 (2005).

[21] L. Huang, A. Hartschuh, H. N. Pedrosa, J. Peterson, M. Steiner, L. Novotny, and T. D. Krauss, "Individual single-wall carbon nanotube photonics," Proc. SPIE **5513**, 1–13 (2004).

[22] R. Hanbury Brown and R. Q. Twiss, "Correlation between photons in two coherent beams of light," Nature **177**, 27–29 (1956).

[23] C. Brunel, B. Lounis, P. Tamarat, and M. Orrit, "Triggered Source of Single Photons based on Controlled Single Molecule Fluorescence," Phys. Rev. Lett. **83**, 2722–2725 (1999).

[24] B. Lounis and W. E. Moerner, "Single photons on demand from a single molecule at room temperature," Nature **407**, 491–493 (2000).

[25] L. Fleury, J.-M. Segura, G. Zumofen, B. Hecht, and U. P. Wild, "Nonclassical Photon Statistics in Single-Molecule Fluorescence at Room Temperature," Phys. Rev. Lett. **84**, 1148–1151 (2000).

[26] F. Treussart, A. Clouqueur, C. Grossman, and J.-F. Roch, "Photon antibunching in the fluorescence of a single dye molecule embedded in a thin polymer film," Opt. Lett. **26**, 1504–1506 (2001).

[27] F. Treussart, R. Alléaume, V. Le Floc'h, L. T. Xiao, J.-M. Courty, and J.-F. Roch, "Direct Measurement of the Photon Statistics of a Triggered Single Photon Source," Phys. Rev. Lett. **89**, 093 601 (2002).

[28] S. G. Lukishova, A. W. Schmid, A. J. McNamara, R. W. Boyd, and C. R. Stroud Jr., "Room Temperature Single-Photon Source: Single-Dye Molecule Fluorescence in Liquid Crystal Host," IEEE J. Select. Top. Quantum Electron. **9**, 1512–1518 (2003).

[29] W. E. Moerner, "Single-photon sources based on single molecules in solids," New Journal of Physics **6**, 1–21 (2004).

[30] E. Knill, R. Laflamme, and G. J. Milburn, "A scheme for efficient quantum computation with linear optics," Nature **409**, 46–52 (2001).

[31] N. Gisin, G. Ribordy, W. Tittel, and H. Zbinden, "Quantum cryptography," Rev. Mod. Phys. **74**, 145–195 (2002).

[32] W. Becker, H. Hickl, C. Zander, K. H. Drexhage, M. Sauer, S. Siebert, and J. Wolfrum, "Time-resolved detection and identification of single analyte molecules in microcapillaries by time-correlated single-photon counting (TCSPC)," Rev. Sci. Instrum. **70**, 1853–1841 (1999).

[33] L.-Q. Li and L. M. Davis, "Rapid and efficient detection of single chromophore molecules in aqueous solution," Appl. Opt. **34**, 3208–3217 (1995).

[34] F. De Martini, G. Di Giuseppe, and M. Marrocco, "Single-Mode Generation of Quantum Photon States by Excited Single Molecules in a Microcavity Trap," Phys. Rev. Lett. **76**, 900–903 (1996).

[35] S. C. Kitson, P. Jonsson, J. G. Rarity, and P. R. Tapster, "Intensity fluctuation spectroscopy of small numbers of dye molecules in a microcavity," Phys. Rev. A **58**, 620–627 (1998).

[36] M. D. Barnes, N. Lermer, C.-Y. Kung, W. B. Whitten, J. M. Ramsey, and S. C. Hill, "Real-time observation of single-molecule fluorescence in microdroplet streams," Opt. Lett. **22**, 1265–1267 (1997).

[37] F. De Martini, M. Marrocco, and D. Murra, "Transverse Quantum Correlations in the Active Microscopic Cavity," Phys. Rev. Lett. **65**, 1853–1856 (1990).

[38] R. E. Kunz and W. Lukosz, "Changes in fluorescence lifetimes induced by variable optical environments," Phys. Rev. B **21**, 4814–4828 (1980).

[39] H. Becker, S. E. Burns, N. Tessler, and R. H. Friend, "Role of optical properties of metallic mirrors in microcavity structures," J. Appl. Phys. **81**, 2825–2829 (1997).

[40] S. G. Lipson, H. S. Lipson, and D. S. Tannhauser, *Optik* (Springer, Berlin, 1997).

[41] E. Fermi, "Quantum Theory of Radiation," Rev. Mod. Phys. **4**, 87–132 (1932).

[42] E. M. Purcell, "Spontaneous Emission Probabilities at Radio Frequencies," Phys. Rev. **69**, 681 (1946).

[43] P. Stehle, "Atomic Radiation in a Cavity," Phys. Rev. A **2**, 102–106 (1970).

[44] D. Kleppner, "Inhibited Spontaneous Emission," Phys. Rev. Lett. **47**, 233–236 (1981).

[45] F. De Martini, G. Innocenti, G. R. Jacobovitz, and P. Mataloni, "Anomalous Spontaneous Emission Time in a Microscopic Optical Cavity," Phys. Rev. Lett. **59**, 2955–2958 (1987).

[46] H. Yokoyama, K. Nishi, T. Anan, H. Yamada, S. D. Brorson, and E. P. Ippen, "Enhanced spontaneous emission from GaAs quantum wells in monolithic microcavities," Appl. Phys. Lett. **57**, 2814–2816 (1990).

[47] M. Suzuki, H. Yokoyama, S. D. Brorson, and E. P. Ippen, "Observation of spontaneous emission lifetime change of dye-containing Langmuir-Blodgett films in optical microcavities," Appl. Phys. Lett. **58**, 998–1000 (1991).

[48] T. Yamauchi, Y. Arakawa, and M. Nishioka, "Enhanced and inhibited spontaneous emission in GaAs/AlGaAs vertical microcavity lasers with two kinds of quantum wells," Appl. Phys. Lett. **58**, 2339–2341 (1991).

[49] A. M. Vredenberg, N. E. J. Hunt, E. F. Schubert, D. C. Jacobson, J. M. Poate, and G. J. Zydzik, "Controlled Atomic Spontaneous Emission from Er^{3+} in a Transparent Si/SiO_2 Microcavity," Phys. Rev. Lett. **71**, 517–520 (1993).

[50] P. T. Worthing, J. A. E. Wasey, and W. L. Barnes, "Rate and efficiency of spontaneous emission in metal-clad microcavities," J. Appl. Phys. **89**, 615–625 (2001).

[51] J. M. Gérard, B. Sermage, B. Gayral, B. Legrand, E. Costard, and V. Thierry-Mieg, "Enhanced Spontaneous Emission by Quantum Boxes in a Monolithic Optical Microcavity," Phys. Rev. Lett. **81**, 1110–1113 (1998).

[52] M. Bayer, T. L. Reinecke, F. Weidner, A. Larionov, A. McDonald, and A. Forchel, "Inhibition and Enhancement of the Spontaneous Emission of Quantum Dots in Structured Microresonators," Phys. Rev. Lett. **86**, 3168–3171 (2001).

[53] H.-B. Lin, J. D. Eversole, C. D. Merritt, and A. J. Campillo, "Cavity-modified spontaneous-emission rates in liquid microdroplets," Phys. Rev. A **45**, 6756–6760 (1992).

[54] M. D. Barnes, C.-Y. Kung, W. B. Whitten, J. M. Ramsey, S. Arnold, and S. Holler, "Fluorescence of Oriented Molecules in a Microcavity," Phys. Rev. Lett. **76**, 3931–3934 (1996).

[55] H. Schniepp and V. Sandoghdar, "Spontaneous Emission of Europium Ions Embedded in Dielectric Nanospheres," Phys. Rev. Lett. **89**, 257 403 (2002).

[56] P. Goy, J. M. Raimond, M. Gross, and S. Haroche, "Observation of Cavity-Enhanced Single-Atom Spontaneous Emission," Phys. Rev. Lett. **50**, 1903–1906 (1983).

[57] R. G. Hulet, E. S. Hilfer, and D. Kleppner, "Inhibited Spontaneous Emission by a Rydberg Atom," Phys. Rev. Lett. **55**, 2137–2140 (1985).

[58] W. Jhe, A. Anderson, E. A. Hinds, D. Meschede, L. Moi, and S. Haroche, "Suppression of Spontaneous Decay at Optical Frequencies: Test of Vacuum-Field Anisotropy in Confined Space," Phys. Rev. Lett. **58**, 666–669 (1987).

[59] A. Kreuter, C. Becher, G. P. T. Lancaster, A. B. Mundt, C. Russo, H. Häffner, C. Roos, J. Eschner, F. Schmidt-Kaler, and R. Blatt, "Spontaneous Emission Lifetime of a Single Trapped Ca^+ Ion in a High Finesse Cavity," Phys. Rev. Lett. **92**, 203 002 (2004).

[60] G. S. Solomon, M. Pelton, and Y. Yamamoto, "Modification of Spontaneous Emission of a Single Quantum Dot," phys. stat. sol. (a) **178**, 341–344 (2000).

[61] G. S. Solomon, M. Pelton, and Y. Yamamoto, "Single-mode Spontaneous Emission from a Single Quantum Dot in a Three-Dimensional Microcavity," Phys. Rev. Lett. **86**, 3903–3906 (2001).

[62] A. Kiraz, P. Michler, C. Becher, B. Gayral, A. Imamoğlu, L. Zhang, E. Hu, W. V. Schoenfeld, and P. M. Petroff, "Cavity-quantum electrodynamics using a single InAs quantum dot in a microdisk structure," Appl. Phys. Lett. **78**, 3932–3934 (2001).

[63] F. De Martini, F. Cairo, P. Mataloni, and F. Verzegnassi, "Thresholdless microlaser," Phys. Rev. A **46**, 4220–4233 (1992).

[64] K. Ujihara, "Spontaneous Emission and the Concept of Effective Area in a Very Short Optical Cavity with Plane-Parallel Dielectric Mirrors," Jpn. J. Appl. Phys. **30**, L901–L903 (1991).

[65] G. Björk, H. Heitmann, and Y. Yamamoto, "Spontaneous-emission coupling factor and mode characteristics of planar dielectric microcavity lasers," Phys. Rev. A **47**, 4451–4463 (1993).

[66] F. De Martini and G. R. Jacobovitz, "Anomalous Spontaneous-Stimulated-Decay Phase Transition and Zero-Threshold Laser Action in a Microscopic Cavity," Phys. Rev. Lett. **60**, 1711–1714 (1988).

[67] J. R. Lakowicz, *Principles of Fluorescence Spectroscopy* (Kluwer Academic / Plenum Publishers, New York, 1999), 2 edn.

[68] R. R. Chance, A. Prock, and R. Silbey, "Lifetime of an emitting molecule near a partially reflecting surface," J. Chem. Phys. **60**, 2744–2748 (1974).

[69] Z. Shen, P. E. Burrows, V. Bulović, S. R. Forrest, and M. E. Thompson, "Three-Color, Tunable, Organic Light-Emitting Devices," Science **276**, 2009–2011 (1997).

[70] V. Bulović, V. G. Kozlov, V. B. Khalfin, and S. R. Forrest, "Transform-Limited, Narrow-Linewidth Lasing Action in Organic Semiconductor Microcavities," Science **279**, 553–555 (1998).

[71] T. Someya, R. Werner, A. Forchel, M. Catalano, R. Cingolani, and Y. Arakawa, "Room Temperature Lasing at Blue Wavelengths in Gallium Nitride Microcavities," Science **285**, 1905–1906 (1999).

[72] V. Bulović, V. B. Khalfin, G. Gu, V. B., P. E. Burrows, D. Z. Garbuzov, and S. R. Forrest, "Weak microcavity effects in organic light-emitting devices," Phys. Rev. B **58**, 3730–3740 (1998).

[73] H. Yokoyama and S. D. Brorson, "Rate equation analysis of microcavity lasers," J. Appl. Phys. **66**, 4801–4805 (1989).

[74] T. Baba, T. Hamano, and F. Koyama, "Spontaneous Emission Factor of a Microcavity DBR Surface Emitting Laser," IEEE J. Quantum Electron. **27**, 1347–1358 (1991).

[75] M. Osuge and K. Ujihara, "Spontaneous emission and oscillation in a planar microcavity dye laser," J. Appl. Phys. **76**, 2588–2597 (1994).

[76] H. Benisty, H. De Neve, and C. Weisbuch, "Impact of Planar Microcavity Effects on Light Extraction-Part I: Basic Concepts and Analytical Trends," IEEE J. Quantum Electron. **34**, 1612–1631 (1998).

[77] H. Benisty, H. De Neve, and C. Weisbuch, "Impact of Planar Microcavity Effects on Light Extraction-Part II: Selected Exact Simulations and Role of Photon Recycling," IEEE J. Quantum Electron. **34**, 1632–1643 (1998).

[78] G. S. Agarwal and S. Dutta Gupta, "Microcavity-induced modification of the dipole-dipole interaction," Phys. Rev. A **57**, 667–670 (1998).

[79] M. Hopmeier, W. Guss, M. Deussen, E. O. Göbel, and R. F. Mahrt, "Enhanced Dipole-Dipole Interaction in a Polymer Microcavity," Phys. Rev. Lett. **82**, 4118–4121 (1999).

[80] W. L. Barnes and P. Andrew, "Energy transfer under control," Nature **400**, 505–506 (1999).

[81] P. Mataloni, E. De Angelis, and F. De Martini, "Bose-Einstein Partition Statistics in Superradiant Spontaneous Emission," Phys. Rev. Lett. **85**, 1420–1423 (2000).

[82] P. Andrew and W. L. Barnes, "Förster Energy Transfer in an Optical Microcavity," Science **290**, 785–788 (2000).

[83] D. G. Lidzey, D. D. C. Bradley, A. Armitage, S. Walker, and M. S. Skolnick, "Photon-Mediated Hybridization of Frenkel Excitons in Organic Semiconductor Microcavities," Science **288**, 1620–1623 (2000).

[84] M. J. A. de Dood, J. Knoester, A. Tip, and A. Polman, "Förster transfer and the local optical density of states in erbium-doped silica," Phys. Rev. B **71**, 115 102 (2005).

[85] R. Jin, D. Boggavarapu, M. Sargent III, P. Meystre, H. M. Gibbs, and G. Khitrova, "Photon-number correlations near the threshold of microcavity lasers in the weak-coupling regime," Phys. Rev. A **49**, 4038–4042 (1994).

[86] T. Enomoto, T. Sasaki, K. Sekiguchi, Y. Okada, and K. Ujihara, "Intensity fluctuation of a pulsed planar microcavity laser," J. Appl. Phys. **80**, 6595–6601 (1996).

[87] J. A. Veerman, M. F. Garcia-Parajo, L. Kuipers, and N. F. van Hulst, "Time-Varying Triplet State Lifetimes of Single Molecules," Phys. Rev. Lett. **83**, 2155–2158 (1999).

[88] M. Orrit, "Photon Statistics in Single Molecule Experiments," Single Mol. **3**, 255–265 (2002).

[89] K. Kai, C. Oh-Hara, H. Inoue, T. Yamanaka, and K. Ujihara, "Measurement of the Characteristic Transverse Mode Radius of a Planar Microcavity Laser," Jpn. J. Appl. Phys. **41**, 7398–7399 (2002).

[90] F. Cairo, F. De Martini, and D. Murra, "QED-Vacuum Confinement of Inelastic Quantum Scattering at Optical Frequencies: A New Perspective in Raman Spectroscopy," Phys. Rev. Lett. **70**, 1413–1416 (1993).

[91] A. Fainstein, B. Jusserand, and V. Thierry-Mieg, "Raman Scattering Enhancement by Optical Confinement in a Semiconductor Planar Microcavity," Phys. Rev. Lett. **75**, 3764–3767 (1995).

[92] A. B. Myers, P. Tchénio, M. Z. Zgierski, and W. E. Moerner, "Vibronic Spectroscopy of Individual Molecules in Solids," J. Phys. Chem. **98**, 10 377–10 390 (1994).

[93] A. Kiraz, M. Ehrl, C. Bräuchle, and A. Zumbusch, "Ultralong coherence times in the purely electronic zero-phonon line emission of single molecules," Appl. Phys. Lett. **85**, 920–922 (2004).

[94] A. Kiraz, M. Ehrl, T. Hellerer, Ö. E. Müstecaplioğlu, C. Bräuchle, and A. Zumbusch, "Indistinguishable Photons from a Single Molecule," Phys. Rev. Lett. **94**, 223 602 (2005).

[95] R. F. Oulton, P. N. Stavrinou, and G. Parry, "Optical coherence of planar microcavity emission," Appl. Phys. B **80**, 817–821 (2005).

[96] Z. S. Wang, H. A. Rabitz, and M. O. Scully, "The Single-Molecule Dye Laser," Laser Physics **15**, 118–123 (2005).

[97] F. D. Stefani, K. Vasilev, N. Bocchio, N. Stoyanova, and M. Kreitner, "Surface-Plasmon-Mediated Single-Molecule Fluorescence Through a Thin Metallic Film," Phys. Rev. Lett. **94**, 023 005 (2005).

[98] B. C. Buchler, T. Kalkbrenner, C. Hettich, and V. Sandoghdar, "Measuring the Quantum Efficiency of the Optical Emission of Single Radiating Dipoles Using a Scanning Mirror," Phys. Rev. Lett. **95**, 063 003 (2005).

[99] S. Reich, C. Thomsen, and J. Maultzsch, *Carbon Nanotubes* (WILEY-VCH, Weinheim, 2004).

[100] A. G. Souza Filho, A. Jorio, J. H. Hafner, C. M. Lieber, R. Saito, M. A. Pimenta, G. Dresselhaus, and M. S. Dresselhaus, "Electronic transition energy E_{ii} for an isolated (n,m) single-wall carbon nanotube obtained by anti-Stokes/Stokes resonant Raman intensity ratio," Phys. Rev. B **63**, 241 404(R) (2001).

[101] B. Lounis and M. Orrit, "Single-photon sources," Rep. Prog. Phys. **68**, 1129–1179 (2005).

[102] F. Jelezko, A. Volkmer, I. Popa, K. K. Rebane, and J. Wrachtrup, "Coherence length of photons from a single quantum system," Phys. Rev. A **67**, 041 802(R) (2003).

[103] P. Grangier, G. Roger, and A. Aspect, "Experimental Evidence for a Photon Anticorrelation Effect on a Beam Splitter: A New Light on Single-Photon Interferences," Europhys. Lett. **1**, 173–179 (1986).

[104] J. Eschner, C. Raab, F. Schmidt-Kaler, and R. Blatt, "Light interference from single atoms and their mirror images," Nature **413**, 495–498 (2001).

[105] C. Santori, D. Fattal, J. Vučković, G. S. Solomon, and Y. Yamamoto, "Indistinguishable photons from a single-photon device," Nature **419**, 594–597 (2002).

[106] J. Chamberlain, *The Principles of Interferometric Spectroscopy* (Wiley, Chichester, 1979).

A   Acknowledgement

The author would like to thank the following people and institutions for their contribution to this thesis:

Prof. Dr. Alfred Johann Meixner (University of Tübingen). He is the Ph. D. supervisor and supported this work by his interest, stimulating discussions and many fruitful suggestions. He provided his laboratory and organized the necessary funding for the realization of the experiments discussed in this thesis. Moreover, he gave the opportunity to the author to report the results on international conferences.

Prof. Dr. Achim Hartschuh (LMU, Munich). He contributed by advise, strong experimental support as well as calculations and discussions on micro-resonator physics and nano-optics. Thanks to his support and his continuing motivation it was possible to collect this large amount of new scientific results presented in this thesis.

Dipl.-Chem. Frank Schleifenbaum (University of Tübingen). He contributed to many experiments discussed in this work. He helped with solving chemical problems and gave good suggestions for the sample preparation. Moreover, he prepared several illustrative and neat figures for publications, presentations and also for this work (see Fig. 13 and Fig. 14).

Dr. Clemens Stupperich (University of Siegen). He started the computer simulations for modeling the optical properties of the microresonator.

Dr. Virgilio Failla (University of Tübingen). He extended the computer simulations for modeling the optical properties of the microresonator. By developing elegant solutions, he succeeded with modeling the spectral shape of microresonator-controlled molecular fluorescence.

Dr. Rafal Korlacki (University of Tübingen). He contributed essentially in experiments and data analysis for obtaining the results on single molecule Fourier spectroscopy presented in chapter 8.

M. Sc. Huihong Qian (LMU, Munich). She helped to obtain the results of microresonator-controlled phonon scattering on embedded single-walled carbon nanotubes shown in chapter 7. Moreover, she performed valuable afm-measurements.

B   Abstract

In this thesis, we investigate the influence of a planar optical $\lambda/2$-microresonator on the Spontaneous Emission rate of embedded molecules and the implications on the microresonator-controlled emission by means of scanning confocal optical microscopy and spectroscopy. The experimental results are compared with computer calculations based on existing theoretical models.

In chapter 1, we introduce and motivate the research described in this work and define the scope of this thesis. Moreover, we give an overview of the instrumentation used for the experiments described in the following chapters.

In chapter 2, we present a new microresonator design which allows the efficient detection of single molecules by measuring the molecular fluorescence emission coupled into resonant photonic modes. First, we discuss the preparation and characterization of the resonator mirrors. Second, the manufacturing of the microresonator and the experimental determination of its optical properties is described. In a third step, the coupling between single dye molecules and the longitudinal cavity mode of the resonator in the $\lambda/2$-regime is investigated. As a result, we observe a significant spectral narrowing of room temperature single molecule fluorescence emission determined by the spectral width of the on-axis transmission spectrum of the microresonator. The microresonator forms the basis for all experiments described in the following chapters.

In chapter 3, we discuss fluorescence decay curves delivered by single dye molecules embedded in our $\lambda/2$-microresonator. The Spontaneous Emission rate of individual molecules was found to be enhanced by the Purcell-effect up to 3 times compared to the Spontaneous Emission rate in free space as determined by the mirror spacing and in agreement with predictions from our calculations based on first order perturbation theory. The results presented in this chapter allow modeling the spectral shape of microresonator-controlled emission as described in chapter 4 without accounting for free parameters. Moreover, the knowledge of the Spontaneous Emission rate of single molecules as determined by the mirror spacing of the microresonator gives access to an important parameter for photonic applications, i. e. the Spontaneous Emission coupling ratio of the system introduced in chapter 5. Importantly, the radiative coupling between electronic-vibronic transitions of single molecules and photonic modes of the microresonator in both fluorescence and Raman scattering processes as discussed in chapter 7 can be quantified using the same theoretical approach as described in chapter 3.

In chapter 4, we investigate experimentally and theoretically the spec-

tral shape of fluorescence emission of dye molecules coupled to the photonic mode structure of the $\lambda/2$-microresonator by varying the emitter concentration and the mirror spacing. The spectral shape of the outcoupled emission is modeled by summing radiative on- and off-axis contributions depending on the mirror spacing. Good agreement was found between experimental results and simulations taking into account the complex interplay between focussed pump field, broad free-space fluorescence spectrum of embedded molecules, microresonator properties and detection conditions. As an important result, both the maximum spectral narrowing and the maximum output of the microresonator-controlled fluorescence emission occur for the same mirror spacing in our system. This finding will be further explored in chapter 5: There, we connect the Spontaneous Emission Rate with both the output and the Stimulated Emission properties of the microresonator-molecule system.

In chapter 5, we investigate experimentally and theoretically the fluorescence dynamics of dye molecules immobilized in a planar $\lambda/2$-microresonator for varying emitter concentrations. Time-resolved spectroscopy reveals enhancement and inhibition of radiative rates determined by the mirror spacing in agreement with simulation results. The maximum output efficiency was found to occur for mirror spacings where no rate modification is observed and coincides with the maximum of Stimulated Emission efficiency which was probed by means of output fluctuations. In chapter 6, we will identify isolated, unstable emitting spatial modes formed between the microresonator mirrors as the origin of the output fluctuations mentioned above.

In chapter 6, we investigate the radiation pattern formed on the surface of a planar $\lambda/2$-microresonator enclosing immobilized dye molecules. Using widefield imaging microscopy, we observed isolated spatial modes which occurred randomly in the pumped microresonator area, exhibiting strong intensity fluctuations. The measured upper limit for the diameter of isolated spatial modes around 0.5 μm was found to agree with theoretical predictions for the effective mode radius of our system. Moreover, we demonstrate the formation and decay of a spatial double mode as a proof for the validity of the spatial mode concept in planar microresonators.

In chapter 7, we study spatially isolated molecules and nanostructures, respectively, immobilized in a planar $\lambda/2$-microresonator by means of fluorescence and Raman microscopy. In a first step, we show that single terrylene molecules relax into microresonator-allowed vibronic levels of the electronic ground state by emission of single fluorescence photons. Low temperature fluorescence spectra demonstrate that the microresonator spectrally isolates the purely electronic transition of single terrylene molecules accompanied by suppression of radiative relaxation in excited vibronic levels of the electronic ground state. These low-temperature experiments are also the starting

point for performing single molecule Fourier spectroscopy on dye molecules as reported in chapter 8. In a second step, we demonstrate microresonator-controlled Raman scattering on embedded single-walled carbon nanotubes and discuss if utilization of a $\lambda/2$-microresonator enables cooling them.

In chapter 8, we analyze the correlation between the spectral shape and the temporal coherence of fluorescence emission of single dye molecules embedded in a planar $\lambda/2$-microresonator. Low-temperature studies reveal the influence of typical single molecule fluorescence features like intensity blinking and spectral diffusion on the visibility of two-beam interferograms measured with a Michelson interferometer. By comparison with spectroscopic data that was acquired with a grating spectrometer, we demonstrate the applicability of Fourier transform spectroscopy for unstable emitting molecules. Moreover, we show how the phonon sideband accompanying the narrow molecular zero-phonon emission line affects the visibility of interference fringes.

C Zusammenfassung

In dieser Arbeit wird der Einfluss eines planaren optischen $\lambda/2$-Mikroresonators auf die Spontane Emissionsrate von eingebetteten Molekülen und die daraus resultierenden Modifikationen der molekularen Emission untersucht. Die Experimente wurden unter Verwendung von konfokaler optischer Mikroskopie und Spektroskopie durchgeführt. Die dabei erzielten Resultate werden mit den Ergebnissen von Computersimulationen und Rechnungen verglichen, die auf der Grundlage von bekannten theoretischen Ansätzen gewonnen wurden.

Kapitel 1 beginnt mit der inhaltlichen Einführung und Motivation der Arbeit. Danach erfolgt eine Abgrenzung und Erläuterung des Inhalts der folgenden Kapitel. Abschließend wird die experimentelle Ausstattung zur Durchführung der Messungen, die in dieser Arbeit diskutiert werden, vorgestellt.

In Kapitel 2 wird ein neuartiges Mikroresonator-Design vorgestellt, das die Detektion einzelner zwischen den Resonatorspiegeln eingebetteter Moleküle erlaubt. Zunächst wird die Herstellung und Charakterisierung der Resonator-Spiegel diskutiert. Danach wird die Herstellung des Mikroresonators und die experimentelle Bestimmung seiner optischen Eigenschaften erörtert. Abschließend wird die radiative Kopplung zwischen einzelnen Farbstoffmolekülen und der longitudinalen photonischen Mode des $\lambda/2$-Mikroresonators untersucht. Durch diese Kopplung wird die spektrale Breite der Fluoreszenzemission einzelner Moleküle reduziert, und zwar auf die spektrale Breite des axialen Transmissionsspektrum des Mikroresonators. Der hier vorgestellte Mikroresonator bildet die Basis für sämtliche in dieser Arbeit beschriebenen Experimente.

In Kapitel 3 werden Fluoreszenzzzerfallskurven analysiert, die an einzelnen innerhalb des $\lambda/2$-Mikroresonators räumlich isolierten und immobilisierten Farbstoffmolekülen gemessen wurden. Die Spontane Emissionsrate einzelner Moleküle ist durch den Purcell-Effekt gegenüber dem Referenzwert ohne Resonatoreinfluss um bis zu dreifach erhöht und wird duch den Abstand der Resonatorspiegel bestimmt. Die experimentellen Ergebnisse zeigen dabei eine gute Übereinstimmung mit theoretischen Vorhersagen, die auf quantenmechanischer Störungstheorie erster Ordnung basieren. Die hier vorgestellten Ergebnisse erlauben die Berechnung der vom Mikroresonator modifizierten spektralen Form der molekularen Emission ohne die Berücksichtigung freier Parameter (siehe Kapitel 4). Des Weiteren ermöglicht die Kenntnis der Spontanen Emissionsrate einzelner Moleküle als Funktion des Spiegelabstands im Mikroresonator auch die Bestimmung einer wichtigen Kenngröße für pho-

tonische Anwendungen, nämlich des Kopplungsverhältnisses der Spontanen Emission für dieses System (siehe Kapitel 5). Darüber hinaus kann mit dem hier vorgestellten Ansatz auch die radiative Kopplung zwischen wohldefinierten elektronisch-vibronischen Übergängen einzelner Moleküle und der photonischen Modenstruktur des Mikroresonators sowohl für Fluoreszenz- als auch für Raman-Prozesse modelliert werden (siehe Kapitel 7).

In Kapitel 4 werden Fluoreszenzspektren untersucht, die für verschiedene Molekülkonzentrationen und unter Variation des Spiegelabstands des $\lambda/2$-Mikroresonators gemessen wurden. Die spektrale Form der ausgekoppelten Emission wird berechnet, indem die radiativen Beiträge aus der Kopplung der Moleküle an die photonische Modenstruktur des Resonators in Abhängigkeit vom Abstand der Resonatorspiegel aufsummiert werden. Eine gute Übereinstimmung der experimentellen und gerechneten Spektren ergibt sich, wenn das komplexe Zusammenspiel zwischen dem fokussierten Laserlichtfeld, dem breiten Fluoreszenzspektrum der eingebetteten Moleküle, den optischen Eigenschaften des Mikroresonators sowie den optischen Messbedingungen angemessen berücksichtigt wird. Ein wesentliches Resultat ist, dass für die ausgekoppelte und detektierte Fluoreszenzemission die maximale spektrale Einschnürung und die maximale integrierte Leistung bei demselben Resonatorspiegelabstand auftreten. Dieses Phänomen wird in Kapitel 5 wieder aufgegriffen: Dort wird der Einfluss der modifizierten Spontanen Emissionsrate auf die Effizienz für Stimulierte Emission und die integrierte ausgekoppelte Lichtintensität in unserem Mikroresonator-Molekül-System untersucht.

In Kapitel 5 wird die Fluoreszenzdynamik von Farbstoffmolekülen im $\lambda/2$-Mikroresonator unter Variation der Emitterkonzentration und des Resonatorspiegelabstands experimentell und theoretisch untersucht. Zeitaufgelöste Spektroskopie offenbart die Verstärkung und Unterdrückung der Spontanen Emissionsrate der eingebetteten Farbstoffmoleküle als Funktion des Abstandes der Resonatorspiegel in Übereinstimmung mit den theoretischen Vorhersagen. Das Maximum der Auskopplungseffizienz und das Maximun der Effizienz für Stimulierte Emission, welches über Intensitätsfluktutionen in der ausgekoppelten Fluoreszenz sondiert wurde, treten in unserem System für denselben Resonatorspiegelabstand auf. Bei diesem Spiegelabstand wird allerdings keine Modifikation der Spontanen Emissionsrate beobachtet. In Kapitel 6 werden räumlich isolierte, instabil emittierende Transversalmoden, die sich zwischen den Resonatorspiegeln ausbilden, als Ursache der beobachteten Intensitätsfluktutionen identifiziert.

In Kapitel 6 werden die Abstrahlungsmuster auf der Oberfläche eines mit Farbstoffmolekülen dotierten $\lambda/2$-Mikroresonators diskutiert, die mit Hilfe von zeitaufgelöster Weitfeld-Mikroskopie gemessen wurden. Räumlich isolier-

te Transversalmoden erscheinen zufällig im optisch gepumpten Bereich des Mikroresonators und weisen starke Intensitätsfluktuationen auf. Die experimentell bestimmte obere Grenze des Modenradius stimmt gut mit der theoretischen Vohersage für den effektiven Modenradius dieses Systems überein. Darüber hinaus wird der Aufbau und Zerfall einer transversalen Dopelmode vorgestellt und diskutiert.

In Kapitel 7 werden einzelne Moleküle und Nanostrukturen, die im $\lambda/2$-Mikroresonator eingebettet und räumlich isoliert sind, mit Hilfe von Fluoreszenz- und Raman-Mikroskopie untersucht. Wird der Mikroresonator auf $T = 1,8$ K abgekühlt, beobachtet man die radiative Relaxation einzelner Terrylen-Moleküle in einen vom Mikroresonator selektierten angeregten vibronischen Zustand des elektronischen Grundzustands unter Emission einzelner Fluoreszenzphotonen. Unter diesen Bedingungen erlaubt der Mikroresonator darüber hinaus die spektrale Isolation des rein elektronischen Übergangs einzelner Terrylen-Moleküle. Diese Isolation ist begleitet von einer unterdrückten radiativen Relaxation in angeregte vibratorische Niveaus des elektronischen Grundzustands. Die hier beschriebenen Tieftemperaturexperimente bilden gleichzeitig den Ausgangspunkt für die Einzelmolekül-Fourierspektroskopie an fluoreszierenden Farbstoffmolekülen, wie sie in Kapitel 8 vorgestellt wird. Des Weiteren wird die vom Mikroresonator gesteuerte Raman-Streuung an eingebetteten Einzelwand-Kohlenstoffnanoröhren experimentell demonstriert. Die Möglichkeit, einzelne Kohlenstoffnanoröhren unter Verwendung eines $\lambda/2$-Mikroresonators optisch zu kühlen, wird ebenfalls erörtert.

In Kapitel 8 wird der Zusammenhang zwischen spektraler Form und zeitlicher Kohärenz der Fluoreszenzemission einzelner Farbstoffmoleküle, die im $\lambda/2$-Mikroresonator eingebettet sind, analysiert. Experimente bei kryogenen Temperaturen zeigen den Einfluss typischer Einzelmolekülfluktuationen, wie Blinken der Fluoreszenzemission und spektrale Diffusion, auf die Sichtbarkeit von Zweistrahl-Interferogrammen, die mit einem Michelson-Interferometer gemessen wurden. Durch Vergleich mit Fluoreszenzspektren, die mit einem Gitterspektrometer aufgenommen wurden, wird die Anwendbarkeit der Fourier-Transform-Spektroskopie auf unstabil emittierende Moleküle demonstriert. Darüber hinaus wird der Einfluss des Phononenflügels, der die schmale Emissionslinie des rein elektronischen molekularen Übergangs begleitet, auf die Sichtbarkeit der Interferenzstreifen diskutiert.